Electrochemical investigations of the Membrane-Bound [NiFe] Hydrogenase of *Ralstonia eutropha*

Valentin Radu

Submitted in accordance with the requirements for the degree of

Doctor of Philosophy

The University of Leeds

School of Biomedical Sciences

April 2016

The candidate confirms that the work submitted is his own, except where work which has formed part of jointly authored publications has been included. The contribution of the candidate and the other authors to this work has been explicitly indicated below. The candidate confirms that appropriate credit has been given within the thesis where reference has been made to the work of others.

The chapters within the thesis that have been based on work from jointly authored publications are chapters 4, 5, and 6.

Chapters 4 and 5

Radu, V., Frielingsdorf, S., Evans, S. D., Lenz, O., and Jeuken, L. J. C. (2014). Enhanced Oxygen-Tolerance of the Full Heterotrimeric Membrane-Bound [NiFe]-Hydrogenase of *Ralstonia eutropha*. J. Am. Chem. Soc. 136, 8512 − 8515.

Valentin Radu prepared the samples (bacterial inner membrane extracts and modified electrodes), planned and conducted the electrochemical experiments, analysed the experimental data, and contributed to the discussion and the writing of the manuscript. L. J. C. Jeuken provided guidance regarding the design of experiments, data analysis, and contributed to the discussion and the writing of the manuscript. S. Frielingsdorf provided the raw material for sample preparation (bacterial total membranes) and contributed to the discussion and writing of the manuscript. S. D. contributed to the discussion and writing of the manuscript. O. Lenz has contributed to the discussion and the writing of the manuscript.

Chapter 6

Radu, V., Frielingsdorf, S., Evans, S. D., Lenz, O., and Jeuken, L. J. C. (2016). Reactivation from the Ni–B state in [NiFe] hydrogenase of *Ralstonia eutropha* is controlled by reduction of the superoxidized proximal cluster. Chem. Commun. 52, 2632-2635.

Valentin Radu prepared the samples (bacterial inner membrane extracts and modified electrodes), planned and conducted the electrochemical experiments, analysed the experimental data, and contributed to the discussion and the writing of the manuscript. L. J. C. Jeuken provided guidance regarding the design of experiments, data analysis, and contributed to the discussion and the writing of the manuscript. S. Frielingsdorf provided the raw material for sample preparation (bacterial total membranes), provided guidance regarding the design of experiments, and contributed to the discussion and writing of the manuscript. O. Lenz provided guidance regarding the design of experiments and contributed to the discussion and the writing of the manuscript.

Acknowledgements

I would like to thank my supervisors, Dr Lars Jeuken and Professor Stephen Evans, for their advice and support during my PhD. Particular thanks go to Dr Stefan Frielingsdorf and Professor Oliver Lenz at the Technische Universität Berlin, who provided in due time all the samples, without which this work would not have been possible. I would also like to thank Dr Roman Tuma for his advice and useful tips.

For their technical and moral support, I would like to thank Theodoros Laftsoglou, Dr Mengqiu Li, Vlad Vasilca, Joseph Oram, Anna Wroblewska-Wolna, Dr Khizar Sheikh, Dr Ee Taek Hwang, Matthias Gantner, Dr George Heath, Riitta Partanen, Honglin Rong, and Sunjie Ye.

Special thanks go to James Hetfield, Kirk Hammett, Lars Ulrich, Cliff Burton, Jason Newsted, and Rob Trujillo. Now, that the show is through, the metal's gone, it's time to hit the road.

Finally, I would like to thank my family for their unconditional support.

Abstract

Hydrogenases are structurally complex enzymes that catalyse the production and oxidation of H_2 in a wide variety of microorganisms. The catalytic properties of these enzymes are related to the interaction between their redox-active metal cofactors. O_2-tolerant [NiFe] hydrogenases catalyse H_2 oxidation in the presence of O_2, which normally completely inhibits other hydrogenases. Their (in)activation mechanism is of fundamental importance for H_2-based energy technologies.

The present study has characterized the catalytic properties of the full heterotrimeric membrane bound hydrogenase (MBH) in native-like conditions by using a novel approach for immobilizing the enzyme onto the electrode. With the use of the tethered bilayer lipid membrane (tBLM) approach, the study obtained mechanistic insights relevant to the *in vivo* functioning of the enzyme. The MBH, inserted into the tethered lipid membrane, in equilibrium with the quinone pool, was probed in cyclic voltammetry and chronoamperometry experiments.

The catalytic properties displayed at oxidizing potentials revealed that the heterotrimeric MBH undergoes anaerobic oxidative inactivation to a much smaller extent compared to the heterodimeric sub-complex, which was probed in previous protein film electrochemistry studies. In addition, the enzyme recovers after aerobic inactivation under oxidizing conditions without the application of reducing potentials.

The reactivation kinetics of MBH^{wt} and that of an MBH variant with the metal cofactor configuration of an O_2-sensitive [NiFe] hydrogenase were probed under oxidative substrate-limiting conditions. The results show that the O_2 sensitive mutant reactivates

faster than MBH^{wt}. This indicates that protection against oxidative damage is achieved by tuning electron transfer to the active site with the scope of preventing the formation of reactive species that would lead to irreversible inactivation.

Table of Contents

List of Tables

List of Figures

List of abbreviations

AH - actinobacterial hydrogenase

BCA - bicinchoninic acid assay

BLM - bilayer lipid membrane

CCCP - Carbonyl cyanide *m*-chlorophenyl hydrazone

CHES - (2-(Cyclohexylamino)ethanesulfonic acid)

CPE - constant phase element

CV - cyclic voltammetry

DCM - dichloromethane

EDTA - ethylenediaminetetraacetic acid

EIS - electrochemical impedance spectroscopy

EO3C - triethyleneoxythiol cholesterol

EPR – electron paramagnetic resonance spectroscopy

FTIR – Fourier transform infrared spectroscopy

IM - inner membrane

ITO - indium-tin oxide

MBH - membrane-bound hydrogenase

MES - (2-(*N*-morpholino)ethanesulfonic acid)

MOPS - 3-(*N*-morpholino)propanesulfonic acid

OM - outer membrane

PFE - protein film electrochemistry

PGE - pyrolytic graphite electrode

PTFE - [poly(tetrafluoroethylene)]

RH - regulatory hydrogenase

SAM - self assembled monolayer

SH - soluble hydrogenase

SHE - standard hydrogen electrode

TAPS - (3-[[1,3-dihydroxy-2-(hydroxymethyl)propan-2-yl]amino]propane-1-sulfonic acid

tBLM - tethered bilayer lipid membrane

TSG - template stripped gold

1. Introduction

Hydrogenases are complex microbial metallo-enzymes which catalyse the reversible oxidation of H_2 (Equation 1) (Lubitz et al., 2014; Fritsch et al., 2013; Parkin and Sargent, 2012; Vignais and Billoud, 2007). The efficiencies of hydrogenases are comparable to those achieved by Pt under similar conditions (Woolerton and Vincent, 2009; Jones et al., 2002). Many organisms, like prokaryotic microbes, eukaryotic protozoa and fungi, make use of the catalytic properties of hydrogenases to produce H_2 in order to dispose of the excess reducing equivalents or to cleave H_2 into protons and electrons in order to generate energy (Armstrong, 2004; Evans and Pickett, 2003). Even pathogenic bacteria from the mammalian gut have the capability to use H_2 as an energy source. Hydrogenases present in *Helicobacter pylori* help the bacterium in the colonization of the stomach environment by metabolising H_2 formed during carbohydrate fermentation (Olson and Maier, 2002).

$$H_2 \xleftrightarrow{hydrogenase} 2H^+ + 2e^- \qquad (1)$$

The first indication of the existence of hydrogenases was provided by Stephenson and Stickland (1931), who observed that *E. coli* evolves H_2 during growth under anaerobic conditions. Stephenson and Stickland, who coined the term “hydrogenase”, used redox dyes to prove the formation of H_2. The fact that dye reduction was inhibited by carbon monoxide (CO), as was determined later, indicated the involvement of transition metals in the process (Thauer et al., 2010).

Since their discovery in 1931, hydrogenases have been a subject of intense research not only because of their intriguing enzymology, but lately also because of their potential application in renewable energy technologies (Wakerley and Reisner, 2015; de Poulpiquet et al., 2014; Parkin and Sargent, 2012; Reisner, 2011; Thauer, 2011; Friedrich et al., 2011; Wait et al., 2010; Le Goff et al., 2009; Heinekey, 2009) and in catalysis for chemical production (Reeve et al., 2015; Reeve et al., 2012). Efforts have been invested in developing bio-mimetic H_2-producing catalysts, genetically engineered hydrogenases for photobiological H_2 production, and membrane-free H_2/O_2 fuel cells based on O_2-tolerant hydrogenases. Many hydrogenases possess a remarkable tolerance to inhibitors like O_2, CO, and H_2S, a crucial property since their application as catalysts in energy technologies requires them to function in the presence of air or even utilize gaseous mixtures containing CO or H_2S.

From the point of view of the metal content of their active site, hydrogenases are classified into three main classes: [NiFe], [FeFe], and [Fe] hydrogenases (Lubitz et al., 2014; Vignais and Billoud, 2007; Fontecilla-Camps et al., 2007). All three types of hydrogenases contain a Fe atom coordinated by thiolates and CO ligands. In [NiFe] and [FeFe] hydrogenases, Fe is also coordinated by cyanide (CN^-) ligands.

[NiFe] and [FeFe] hydrogenases catalyse both the reduction of protons and the oxidation of H_2, while [Fe]-hydrogenases catalyse only the first step in the uptake process (the heterolytic cleavage of H_2) (Thauer et al., 2010; Meyer et al., 2007). Hydrogenases located in the cytoplasm are usually associated with H_2 production and those located in the membrane or the periplasm of gram-negative bacteria are associated with H_2 oxidation. So far, the sequences of more than 450 hydrogenases have been determined

based on genome analysis. [NiFe] and [FeFe] hydrogenases constitute by far the most studied classes (Mulder et al., 2011; Vignais and Billoud, 2007). [NiFe] hydrogenases have been of particular interest, as they include a sub-class of so-called O_2-tolerant membrane-bound hydrogenases (MBHs) which display higher tolerances to aerobic/oxidizing conditions (Fritsch et al., 2013). The introductory chapter provides a more detailed overview of [NiFe] hydrogenases and only a brief description of [FeFe] and [Fe] hydrogenases as the focus of my PhD studies has been on [NiFe] hydrogenase.

1.1 [NiFe] Hydrogenases

[NiFe] hydrogenases are found in organisms that are capable of living in very diverse environmental conditions: under light or in darkness, in anaerobic or aerobic media. The structures and catalytic properties of [NiFe] hydrogenases are tailored to meet the physiological requirements under the given regime of the organism (see Section 1.1.2). [NiFe] hydrogenases contain at least two subunits: a large (α) subunit (with a molecular weight of ~60 kDa in MBHs), hosting the [NiFe] active site, and a small (β) subunit (with a molecular weight of ~35 kDa in MBHs), enclosing an [FeS] electron transfer relay (Lubitz et al., 2014; Volbeda et al., 2013; Fritsch et al., 2013; Horch et al., 2012; Volbeda et al., 2012; Fritsch et al., 2011a; Shomura et al., 2011; Ogata et al., 2010; Fontecilla-Camps et al., 2007; Volbeda et al., 1995). With a few exceptions, the Ni atom is coordinated by four cysteine thiolates (SCys) (Figure 1.1). In the sub-class of [NiFeSe] hydrogenases, the Ni atom is terminally coordinated by a cysteine and a selenocysteine (SeCys) residue (Marques et al., 2010; Vignais and Billoud, 2007; Garcin et al., 1999). Two cysteine thiolates form a bridge between the Ni atom and the

Fe atom. The Fe atom is coordinated to two CN^- and one CO ligand. One coordination site, bridging the Fe and the Ni atom, constitutes the substrate-binding site.

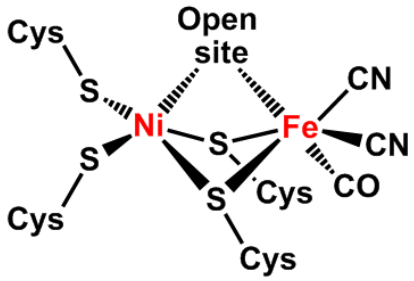

Figure 1.1 The structure of the active site of [NiFe] hydrogenases.

Typically, the small subunit of a [NiFe] hydrogenase accommodates up to three [FeS] clusters: a distal [4Fe-4S] cluster, a medial [3Fe-4S]/[4Fe-4S] cluster, and a proximal [4Fe-4S]/[4Fe-3S] cluster (distal/proximal is with respect to the active site). [4Fe-4S] medial clusters are more common in actinobacterial and [NiFeSe] hydrogenases (Schäfer et al., 2016; Marques et al., 2010; Garcin et al., 1999). The [NiFe] active site and the three [FeS] clusters are closely spaced (<14 Å) allowing rapid intramolecular electron transfer (Page et al., 1999). The [FeS] relay transfers electrons between the active site and the acceptor/donor site. The distal cluster, the furthest away from the [NiFe] active site, is located close to the surface of the small subunit (Horch et al., 2012; Fontecilla-Camps et al., 2007).

[NiFe] hydrogenases are classified into five main groups based on the amino acid sequences of their small and large subunits and on their inherent function (Parkin and Sargent, 2012; Kim and Kim, 2012; Vignais and Billoud, 2007).

The first group is constituted by the uptake [NiFe] hydrogenases, which are hydrogenases that are primarily involved in respiratory H_2 oxidation coupled to quinone

reduction. These are membrane-bound proteins, also called membrane-bound hydrogenases or H_2-uptake (Hup) hydrogenases, which link H_2 oxidation activity to the reduction of a wide variety of electron acceptors like SO_4^{2-}, NO_3^-, fumarate, CO_2, and O_2 (via terminal reductases). The energy is recovered in this case in the form of a proton motive force (Vignais and Billoud, 2007).

One common structural feature of the [NiFe] hydrogenases in this category is the existence of a long peptide (ca. 35-50 amino acid residues) at the N terminus of the small subunit for export across the cytoplasmic membrane. This peptide signals the export of the heterodimer into the periplasm or the periplasmic side of the cytoplasmic membrane (Vignais and Billoud, 2007). In addition to the α and β subunits, these hydrogenases contain a third subunit, a di-haem cytochrome *b*, which, along with a hydrophobic C-terminus of the small subunit, fixes the $\alpha\beta$ dimer to the membrane (Volbeda et al., 2013; Vignais and Billoud, 2007; Fontecilla-Camps et al., 2007). The cytochrome *b* subunit is also responsible for electrically connecting the hydrogenase active site to the quinone pool in the membrane (catalytically reducing the quinone pool).

The second group is constituted by cytoplasmic H_2 sensors and cyanobacterial uptake [NiFe] hydrogenases (Parkin and Sargent, 2012; Vignais and Billoud, 2007). These hydrogenases do not contain a signal peptide at the N terminus of the small subunit and consequently are not exported to the periplasm, remaining in the cytoplasm. The cytoplasmic H_2 sensor [NiFe] hydrogenases have the role of detecting H_2 and triggering a cascade of cellular reactions controlling the biosynthesis of uptake hydrogenases in response to the presence of H_2 (Friedrich et al., 2011; Ludwig et al., 2009). The

cyanobacterial uptake hydrogenases (HupSL) are linked to the occurrence of nitrogenase and are induced under N_2-fixing conditions (Vignais and Billoud, 2007).

The third group comprises the so called "bidirectional heteromultimeric cytoplasmic [NiFe] hydrogenases" which are water-soluble multi-protein complexes dependent on cofactors like NADH/NAD^+, NADPH/$NADP^+$ or F_{420} (8-hydroxy-5-deazaflavin). In addition to the dimeric hydrogenase module, these complexes contain subunits that bind the cofactors. These enzymes function reversibly, re-oxidizing the cofactors under anaerobic conditions using protons from water as electron acceptors (Horch et al., 2012; Friedrich et al., 2011; Vignais and Billoud, 2007).

The fourth group of [NiFe] hydrogenases is constituted by H_2-evolving hydrogenases. These are energy conserving, membrane-associated, multimeric proteins (containing at least six subunits) which catalyze H_2 production with no physiological H_2 oxidation activity. These hydrogenases reduce protons from water in order to dispose of excess reducing equivalents resulting from the anaerobic oxidation of C_1 organic compounds like CO or formate (Vignais and Billoud, 2007).

A recently discovered fifth group comprises [NiFe] hydrogenases found in soil-living actinobacteria (Constant et al., 2011). It has been hypothesized that these enzymes can oxidise H_2 at atmospheric concentrations, having presumed K_M values in the nM range. However, the K_M of the actinobacterial-type hydrogenase (AH) from *Ralstonia eutropha* was determined to be in the lower μM range, indicating that the high affinity for H_2 might not be a defining characteristic of this group (Schäfer et al., 2013).

1.1.1 Catalytic and inactivation mechanism

The challenge of identifying the critical steps involved in catalysis by hydrogenases arises from the difficulty of detecting and monitoring the state of redox active metal cofactors, buried deeply in the protein matrix, while having bound small and elusive molecules/ions like H_2 or H^-, or reactive and ubiquitous O_2-derived species. Crystallographic, spectroscopic, as well as computational methods and electrochemical techniques have all been employed for elucidating the mechanism of hydrogenase catalysis.

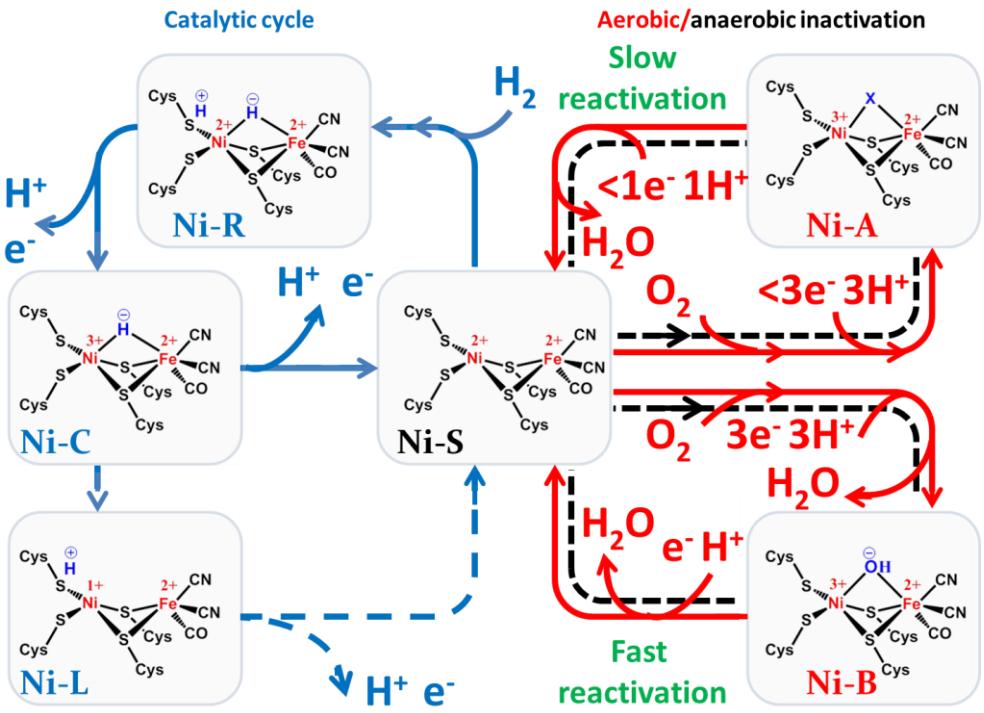

Figure 1.2 Possible mechanistic pathways for H_2 cycling, O_2 (aerobic) inactivation/reactivation, and anaerobic inactivation/reactivation at the active site of a [NiFe] hydrogenase (only the formal oxidation states of the metal atoms are depicted). The catalytic cycle is presented in blue, while the inactivation cycles are presented in red (aerobic) and black (anaerobic). "X" designates an unknown O_2-derived ligand.

In the [NiFe] hydrogenase catalytic cycle, H_2 is heterolytically cleaved via four redox intermediates: “Ni-S”, “Ni-C”, “Ni-R”, and “Ni-L” (Figure 1.2) (Bleijlevens et al., 2001; Krasna, 1979). All four states have distinct IR signatures. Ni-S and Ni-R are EPR-silent, while Ni-C and Ni-L are EPR-detectable intermediates.

In the Ni-S state the active site carries no exogenous ligand in the open site and the Ni atom has a formal 2+ charge (George et al., 2004; Kurkin et al., 2004). The cleavage of the H-H bond at the active site leads to the formation of the Ni-R state in which a H^- occupies the bridging position and a H^+ was thought to bind to the sulphur atom of one of the thiolates terminally coordinated to the Ni atom (Ogata et al., 2015). However, recently published data indicates that the guanidine group from an arginine residue near the metal centre may act as the base stabilizing the H^+ resulted from heterolytic cleavage (Evans et al., 2016). The release of one H^+ and one electron brings the enzyme into the Ni-C state in which an H^- is still occupying the binding site and the Ni atom is in the 3+ state (Brecht et al., 2003). The elimination of another electron along with the release of the proton from the bridging position returns the enzyme to the Ni-S state. An alternative route for the conversion to the Ni-S state was proposed to be via the Ni-L state, which carries the Ni atom in the +1 state (Figure 1.2). Previously thought to be only a photoinduced state, Ni-L was recently proved to be detectable under catalytic turnover conditions in the absence of light and its formation was shown to be favoured under basic pH conditions (Hidalgo et al., 2015; Murphy et al., 2015; Roessler et al., 2012).

Most [NiFe] hydrogenases cleave H_2 using a common mechanism and display similar catalytic properties under the reducing conditions ensured by the substrate, but not all of

them react in the same way under oxidizing and/or aerobic conditions. [NiFe] hydrogenases have been divided into two categories based on their catalytic performance under aerobic/oxidizing conditions. Many [NiFe] hydrogenases lose completely their catalytic activity in the presence of O_2 (Vincent et al., 2005a; Lamle et al., 2005; Leger et al., 2004; Lamle et al., 2004; Lamle et al., 2003; Leger et al., 2002a). These enzymes, also termed standard [NiFe] hydrogenases, recover extremely slowly after the removal of O_2. In contrast to these "O_2-sensitive" [NiFe] hydrogenases, "O_2-tolerant" [NiFe] hydrogenases recover activity much faster after O_2 inactivation. They are also known to partly maintain H_2 oxidation activity at ambient O_2 concentrations (Pandelia et al., 2010; Lukey et al., 2010; Ludwig et al., 2009; Cracknell et al., 2009; Armstrong et al., 2009; Cracknell et al., 2008a; Vincent et al., 2007; Vincent et al., 2005ab). Many of the O_2-tolerant [NiFe] hydrogenases are membrane-bound hydrogenases from organisms like *E. coli*, *Aquifex aeolicus*, *Ralstonia eutropha*, *Ralstonia metallidurans*, *Salmonella enterica* and *Hydrogenovibrio marinus* (de Poulpiquet et al., 2014; Fritsch et al., 2013). The disparity in the catalytic responses of [NiFe] hydrogenases under oxidizing conditions is believed to be due to different inactivation mechanisms.

Aerobically isolated and O_2-treated standard (O_2-sensitive) [NiFe] hydrogenases reside in two catalytically inactive states called "Ni-A" and "Ni-B" (Lukey et al., 2010; Ogata et al., 2010; Pandelia et al., 2010; Saggu et al., 2009; Volbeda et al., 2005; Bleijlevens et al., 2001). The same inactive states can be generated in anaerobic conditions by exposing the enzyme to oxidizing redox conditions (e.g. high electrode potentials/redox dyes) (Abou Hamdan et al., 2013; Jones et al., 2003). Both Ni-A and Ni-B are EPR-

active and can be monitored by FTIR spectroscopy. Both intermediates contain an O_2-derived bridging ligand. The Ni-B state carries an OH^- in the open binding site (Ogata et al., 2005; Volbeda et al., 2005), while the exact nature of the bridging species in Ni-A has remained unclear. Both Ni-A and Ni-B are converted to the active Ni-S state under reducing conditions (Figure 1.2). The formation of the Ni-B state has also been proved to be promoted by cyanide (CN^-), which is thought to bind at the active site under oxidizing conditions (Hexter et al., 2014). The rate of reactivation from the Ni-B state is significantly higher than in the case of Ni-A. Reactivation from the Ni-B state is completed in a matter of seconds, while Ni-A reactivation can take hours to complete (Ogata et al., 2005; Volbeda et al., 2005; Vincent et al., 2005a; Jones et al., 2003; Bleijlevens et al., 2001). The difference in the reactivation kinetics has prompted the designation of the Ni-B state as "ready" and the designation of the Ni-A state as "unready". While the active sites of standard [NiFe] hydrogenases are converted to both the Ni-A and Ni-B state under oxidizing conditions (Lukey et al., 2010; Vincent et al., 2005a; Volbeda et al., 2005; Jones et al., 2003; Bleijlevens et al., 2001), those of O_2-tolerant [NiFe] hydrogenases are converted only to the Ni-B state (Hidalgo et al., 2015; Evans et al., 2013; Goris et al., 2011; Pandelia et al., 2010; Saggu et al., 2009). Interestingly, the O_2 tolerant MBH from *E. coli* (Hyd-1) was also reported to form a mixture of Ni-A and Ni-B after treatment with O_2, although the fraction of Ni-A was determined to be small under controlled potential conditions (Lukey et al., 2010).

The striking difference in the inactivation pathways is thought to be due to the different electronic properties of the [FeS] relays. O_2-tolerant [NiFe] hydrogenases contain an unusual [4Fe-3S] cluster proximal to the active site as opposed to standard [NiFe]

hydrogenases which contain a [4Fe-4S] cluster. The [4Fe-3S] cluster, which contains six cysteine thiolates in its coordination environment, is stable in three oxidation states, performing two redox transitions at physiologically relevant potentials (Equations 2 and 3; midpoint potentials, E_m, are given for the membrane-bound [NiFe] hydrogenase of *Ralstonia eutropha*) (Fritsch et al., 2013; Volbeda et al., 2013; Volbeda et al., 2012; Goris et al., 2011; Fritsch et al., 2011ab; Shomura et al., 2011; Lukey et al., 2011).

$$[4Fe\text{-}3S]^{3+} \leftrightarrow [4Fe\text{-}3S]^{4+} \qquad E_m = -0.060\ V \qquad (2)$$

$$[4Fe\text{-}3S]^{4+} \leftrightarrow [4Fe\text{-}3S]^{5+} \qquad E_m = +0.160\ V \qquad (3)$$

The second redox transition is associated with major structural rearrangements: Fe(4) exchanges a sulphide ligand with an amide N atom of a cysteine residue (Figure 1.3).

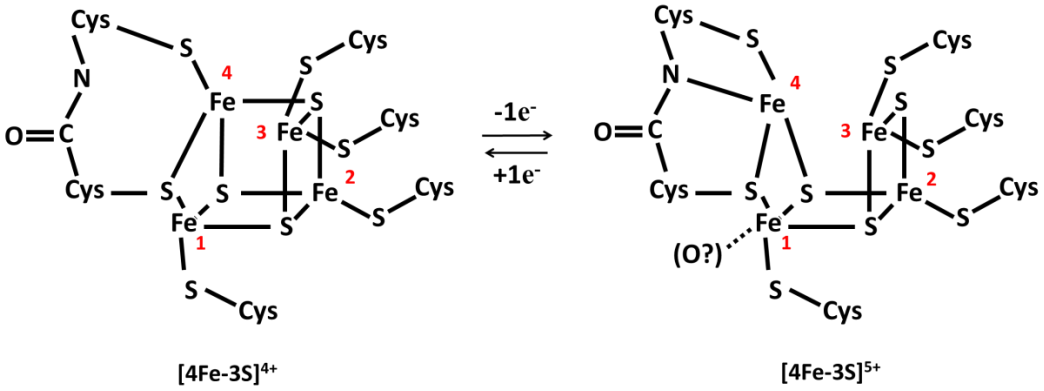

Figure 1.3 Schematic drawing of the structure of the unusual proximal $[4Fe\text{-}3S]^{4+}$ cluster undergoing oxidation, which is accompanied by the Fe(4) swapping a sulphide with an amide N and the addition of an O_2-derived species at Fe(1).

An O_2-derived ligand bound to Fe(1) of the [4Fe-4S] cluster (Figure 1.3), together with the aforementioned ligand exchange, is hypothesized to make the second redox transition accessible at physiologically relevant potentials (Frielingsdorf et al., 2014). It

should be noted that the additional O_2-derived ligand was observed only in the structures of *R. eutropha* MBH, but not in the structures of other O_2 tolerant MBHs.

The proximal [4Fe-4S] cluster in standard [NiFe] hydrogenases, which contains only four cysteine thiolates and two glycine residues in its coordination environment, performs only a single redox transition (Ogata et al., 2010; Vincent et al., 2007; Volbeda et al., 1995). The enhanced electron availability ensured by the unusual [4Fe-3S] cluster has been proposed to contribute to the formation only of the Ni-B state in O_2-tolerant [NiFe] hydrogenases under oxidizing conditions. The extra electron provided by the cluster is hypothesized to ensure the full reduction of an O_2 molecule, which would then lead to the formation of OH^- ligands in the open coordinating site (Fritsch et al., 2013). Standard [NiFe] hydrogenases, on the other hand, accumulate more Ni-A state compared to Ni-B and implicitly recover activity much slower than O_2-tolerant [NiFe] hydrogenases after inactivation (Evans et al., 2013; Lukey et al., 2010; Leger et al., 2004; Jones et al., 2003). The substitution of the supernumerary cysteine residues (the two extra cysteines in the coordination environment of the unusual [4Fe-3S] cluster) by glycine residues led to the loss of catalytic activity upon prolonged exposure to O_2 (Evans et al., 2013; Goris et al., 2011; Lukey et al., 2011). Spectroscopic analysis revealed the accumulation of unready inactive states, characteristic for O_2 sensitive [NiFe] hydrogenases. Interestingly, only small fractions of Ni-A state were detected, suggesting that the unready states generated electrochemically under aerobic conditions are not solely correlated to the spectroscopically defined Ni-A state.

It has been proved that H_2 oxidation in the presence of O_2, requiring reactivation from the Ni-B state, involves the reduction of O_2 to H_2O, which has to be removed from the

active site (Wulff et al., 2014; Lauterbach and Lenz, 2013; Fritsch et al., 2013). The crystal structures of the O_2-tolerant membrane-bound [NiFe] hydrogenases from *Ralstonia eutropha* and *Hydrogenovibrio marinus* revealed the presence of hydrophilic water channels leading from the active site to the surface of the large subunit, which might serve as an exit gate for the H_2O molecules generated at the active site (Fritsch et al., 2011a; Shomura et al., 2011). The reductase activity would require four electrons to be provided by the active site and the [FeS] relay. It has been suggested that one electron is provided by Ni ($Ni^{2+} \rightarrow Ni^{3+}$), two by the proximal [4Fe-3S] cluster ($[4Fe\text{-}3S]^{3+} \rightarrow [4Fe\text{-}3S]^{4+}$; $[4Fe\text{-}3S]^{4+} \rightarrow [4Fe\text{-}3S]^{5+}$), and another one by the medial cluster ($[4Fe\text{-}4S]^{0} \rightarrow [4Fe\text{-}4S]^{1+}$).

It has also been proposed that the occlusion of putative hydrophobic gas channels (through which gas molecules reach the active site) by bulky amino acid residues might contribute to O_2 tolerance (Liebgott et al., 2010a; Dementin et al., 2009). A recent study comparing the predicted gas tunnel routes in crystal structures of standard and O_2-tolerant [NiFe] hydrogenases hypothesized that the former have a more complicated and extended tunnel network, which might increase gas diffusion rates for both H_2 and O_2 (Kalms et al., 2016). However, site-directed mutagenesis studies have shown that the narrowing of the gas channels affects the rate of O_2 diffusion, but it does not significantly alter O_2 tolerance (Abou Hamdan et al., 2012; Liebgott et al., 2010b).

1.1.2 The model O_2-tolerant membrane-bound [NiFe] hydrogenase (MBH) from *Ralstonia eutropha*

The membrane-bound [NiFe] hydrogenase (MBH) from the β-proteobacterium *Ralstonia eutropha*, the enzyme studied in this thesis, is one of the best-studied O_2-tolerant hydrogenases (Fritsch et al., 2013; Lenz et al., 2010). It is one of the four hydrogenases found in *R. eutropha* which is considered to be one of the best studied organisms growing on H_2 and carbon dioxide (CO_2) (Schäfer et al., 2013; Cramm, 2009). *R. eutropha* has suffered many name changes due to nomenclature modifications. Initially assigned the name *Hydrogenomonas eutrophus*, it was successively reclassified in the genus *Alcaligenes*, *Ralstonia*, and *Wautersia*. Its current name, according to the Rules of the International Code of Nomenclature of Bacteria, is *Cupriavidus necator* (a name very rarely used) (Cramm, 2009; Vignais and Billoud, 2007).

R. eutropha is capable of growing on explosive gas mixtures, such as 70% H_2, 10% CO_2 and 20% O_2 (Lenz et al., 2010). When organic substrates are scarce, this bacterium can utilize CO_2 as a carbon source and H_2 as an energy source (Cramm, 2009). H_2 is converted to protons and electrons by two hydrogenases, the membrane-bound hydrogenase (MBH) and the soluble hydrogenase (SH), to provide energy. The regulatory hydrogenase (RH) controls the expression of MBH and SH in response to the availability of H_2 (Lenz et al., 2010). The fourth hydrogenase is an actinobacterial-type hydrogenase (AH) and its physiological role has not been determined yet (Schäfer et al., 2013).

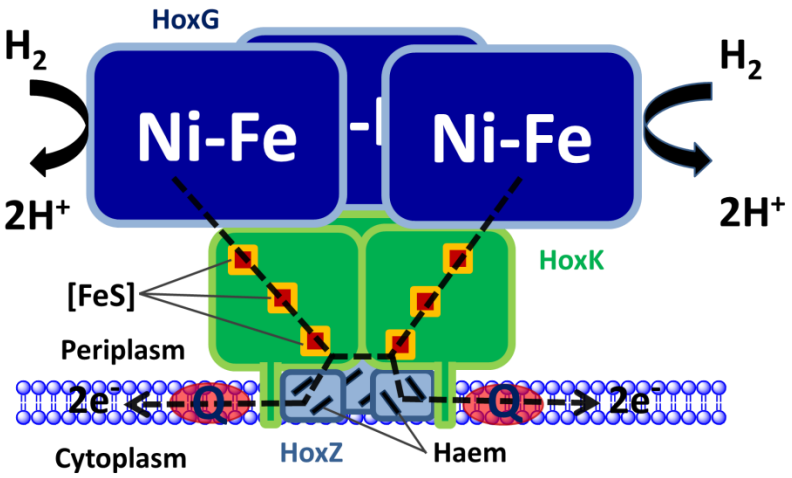

Figure 1.4 Schematic representation of MBH as part of the supercomplex of heterotrimers. H_2 is oxidized to protons and electrons at the active site of the large subunit, HoxG . The resulted electrons are transferred via the [FeS] relay of the small subunit, HoxK, to the membrane integral cytochrome *b*, HoxZ, which then reduces the quinone pool (Q).

Like all uptake hydrogenases, MBH is a heterotrimeric protein complex, consisting of a large subunit (HoxG, 67.2 kDa), a small subunit (HoxK, 34.6 kDa), and a membrane-integral cytochrome b_{562} harbouring two haem groups (HoxZ, 27.6 kDa) (Figure 1.4) (Fritsch et al., 2011a; Frielingsdorf et al., 2011; Bernhard et al., 1997). The hydrogenase module, consisting of the small and the large subunit, is oriented towards the periplasmic side of the cytoplasmic membrane. Based on molecular mass determinations of the purified enzyme, it was proposed that MBH forms super-complexes consisting of three heterotrimers (Frielingsdorf et al., 2011). However, the crystal structures of MBHs from *E. coli*, *A. vinosum*, *S. enterica*, and *H. marinus* have shown the formation of dipartite complexes (Bowman et al., 2014; Volbeda et al., 2012; Ogata et al., 2011; Shomura et al., 2011). Oligomerization of MBHs has been proposed to enable intermolecular electron transfer via the distal [4Fe-4S] cluster, which is located close to the surface of the small subunit (Figure 1.4) (Volbeda et al., 2013).

As previously mentioned, MBH couples H_2 oxidation to the reduction of the quinone pool via the cytochrome b_{562} subunit in the cytoplasmic membrane (Frielingsdorf et al., 2011; Bernhard et al., 1997). It has been proposed that MBH can donate electrons to both ubiquinone and menaquinone found in the membrane of *R. eutropha* (Frielingsdorf et al., 2011).

Like all other studied O_2 tolerant MBHs, the MBH from *R. eutropha* can oxidize H_2 at atmospheric O_2 levels. Under these conditions, the enzyme has a high tolerance towards O_2 and a high selectivity for H_2. The concentration of O_2 required to attenuate H_2 oxidation activity by 50% is approximately twenty times higher than the O_2 concentration required for the complete inhibition of the activity of "standard" (O_2-sensitive) [NiFe] hydrogenases. The value of the Michaelis-Menten constant for H_2, $K_M^{H_2}$, is in the lower end range reported for [NiFe] hydrogenases (< 10 μM) (Ludwig et al., 2009; Cracknell et al., 2009; Vincent et al., 2005b).

1.1.3 Electrochemical investigations of O_2 tolerant [NiFe] hydrogenases

1.1.3.1 Protein film electrochemistry

Protein film electrochemistry (PFE) is a powerful technique for studying the catalytic properties of redox enzymes (Armstrong et al., 2009, Vincent et al., 2007; Leger et al., 2003). It allows the measurement of potentials at which redox reactions occur and the determination of the rates of these reactions. The technique requires a small amount of enzyme, usually in the range of picomoles, which is adsorbed on the surface of an electrode (typically a pyrolitic graphite electrode, PGE) to form a mono- or sub-mono-layer film (Leger et al., 2003). The adsorbed enzyme molecules directly exchange

electrons with the electrode while maintaining the original configuration of the active site (Figure 1.5).

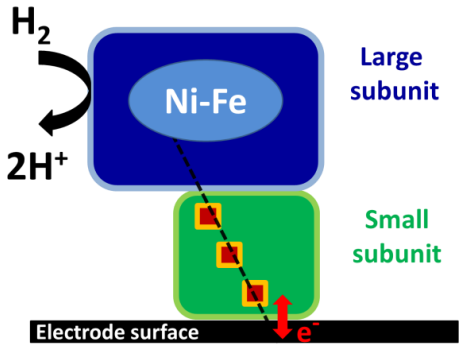

Figure 1.5 Schematic representation of the hydrophilic subunits of a MBH adsorbed on an electrode surface.

The immobilisation of the enzyme on the working electrode is ensured by first polishing the surface to expose a rough and oxidized fresh surface that provides adsorption sites (oxidized functional groups like –COOH, –C–OH and –C=O) which can non-covalently bind enzyme molecules (Blanford and Armstrong, 2006). In these conditions, the driving force for redox reactions is controlled through the applied electrode potential and the response is monitored via the current representing interfacial electron transfer. The stability of the enzyme film can be improved by employing poly-cationic co-adsorbates such as polymyxin (Hoeben et al., 2008). Covalent attachment can be used to achieve permanent immobilisation of the enzyme onto the electrode surface. The electrode can be functionalised with a monolayer of aromatic amines and then the enzyme can be linked to the electrode via amidic bonds formed between carboxylic groups of the protein backbone and electrode-bound amine groups (Rüdiger et al., 2005). The most common techniques employed for investigating the catalytic properties

of enzymes are cyclic voltammetry and chronoamperometry. PFE has been used to study the interaction of hydrogenases with small molecule inhibitors like O_2, CO and H_2S, complementing structural and spectroscopic studies.

The setup required for PFE involves a standard three-electrode configuration electrochemical cell holding a few millilitres of solution. The counter electrode is usually a platinum wire and the reference electrode is typically a saturated calomel electrode or a Ag/AgCl electrode. For precise temperature control the cell can be equipped with a water jacket. In the case of experiments employing hydrogenases, the cell is typically placed within an anaerobic glove box and gas mixtures are bubbled through the content of the cell. The addition of gases can also be done by injection of aliquots of gas-saturated solutions or by placing the cell in a controlled gas chamber (Armstrong et al., 2009; Goldet et al., 2008). Removal of gases can be done by flushing with other gases (usually N_2 or Ar). As the enzyme is adsorbed on the electrode surface, the content of the cell can be easily exchanged allowing the control of other variables (e.g. pH, ionic strength) in addition to temperature and electrode potential. A rotating disc electrode is typically used as the working electrode. This ensures a well-controlled flux of substrate to the surface and facilitates the removal of products away from the surface (Armstrong et al., 2009, Vincent et al., 2007) with the aim of avoiding electron transfer being limited by mass transport of the substrate/product to/from the electrode surface. In the absence of mass transport limitations, the inherent activity of the enzyme is directly correlated with the maximum catalytic current (Equation 4, where k_{cat} is the turnover frequency of the enzyme, i_{lim} is the maximum catalytic current obtained in an experiment where mass transport is not rate limiting, n is the number of electrons

involved, F is the Faraday constant, A is the electrode surface area, and Γ is the electro-active coverage of enzyme molecules) (Vincent et al., 2007; Leger et al., 2005).

$$k_{cat} = \frac{i_{\lim}}{n \cdot F \cdot A \cdot \Gamma} \quad (4)$$

Mass transport limitations are difficult to avoid in the case of hydrogenases due to their high catalytic activities and low $K_M^{H_2}$ values (Pershad et al., 1999). In order to overcome this, one can lower the enzyme film coverage. A fraction of the enzyme molecules can be removed by polishing the electrode surface (with damp cotton wool for example) so that the enzyme film behaves like an array of microelectrodes (Woolerton and Vincent, 2009; Vincent et al., 2007).

The electro-active coverage of enzyme molecules (Γ), necessary for the estimation of the turnover frequency (k_{cat}), can be determined from the area of the non-turnover peaks observed in cyclic voltammograms (Armstrong et al., 2009; Leger et al., 2002a; Jones et al., 2002). The non-turnover peaks are the result of reversible redox transitions of the bound redox-active metal cofactors (see Section 2.1.1.2). In the case of hydrogenases, the Fe-S clusters signals can be observed when the enzyme is completely inactivated (by an inhibitor such as CO) and the catalytic electron flow is blocked. Non-turnover peaks can only be obtained when the electro-active enzyme coverage is high (Jones et al., 2002; Pershad et al., 1999).

The main drawbacks of PFE with PGE electrodes are film loss and heterogeneity of interfacial electron-transfer rate constants. Because the enzyme molecules are attached to the electrode via non-covalent bonds, they can desorb from the surface. In addition,

the interaction with the PGE surface can destabilize the enzymes causing them to unfold during experiments (Blanford and Armstrong, 2006). The instability of the enzyme film complicates the evaluation of the parameters related to the electro-active coverage of enzyme molecules. The environments and the orientations of enzyme molecules are variable within the film. This non-homogeneous distribution leads to heterogeneity of interfacial electron-transfer rates, affecting the electron transfer kinetics between the surface and the enzymes and implicitly the shape of the voltammograms (Vincent et al., 2007). Instead of a current plateau at high potential, corresponding to the maximal turnover, recorded voltammograms typically display a residual slope. This is assumed to be caused by enzyme molecules that are not well coupled to the electrode requiring higher electrode potentials to ensure efficient interfacial electron transfer (Armstrong et al., 2009; Jones et al., 2003; Leger et al., 2002b).

1.1.3.2 Electrochemical investigations of O_2 tolerant MBHs

One of the first techniques used to study the O_2-tolerance of MBHs was gas chromatography. The employed assay involved mixing hydrogenase-containing membrane particles with H_2, O_2 and a redox dye acting as an artificial electron acceptor (e.g. methylene blue). Using such an artificial dye assay, Schink and Probst concluded that the MBH from *R. eutropha* is more stable in the presence of O_2 than in its absence (Schink and Probst, 1980). However, redox dyes undergo side reactions (especially in the presence of O_2) and this may lead to erroneous results. In addition, due to the low driving force imposed by the redox dye, electron transfer to the dye molecule limits enzyme turnover (Cammack et al., 1994). Protein film electrochemistry (PFE, described above) emerged as an alternative method allowing fast and easy measurements of

activity and overcoming the drawbacks of the methods involving redox dyes. Complementing spectroscopy and crystallography, PFE has provided valuable information regarding the kinetics and the thermodynamic determinants of H_2 oxidation/H^+ reduction catalysis by hydrogenases. Due to the difficulties posed by the isolation of the entire heterotrimeric complex (Frielingsdorf et al., 2011; Saggu et al., 2009), many of the electrochemical studies carried out so far, including the PFE-based ones, have employed only the heterodimeric (αβ) sub-complex of MBHs (Lubitz et al., 2014; Vincent et al., 2007).

1.1.3.2.1 The overpotential requirement

Cyclic voltammetry scans have revealed that the heterodimeric sub-complexes of O_2 tolerant MBHs display an overpotential for the onset of H_2 oxidation with respect to the thermodynamic potential of the $2H^+/H_2$ couple (Figure 1.6) (Lukey et al., 2010; Pandelia et al., 2010; Goldet et al., 2008; Vincent et al, 2005a). While the onset potential for H_2 oxidation of standard [NiFe] hydrogenases almost coincides with the reduction potential of the $2H^+/H_2$ couple, the MBHs from *E. coli*, *R. eutropha*, and *Aquifex aeolicus* require an overpotential of 0.05-0.08 V (Lukey et al., 2010; Pandelia et al., 2010; Goldet et al., 2008). The high potential at which electrons leave the protein through the distal [4Fe-4S] cluster in O_2 tolerant MBHs (-0.19 V in Hyd-1 compared to -0.3 V in Hyd-2 of *E. coli*) has been proposed to account for this property (Hexter et al., 2012).

1.1.3.2.2 Anaerobic inactivation

At high electrode potentials in anaerobic conditions, O_2 tolerant MBHs undergo oxidative inactivation (also termed “anaerobic inactivation”).

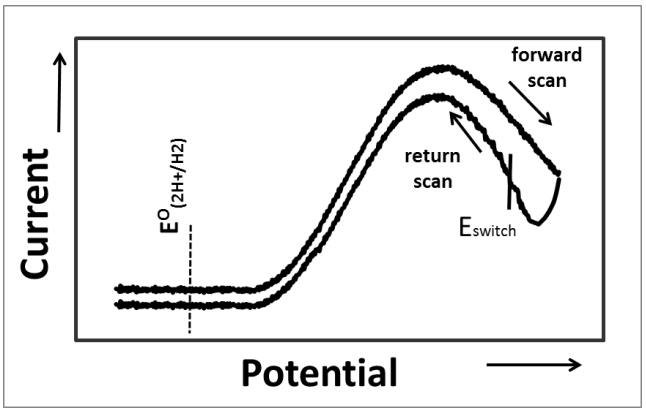

Figure 1.6 Schematic representation of a cyclic voltammogram of an O_2 tolerant MBH undergoing anaerobic inactivation. The thermodynamic potential of the $2H^+/H_2$ couple is marked with a vertical dashed line. E_{switch} is marked with a continuous vertical line.

As the potential is scanned towards positive values, the catalytic current drops and is restored by reductive reactivation on the return scan (Figure 1.6) (Bowman et al., 2014; Goris et al., 2013; Evans et al., 2013; Parkin et al., 2012; Lukey et al., 2011; Pandelia et al., 2010; Lukey et al., 2010; Armstrong et al., 2009; Goldet et al., 2008; Vincent et al., 2007; Vincent et al., 2005a). Spectroelectrochemical data has confirmed that the intermediate formed during high potential turnover conditions is the Ni-B state (Hidalgo et al., 2015).

It was observed that reductive reactivation is fast, consistent with Ni-B reactivation kinetics (Pandelia et al., 2010; Lukey et al., 2010; Goldet et al., 2008; Vincent et al., 2005a). In addition, the potentials at which O_2 tolerant MBHs undergo reactivation are higher compared to standard [NiFe] hydrogenases (Lukey et al., 2010; Vincent et al., 2005a). In order to compare the "ease" with which hydrogenases are reactivated, the "switch" potential (E_{switch}) was introduced as a qualitative parameter (Jones et al., 2003). The switch potential is the potential at which the maximal rate of current recovery is observed when the potential is scanned in the reductive direction. It is determined by

taking the local minimum of the first derivative of the current/potential profile (di/dE) in the high-potential region of the scan (Armstrong et al., 2009; Jones et al., 2003). The switch potential was found to be dependent on pH, indicating that the reactivation process is H^+-coupled (Jones et al., 2003), and also dependent on the employed scan rate (Fourmond et al., 2010). Standard [NiFe] hydrogenases have switch potentials around -0.1 V, while O_2 tolerant MBHs have values around +0.1 V (Vincent et al., 2005a). The extent of anaerobic inactivation observed in the case of O_2 tolerant MBHs is higher at slow scan rates and low H_2 concentrations (Lukey et al., 2010; Armstrong et al., 2009; Goldet et al., 2008). The full heterotrimeric MBH from *R. eutropha* directly adsorbed on a functionalized electrode surface showed the same catalytic response at high potential as the heterodimeric sub-complex. Electron transfer via the cytochrome *b* subunit was proved to be slow compared to the small subunit route. The enzyme displayed anaerobic inactivation to the same extent as the heterodimeric sub-complex (Sezer et al., 2011). The heterotrimeric MBH from *A. aeolicus*, embedded in lipid vesicles, displayed anaerobic inactivation even when using methylene blue as an electron mediator (Infossi et al., 2010).

1.1.3.2.3 O_2 tolerance

As mentioned before, O_2 tolerant MBHs can maintain H_2 oxidation activity in the presence of O_2 (Bowman et al., 2014; Parkin et al., 2012; Pandelia et al., 2010; Lukey et al., 2010; Vincent et al., 2005ab). Activity is inhibited fast upon O_2 injection, but the extent of inactivation is small compared to standard [NiFe] hydrogenases (Vincent et al., 2005a). The $K_{I(app)}^{O_2}$ for the MBH from *R. eutropha* has been determined to be around

110 μM at +0.122 V (pH 5.5, 30 ^{o}C), which is more than 20 times higher than the O_2 concentration required to completely inhibit the activity of the standard [NiFe] hydrogenases from *Allochromatium vinosum* (4 μM; +0.142 V; pH 5.6, 30 ^{o}C) and *Desulfovibrio fructosovorans* (5 μM; +190 V; pH 7; 40 ^{o}C) (Cracknell et al., 2009; Vincent et al., 2005b; Leger et al., 2004). $K_{I(app)}^{O_2}$, the inhibition constant for O_2 inhibition of H_2 oxidation, is defined as the concentration of O_2 required to attenuate H_2 oxidation activity by 50% (Cracknell et al., 2009). O_2 tolerance was found to increase with temperature and to decrease at higher electrode potentials (Cracknell et al., 2009; Vincent et al., 2005b). Protein film cyclic voltammetry showed that upon a short pulse of 90 μM O_2, the MBH from *R. eutropha* maintains 70% of its activity (Vincent et al, 2005a). In addition, the enzyme starts to recover activity before the complete removal of O_2 from the solution at potentials above + 0.150 V (Vincent et al, 2005a). A similar response after O_2 treatment was reported for the MBH (Hyd-1) from *E. coli* (Lukey et al., 2010). Protein film chronoamperometry showed that MBH from *R. eutropha* maintains more than 70% of the initial activity at -0.008 V at ambient concentrations of O_2 (Ludwig et al., 2009; Weiss, 1970; Whiple and Whipple, 1911). Activity recovery is complete after the removal of O_2 from the environment. Upon addition of increasing amounts of O_2, inactivation becomes more prominent and H_2 oxidation activity drops stepwise. After the addition of O_2, the current stabilizes after a period of time. This provides evidence supporting the hypothesis that O_2 reacts at the active site and that the origin of O_2-tolerance is not a simple physical exclusion of O_2 from the [NiFe] center. This was found to be in agreement with the hypothesized O_2 removal from the active

site by reduction to H_2O, which is transported away from the catalytic site through the network of water cavities (Fritsch et al., 2011a).

1.1.3.2.4 Affinity for H_2

The Michaelis-Menten constant for H_2 ($K_M^{H_2}$) under various conditions can be determined by analysing the activity decay following H_2 injection (transient measurements) or by H_2 titration (Lukey et al., 2010; Ludwig et al., 2009; Leger et al., 2004). In transient experiments, chronoamperometric traces are recorded following a short pulse of H_2. Stirring and gas purging (with N_2 or Ar) ensure the exponential decay of H_2 from the electrochemical cell. The current decay caused by the substrate depletion can be fitted to an equation (Equation 5) which describes the variation of current *i(t)* with time (*t*) following H_2 injection into the electrochemical cell to give an initial concentration $C_{H_2}(0)$ (Figure 1.7) (Ludwig et al., 2009; Leger et al., 2004).

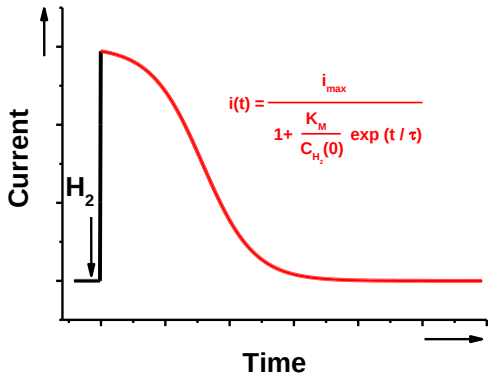

Figure 1.7 Schematic representation of a chronoamperogram
showing the current response during a hydrogenase transient experiment.
The catalytic response of a hydrogenase following a short pulse of H_2 can be fitted starting with the maximum activity region (red trace) to determine K_M.

The equation takes into account the exponential profile for the loss of H_2 from solution (τ is the time constant for exponential gas removal and i_{max} is the initial current) (Ludwig et al., 2009; Leger et al., 2004).

$$i(t) = \frac{i_{\max}}{1 + \frac{K_M}{C_{H_2}(0)} \cdot \exp(t/\tau)} \qquad (5)$$

$K_M^{H_2}$ values for the MBHs from *R. eutropha* and *R. metallidurans* have been determined to be 6 μM and 0.6 μM, respectively (- 0.108 V, pH 5.5, 30 ^oC) (Ludwig et al., 2009). In the case of the MBHs from *E. coli* the values are in the same range: around 9 μM for the O_2 tolerant Hyd-1 and 17 μM for the standard Hyd-2 (-0.175 V, pH 6, 30 ^oC) (Lukey et al., 2010). It is not clear whether the high affinity for H_2 of O_2 tolerant MBHs plays a role in O_2 tolerance. $K_M^{H_2}$ was found to increase with temperature and potential (Cracknell et al., 2009). O_2 tolerance of the MBH from *R. eutropha* increases at temperatures higher than 30 ^oC despite lower affinity for H_2 (high $K_M^{H_2}$). The increased tolerance correlates with the hypothesis that O_2 reacts at the active site. The reductase activity of [NiFe] hydrogenases has been demonstrated in the case of the O_2 tolerant NAD^+-reducing [NiFe]-hydrogenase from *R. eutropha* (k_{cat} = 2.03±0.13 s^{-1}) (Lauterbach and Lenz, 2013) and the O_2 tolerant Hyd-1 from *E. coli* (k_{cat} = 0.28 s^{-1}) (Wulff et al., 2014) using O_2 isotope measurements. However, it has also been determined, using both electrochemical and spectroscopic methods, that the presence of O_2 does not change the ratio of Ni-A/Ni-B state obtained in anaerobic oxidizing conditions for the standard [NiFe]-hydrogenase from *D. fructosovorans* (Abou Hamdan et al., 2013). Based on this, it has been suggested that the O_2 molecule acts only as an electron acceptor in the

vicinity of the active site. In conclusion, although the molecular determinants of O_2 tolerance have been elucidated to a great extent, the models proposed so far can only partially explain the catalytic properties of O_2 tolerant [NiFe] hydrogenases under oxidizing conditions.

1.1.3.2.5 H^+ reduction activity

H^+ reduction rates of O_2 tolerant MBHs are very low or zero at physiologically relevant pH values (Bowman et al., 2014; Lukey et al., 2010; Pandelia et al., 2010; Goldet et al., 2008). Consequently, the H^+ reduction catalytic currents are very low compared to the H_2 oxidation currents. The lower limit for the turnover frequency for H_2 production by the MBH in *R. metallidurans*, in the presence of O_2, was estimated to be around 70 H_2 molecules per second (-0.45 V, pH 5.5, 40 ^oC) (Goldet et al., 2008). Product inhibition was found to be very strong ($K_I^{app}(H_2)$ = 7.1 ± 1.6 μM for *R. eutropha* MBH and 10.8 ± 1.2 μM for *R. metallidurans* MBH). It was shown that Hyd-1 from *E. coli* can become an efficient H_2 producer at pH values below 4 (Murphy et al., 2014). One possible cause for the strong bias of O_2 tolerant MBHs towards H_2 oxidation is considered to be the high midpoint potentials of the [FeS] clusters which might hinder the electron flow from the electron relay to the [NiFe] active site (Murphy et al., 2014; Goldet et al., 2008).

1.1.3.2.6 CO inhibition

H_2 oxidation activity of the MBHs from *A. aeolicus* and *R. eutropha* is not inhibited by CO (Luo et al., 2009; Vincent et al., 2005b). In the case of the MBH from *E.coli*, CO reversibly inhibits the H_2 oxidation activity ($K_I^{app}(CO)$ = 51 ± 6 μM at -0.06 V, under

20% H_2, pH 6, 20 ^oC) (Lukey et al., 2010). Full recovery of activity is observed upon removal of the inhibitor.

CO inhibition of H^+ reduction activity was found to be weaker than H_2 inhibition. The H^+ reduction activity of *R. eutropha* MBH is reversibly inhibited by CO and full recovery is observed after complete removal of the inhibitor ($K_I^{app}(CO)$ = 1.7±0.11 mM, -0.45 V, pH 5.5, 30 ^oC). The same behaviour was reported for the MBH from *R. metallidurans* ($K_I^{app}(CO)$ = 1.2±0.06 mM, -0.45 V, pH 5.5, 30 ^oC) (Goldet et al., 2008).

1.2 [FeFe] Hydrogenases

[FeFe] Hydrogenases are present in prokaryotes as well as in eukaryotes (Mulder et al., 2011; Vignais and Billoud, 2007). Sequence analogues of [FeFe]-hydrogenase have been found in genomes of higher eukaryotes including the human genome (Vignais and Billoud, 2007). [FeFe] hydrogenases are found in single or multiple subunit form. The active metal centre is a binuclear [FeFe] centre, which is bound to a [4Fe-4S] cluster via a bridging cysteine residue of the protein (Figure 1.8). The metal centre and the bound [FeS] cluster form the so-called "H-cluster". In some [FeFe] hydrogenases, accessory [FeS] clusters, apart from the one in the H-cluster, are accomodated in the catalytic subunit or the additional subunits. Each active site Fe atom is coordinated to one CN^- and one CO ligand (Fontecilla-Camps et al., 2007). The two Fe atoms are connected with one another through a CO ligand and two bridging sulphur ligands of an azadithiolate cofactor (Berggren et al., 2013; Esselborn et al., 2013). The Fe atom distal

to the [FeS] cluster has an open coordination site where the substrate binding site is presumed to be located (Lemon and Peters, 1999).

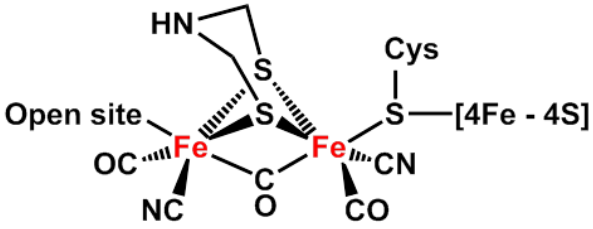

Figure 1.8 The structure of the H-cluster of [FeFe]-hydrogenases.
The open site is thought to be the H_2 binding site.

Catalysis involves cycling of the H-cluster between states known as H_{ox} {[4Fe-4S]$^{2+}$-Fe(I)Fe(II)} and H_{red} {[4Fe-4S]$^{2+}$-Fe(I)Fe(I)}. Both states have been detected in all [FeFe] hydrogenases studied so far with FTIR (Lubitz et al., 2014). One electron reduction of H_{red} leads to the "super-reduced state" H_{sred} {[4Fe-4S]$^{+}$-Fe(I)Fe(I)}. This state has been shown to be active and consequently proposed to be also part of the catalytic cycle (Adamska et al., 2012; Silakov et al., 2009). A more recent PFE study found that accumulation of H_{sred} is associated with activity loss, questioning the involvement of the intermediate in the catalytic cycle (Haji et al., 2014).

In the presence of O_2, [FeFe] hydrogenases show varying catalytic responses. The [FeFe] hydrogenase from *Desulfovibrio desulfuricans* loses most of its activity after a short pulse of O_2, undergoing irreversible inactivation (Parkin et al., 2006; Vincent et al., 2005a). As with [NiFe] hydrogenases, [FeFe] hydrogenases also undergo reversible inactivation at oxidizing electrode potentials in anaerobic conditions. The so-called H_{ox}^{inact} state that is generated under oxidizing conditions has been hypothesized to protect the enzyme from O_2 damage (Parkin et al., 2006), which was shown to take place at the

H-cluster (Swanson et al., 2015; Stripp et al., 2009). Unlike the [FeFe] hydrogenase from *D. desulfuricans*, the [FeFe] hydrogenases from *Clostridium acetobutylicum* and *Chlamydomonas reinhardtii* maintain activity in the presence of O_2 (Orain et al., 2015; Goldet et al., 2009; Baffert et al., 2008). Inhibition by O_2 is only partial and after the removal of the inhibitor, activity is partially recovered. The *C. acetobutylicum* [FeFe] hydrogenase recovers activity even after encountering O_2 concentrations that normally completely and irreversibly inhibit the [FeFe] hydrogenase from *D. desulfuricans* or the standard [NiFe] hydrogenases from *A. vinosum* and *Desulfovibrio gigas*. The rate constant for the reaction with O_2 for the *C. acetobutylicum* [FeFe] hydrogenase was estimated to be eight to ten times smaller than in the case of standard [NiFe] hydrogenases (Liebgott et al., 2010b; Baffert et al., 2008; Leger et al., 2004). Moreover, the rate of anaerobic inactivation for the *C. acetobutylicum* [FeFe] hydrogenase was estimated to be one order of magnitude smaller than for the [FeFe] hydrogenase from *D. desulfuricans* (Baffert et al., 2008). The understanding of the molecular mechanism of O_2 tolerance of [FeFe] hydrogenases is yet not as advanced as in the case of [NiFe] hydrogenases. Further studies are required to elucidate the structural characteristics that confer O_2 tolerance.

A direct comparison of the turnover frequencies of [FeFe] hydrogenases and [NiFe] hydrogenases has proved difficult due to the limitations imposed by the enzyme immobilisation at the electrode surface and the difficulties associated with the estimation of the electroactive coverage. The H_2 production turnover frequency of *C. acetobutylicum* [FeFe] hydrogenase was determined to be 1000 s^{-1} at -0.7 V when the enzyme was adsorbed on a mercapto-carboxylic acid self-assembled monolayer formed

on a flat gold electrode and the coverage was determined via electrochemical scanning tunnelling microscopy (Madden et al., 2012). By comparison, the [NiFeSe] hydrogenase from *Desulfomicrobium baculatum*, adsorbed at a graphite surface, has a H_2 production turnover frequency of 750 s^{-1} at -0.55 V (Parkin et al., 2008). The H_2 oxidation turnover frequency of *C. acetobutylicum* [FeFe] hydrogenase is around 16000 s^{-1}, as determined from spectrophotometric assays (Liebgott et al., 2010b). The H_2 oxidation turnover frequency of *D. baculatum* [NiFeSe] hydrogenase, determined via PFE experiments, is four times lower. Other [NiFe] hydrogenases, like the ones from *Desulfovibrio vulgaris* Miyazaki F and *Citrobacter* sp. S-77, adsorbed onto carbon black, have reported H_2 oxidation turnover frequencies of 14,100 s^{-1} and 893,000 s^{-1}, respectively (Matsumoto et al., 2014).

1.3 [Fe] hydrogenases

[Fe] hydrogenases catalyse only one step in the reduction of CO_2 to CH_4 (Thauer et al., 2010; Vignais and Billoud, 2007) and methanogenic archaea are the only organisms known to harbour these enzymes (Thauer et al., 2010). [Fe] hydrogenases are dependent on methenyl-tetrahydromethanopterin (methenyl-H_4MPT^+) as a substrate. Using H_2, they reduce methenyl-H_4MPT^+ to methylene-H_4MPT (Figure 1.9). The reaction is reversible and, consequently, [Fe] hydrogenases have also been designated as "H_2 forming methylene-tetrahydromethanopterin dehydrogenases" (Hmd) (Lubitz et al., 2014). Hmd is essential only under specific growth conditions of Ni limitation (Thauer et al., 2010; Vignais and Billoud, 2007). Unlike [NiFe] and [FeFe] hydrogenases, [Fe] hydrogenases do not reduce artificial redox dyes (Zirngibl et al., 1992).

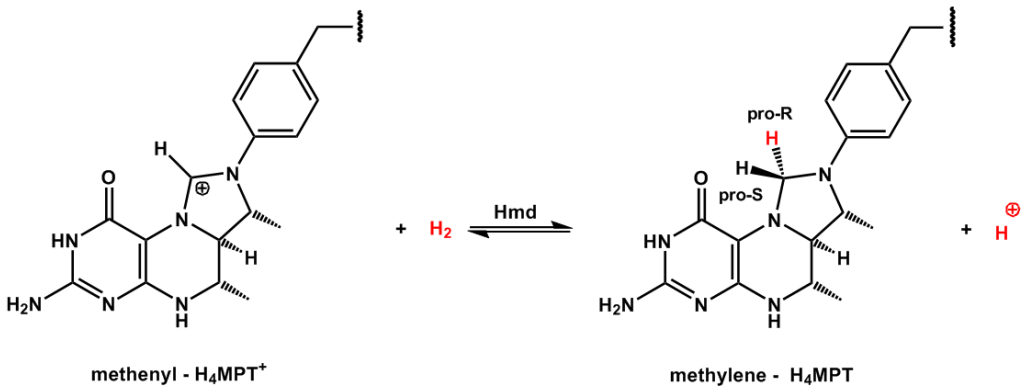

Figure 1.9 The stereoselective transfer of a hydride from H_2 to a pterin substrate catalysed by Hmd.

The nature of the coordination sphere of Fe in [Fe]-hydrogenases resembles that of the Fe atom in the binuclear active sites of [FeFe]-hydrogenases and [NiFe]-hydrogenases (Heinekey, 2009). The Fe atom is coordinated to two CO ligands, one S atom of a cysteine residue, one N atom from the pyridine ring of a guanylylpyridinol cofactor, and one carbonyl group belonging to the same guanylylpyridinol cofactor (Figure 1.10). The enzyme does not contain any Fe-S clusters, being sometimes referred to as "Fe-S cluster-free hydrogenase". [Fe] hydrogenases have been identified in *Methanothermobacter marburgensis*, *Methanocaldococcus jannaschii* and *Methanopyrus kandleri*.

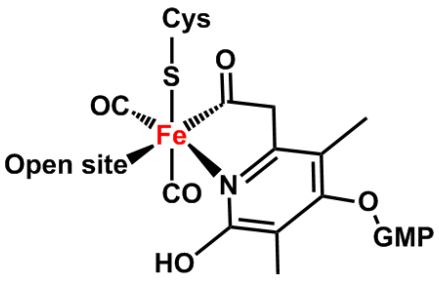

Figure 1.10 Active site structure of [Fe]-hydrogenases (GMP, guanidine monophosphate).

1.4 Hydrogenases in biofuel cells

H_2 is considered a viable fuel for storing excess energy generated by wind, solar and hydrothermal power plants (de Poulpiquet et al., 2014). During periods of low energy demand, excess electrical energy could be used to produce H_2 by water electrolysis (Wakerley and Reisner, 2015). Reconversion to electricity can be done by oxidizing H_2 in fuel cells, which are known to have significantly higher efficiencies than combustion engines (Sahaym and Norton, 2008; Cracknell et al., 2008b; Atkins and de Paula, 2006; Adzic et al., 2006; Ahluwalia et al., 2006). H_2 has a higher energy density (120 MJ/kg) than methane (55 MJ/kg). In addition, its combustion produces only water and its production can be achieved from wastewater (Lin et al., 2012).

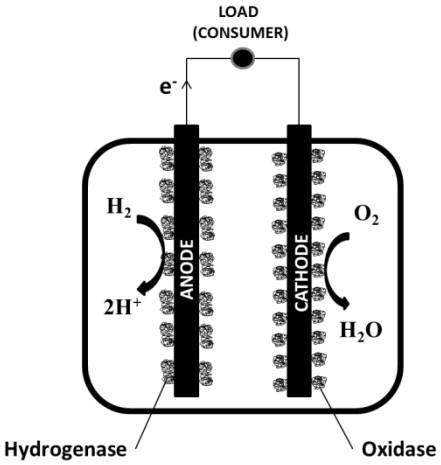

Figure 1.11 Schematic representation of a membrane-less bio-fuel cell employing hydrogenase at the anode and oxidase at the cathode.

The widespread exploitation of fuel cells remains a challenge due to the high operating cost imposed by the expensive Pt electrocatalyst and the anode/cathode separating membrane. The use of hydrogenases as catalysts for H_2 oxidation, coupled with O_2 reduction catalysed by laccases/bilirubin oxidases, would eliminate the need for an ion

selective membrane due to their high substrate selectivity (Figure 1.11). In this instance, direct electron transfer must be ensured between the enzyme and the electrode surface. Water-soluble redox mediators do not constitute an option as their short-circuit reactions require the use of a separating membrane between the anode and the cathode compartment.

The performance of hydrogenases in membrane-less fuel cells is limited by enzyme desorption and inactivation. Attachment to the electrode via covalent bonds provides a better control of orientation and achieves a higher protein film stability compared to adsorption onto graphite surfaces widely used in mechanistic studies (e.g. PFE). The use of covalent attachment leads to increased enzyme stability and higher current densities compared to the protein adsorption approach (Krishnan and Armstrong, 2012). Further improvements are possible by increasing the catalyst load. A single hydrogenase active site is enveloped in a bulky protein matrix, which means that the maximum current density is limited by the protein coverage of the electrode. Covalent attachment to carbon nanotubes significantly increases current density and long-term electrode stability, providing a promising approach for the efficient exploitation of hydrogenase-based electrodes (de Poulpiquet et al., 2013; Xu and Armstrong, 2013; Ciaccafava et al., 2012; Alonso-Lomillo et al., 2007).

The operating potential window of hydrogenases in membrane-less fuel cells is restricted by O_2 inactivation and oxidative (high potential) inactivation. Despite employing O_2-tolerant hydrogenases, the power output decreases due to O_2 inactivation, which is fast at the positive potentials imposed during operation (Wait et al., 2010; Vincent et al., 2006; Vincent et al., 2005b). Under low H_2 concentrations (<4%, below

the flammability range) when the fuel cell output is limited by the anode, anaerobic inactivation due to the increasingly positive potential of the hydrogenase electrode further decreases the power output. Hydrogenase reactivation can be done by connecting a second “fresh” hydrogenase anode, which serves as an external source of electrons (Wait et al., 2010).

Protection from inactivation was achieved by incorporating hydrogenases into redox hydrogel films (Oughli et al., 2015; Plumere et al., 2014; Baur et al., 2011; Karyakin et al., 2005). The approach was successfully validated with standard [NiFe] hydrogenases, a [NiFeSe] and a [FeFe] hydrogenase used as anodic catalysts. A viologen-functionalized polymer was used as a protective matrix that prevents both O_2-induced and anaerobic oxidative inactivation (Oughli et al., 2015; Plumere et al., 2014). The viologen functionalities mediate electron transfer from the hydrogenase active site to the electrode. The redox buffering of the viologen couple at -0.3 V prevents anaerobic inactivation of the hydrogenase. Protection from aerobic inactivation is ensured by physical exclusion of O_2 and by viologen-catalized O_2 reduction at the surface of the hydrogel film (Plumere et al., 2014).

A better understanding of the catalytic and (in)activation mechanisms of hydrogenases is needed for improving the strategies of designing and optimizing synthetic catalysts that would match the catalytic performances of hydrogenases and, at the same time, overcome the drawbacks of current (bio)fuel cell technologies in terms of catalyst loading and lifetime.

The work described in this thesis was performed with the aim of investigating the catalytic properties of the heterotrimeric membrane-bound [NiFe] hydrogenase (HoxGKZ) by comparison to the heterodimeric sub-complex (HoxGK), which was thoroughly studied via an array of techniques including protein film electrochemistry. The heterotrimeric MBH was probed in its native lipid environment in equilibrium with the quinone pool in the tethered lipid bilayer membrane (see Section 2.2.4.1). Anaerobic and aerobic oxidizing conditions have been employed in order to obtain insights into the inactivation/reactivation and O_2 tolerance mechanism of MBHs. The role of the [FeS] electron relay in (re)activation was studied by probing a variant with the same electron relay configuration as standard (O_2 sensitive) [NiFe] hydrogenases.

2. Electrochemistry and electrodes

2.1 Electrochemical methods

2.1.1 Cyclic voltammetry

Cyclic voltammetry is a technique used to acquire information on the thermodynamics and kinetics of electron-transfer processes. It consists of linearly scanning the potential (E) of a working electrode using a triangular potential waveform (Figure 2.1) and measuring the current response (i). The potential of the working electrode is controlled versus a reference electrode with a stable and well-known potential using a potentiostat. The rate at which the working electrode potential is changed is termed scan rate or potential ramp (v in Equation 6 where t is time).

$$v = \frac{dE}{dt} \quad (6)$$

The direction of scan is reversed at the so-called switching potential (Figure 2.1). The plot of the applied potential versus the resulted current is called a cyclic voltammogram or a current-voltage curve (i-E curve) (Bard et al., 2003; Bard and Faulkner, 2001; Zoski, 2001; Wang, 2000; Kissinger and Heineman, 1983).

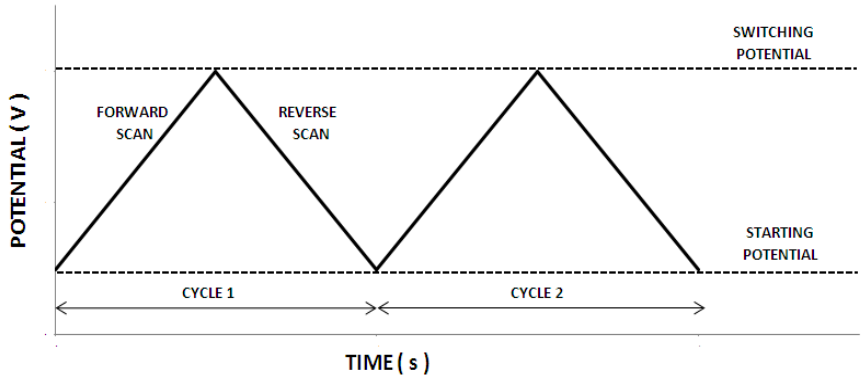

Figure 2.1 Typical excitation signal for cyclic voltammetry.

The shape of a voltammogram depends on the electron-transfer kinetics and on mass transport processes at the electrode surface. According to an equation derived from the *Butler-Volmer model*, the electron-transfer rate constant is an exponential function of the applied potential (Equations 7 and 8).

$$k_{ox} = k^o \cdot \exp\cdot\left[\frac{(1-\alpha)\cdot n\cdot F}{R\cdot T}\cdot\left(E-E^o\right)\right] \quad (7)$$

$$k_{red} = k^o \cdot \exp\cdot\left[\frac{-\alpha\cdot n\cdot F}{R\cdot T}\cdot\left(E-E^o\right)\right] \quad (8)$$

In equations 7 and 8, k_{ox} and k_{red} are the electron-transfer rate constants (cm s^{-1}) for oxidation and reduction, respectively, k^o is the standard heterogeneous electron-transfer rate constant, α is the transfer coefficient (dimensionless parameter, between zero and unity), n is the stoichiometric number of electrons involved in the electrode reaction, F is Faraday's constant (C mol^{-1}), R is the universal gas constant (J $mol^{-1} \cdot K^{-1}$), T is the absolute temperature (K), E is the applied electrode potential (V), and E^o is the formal redox potential of the redox couple (V). The transfer coefficient, α, is a measure of the fraction of energy that is supplied to the system (in the form of applied potential) which

is used to actually lower the activation energy barrier (Zoski, 2001; Wang, 2000; Mabbott, 1983).

According to the Marcus theory of electron transfer, the rate of electron transfer (k_{et}) depends on the distance between the donor and the acceptor molecules, the reaction Gibbs energy for electron transfer ($\Delta_r G$), and the reorganization energy λ (Equation 9, where *h* is Planck's constant). Electron transfer becomes more efficient with decreasing donor to acceptor distance and with increasing exergonicity (Bard et al., 2003; Bard and Faulkner, 2001).

$$k_{et} = \frac{2\langle H_{DA}\rangle^2}{h}\left(\frac{\pi^3}{4\lambda RT}\right)^{1/2} e^{-\Delta^{\neq}G/RT} \quad (9)$$

The $\langle H_{DA}\rangle$ term in Equation 9 accounts for the electronic coupling between the donor and the acceptor molecule. The reorganization energy λ represents the energy required for the structural rearrangements of the donor, acceptor, and medium (solvent) molecules during electron transfer. The Gibbs energy of activation, $\Delta^{\neq}G$, is related to the reaction Gibbs energy for electron transfer, $\Delta_r G$, in the following way:

$$\Delta^{\neq}G = \frac{(\Delta_r G + \lambda)^2}{4\lambda} \quad (10)$$

The model predicts that the electron transfer rate increases as the reorganization energy matches the reaction Gibbs energy, $\Delta_r G$. Equation 9 is useful for estimating electron transfer rates for processes with weak electron coupling between acceptor and donor molecules (as it is the case with protein complexes). For cases in which the

overpotential ($|E-E^o|$) is smaller than the reorganization energy of the redox process taking place, the Marcus model can be considered as analogous to the *Butler-Volmer model* (Vincent et al., 2007; Atkins and de Paula, 2006).

2.1.1.1 Diffusion controlled cyclic voltammetry

Based on the value of k^o (in the Butler-Volmer model), redox couples can be classified as reversible, quasi-reversible, or irreversible. For reversible redox couples ($k^o > 10^{-1}$ cm s^{-1}), the current depends only on mass transport (Wang, 2000; Heinze, 1984). For quasi-reversible reactions, k^o lies in the range of 10^{-1} to 10^{-5} cm s^{-1} and the current response is controlled by both the electron transfer and mass transport. In the case of an irreversible redox process ($k^o < 10^{-5}$ cm s^{-1}), the current is mainly controlled by the rate of the charge transfer.

The voltammogram of a reversible redox couple analyzed on a stationary planar working electrode immersed in a stationary electrolyte solution constitutes the simplest case. For simplification, it is assumed that only the reduced species (*Red*) is present in solution at the beginning of the experiment. As the redox reaction is reversible, interfacial electron transfer is fast with respect to the rate of mass transport of the redox-active species. The concentration ratio for the reduced and the oxidized species at the electrode surface at a given potential can thus be determined from the *Nernst equation* (Equation 11).

$$E = E^o - \frac{R \cdot T}{n \cdot F} \cdot \ln \frac{C_{\mathrm{Re}d}(0,t)}{C_{Ox}(0,t)} \quad (11)$$

$C_{Red}(0,t)$ and $C_{Ox}(0,t)$ in Equation 11 are the surface concentrations of the reduced (*Red*) and the oxidized (*Ox*) species respectively (Zoski, 2001).

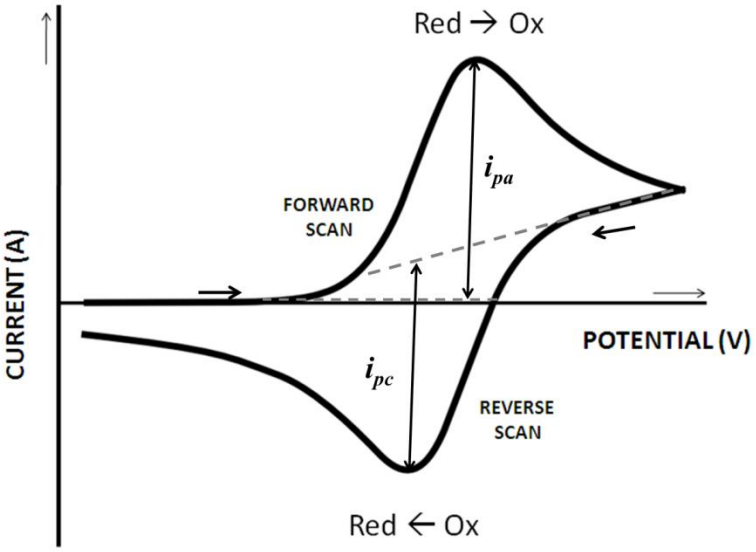

Figure 2.2 Cyclic voltammogram for an ideal reversible redox couple (adapted from Heinze, 1984; Mabbott, 1983; Kissinger and Heineman, 1983). The magnitude of the anodic (i_{pa}) and the cathodic (i_{pc}) peak currents is marked with double-headed arrows. Baseline extrapolations are presented in gray dashed lines.

The starting potential for the experiment is chosen such that electrolysis of the reduced species (*Red*) is completely avoided when the electrode is switched on (Figure 2.2). As the potential is scanned positively, on the forward scan, an anodic current (faradaic current) emerges as *Red* is oxidized to *Ox* (*Red* → *Ox* + ne^-). As the reactant is depleted from the electrode surface a limiting current plateau is reached and then the anodic current starts to decrease. When the switching potential is reached, the direction of scan is reversed. As the potential is scanned towards negative values, the oxidized species generated during the forward scan is reduced back to *Red* (*Ox* + ne^- → *Red*) and a cathodic current peak arises having the same shape as the anodic peak.

The evolution of the current response as a function of potential during the cyclic voltammetry experiment can be explained by taking into account the mass transport phenomena taking place at the surface of the electrode. A diffusion layer is formed near the surface of the working electrode during the potential scan. The change in surface concentration of the redox active species determines the variation of the current response. According to an application of Fick's first law of diffusion (Equation 12), the current response at any time is proportional to the concentration gradient of the reactant (i.e. *Red*).

$$i = n \cdot F \cdot A \cdot D \cdot \left(\frac{\partial C}{\partial x} \right)_{x=0} \quad (12)$$

In Equation 12, i is the current (A), A is the electrode area (cm^2), D is the diffusion coefficient of the species of interest ($cm^2\ s^{-1}$), C is the concentration of the electroactive species (mol cm^{-3}), and x is the perpendicular distance from the electrode (cm).

Based on Equation 12, the current recorded at a certain potential can be correlated to the slope of the corresponding concentration-distance profile (Figure 2.3). The concentration gradient of the reduced species, $(\partial C_{Red}/\partial x)_{x=0}$, is zero at the beginning of the experiment (just above the starting potential) and the resulting current is, accordingly, zero (Figure 2.3A). As the potential is swept towards the value of the formal redox potential of the couple, the concentration gradient increases and the anodic current increases correspondingly (Figure 2.3B). When the reduced species is depleted from the electrode surface, the current starts to decrease (Figure 2.3C). After the direction of the scan is reversed the potential is lowered. The oxidized species

accumulated at the surface of the electrode will undergo reduction as the potential is dropping towards the formal redox potential. Now, the concentration gradient of the oxidized species, $(\partial C_{Ox}/\partial x)_{x=0}$, increases and the cathodic current increases correspondingly.

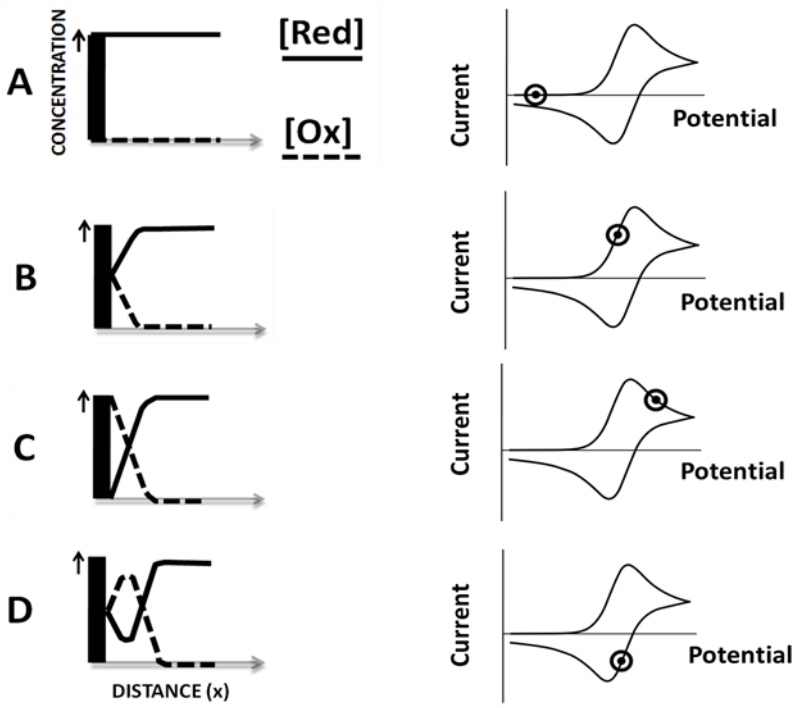

Figure 2.3 Graphical representation of the concentration-distance profiles for selected potentials during a cyclic voltammetry experiment in an unstirred solution and the corresponding current response points on the cyclic voltammogram: (A) immediately after the start of the experiment; (B) in the range of the formal redox potential on the forward scan; (C) at zero reactant surface-concentration; (D) in the range of the formal redox potential on the reverse scan (adapted from Heinze, 1984; Mabbott, 1983; Kissinger and Heineman, 1983).

The current decrease observed after the depletion of the electroactive species (i.e. after the current has reached a peak) is independent of the applied potential, following a $t^{-1/2}$ dependence.

For a reversible electrochemical couple, the peak current (i_p in Figure 2.2) is dependent on the bulk concentration of the redox species and increases with the square root of the scan rate (Equation 13 – the *Randles-Sevcik equation*). The ratio between the anodic-to-cathodic peak currents (i_{pa}/i_{pc}) is close to unity. This ratio changes when electron transfer processes are coupled with chemical reactions. The peak heights are determined by extrapolating the preceding baseline current (Figure 2.2). The correct determination of the baseline is essential for an accurate measurement of the peak current (Zoski, 2001; Wang, 2000; Heinze, 1984).

$$i_p = 2.69 \cdot 10^5 \cdot n^{3/2} \cdot A \cdot D^{1/2} \cdot C \cdot \nu^{1/2} \quad (13)$$

The position of the peaks on the potential axis is related to the formal potential of the redox process. The formal redox potential is equal to the average of the reduction potential (E_{pc}) and the oxidation potential (E_{pa}) when the diffusion coefficients of the reduced and the oxidized species have the same value (Equation 14).

$$E^o = \frac{E_{pc} + E_{pa}}{2} \quad (14)$$

The separation between the peak potentials can be used to determine the number of transferred electrons or to estimate the deviation from the ideal Nernstian electrochemical behaviour of the investigated system (Equation 15, valid at 25 ^{o}C).

$$\Delta E_p = E_{pa} - E_{pc} = \frac{0.059}{n} \quad (15)$$

In the case of irreversible couples, peak currents depend on the value of α (Equation 16).

$$i_p = \left(2.99 \cdot 10^5\right) \cdot \alpha^{1/2} \cdot A \cdot C \cdot D^{1/2} \cdot \nu^{1/2} \quad (16)$$

Due to slow electron transfer, the peak potentials (E_p) shift with the scan rate (Equation 17).

$$E_p = E^o - \frac{R \cdot T}{\alpha \cdot F} \cdot \left[0.78 + \ln\left(\frac{D^{1/2}}{k^o} \right) + \ln\left(\frac{\alpha \cdot F \cdot \nu}{R \cdot T} \right)^{1/2} \right] \quad (17)$$

In the absence of mass transport limitations, the current response for a reversible electrochemical couple depends on the surface concentration of the electroactive species, the electrode potential, and the standard electron-transfer rate constant (the Butler-Volmer equation; Equation 18).

$$i = n \cdot F \cdot A \cdot k^o \cdot \left\{ \begin{array}{l} C_{\mathrm{Red}}(0,t) \cdot \exp\left[-\alpha \cdot n \cdot F \cdot \left(E - E^o\right) / R \cdot T \right] \\ -C_{Ox}(0,t) \cdot \exp\left[\left(1-\alpha\right) \cdot n \cdot F \cdot \left(E - E^o\right) / R \cdot T \right] \end{array} \right\} \quad (18)$$

2.1.1.2 Catalytic cyclic voltammetry

Cyclic voltammetry can also be employed in the study of electroactive species adsorbed or bound to the electrode surface. In this case, no concentration profile develops. The peak current is proportional to the surface coverage (Γ) and the potential scan rate (Equation 19).

$$i_p = \frac{n^2 \cdot F^2 \cdot \Gamma \cdot A \cdot \nu}{4 \cdot R \cdot T} \quad (19)$$

The quantity of charge (Q) transferred during a redox process (calculated from the peak area) can be used to determine the surface coverage of the species undergoing conversion (Equation 20).

$$Q = n \cdot F \cdot A \cdot \Gamma \quad (20)$$

An ideal adsorbed electro-active catalytic species, like a redox protein or a transition metal complex redox catalyst, undergoing reversible uncoupled electron transfer in the absence of substrate gives rise to symmetrical oxidation and reduction waves with no peak separation (Figure 2.4) (Le Goff et al., 2009; Wang, 2000; Hirst and Armstrong, 1998; Heering et al., 1998; Chidsey et al., 1991).

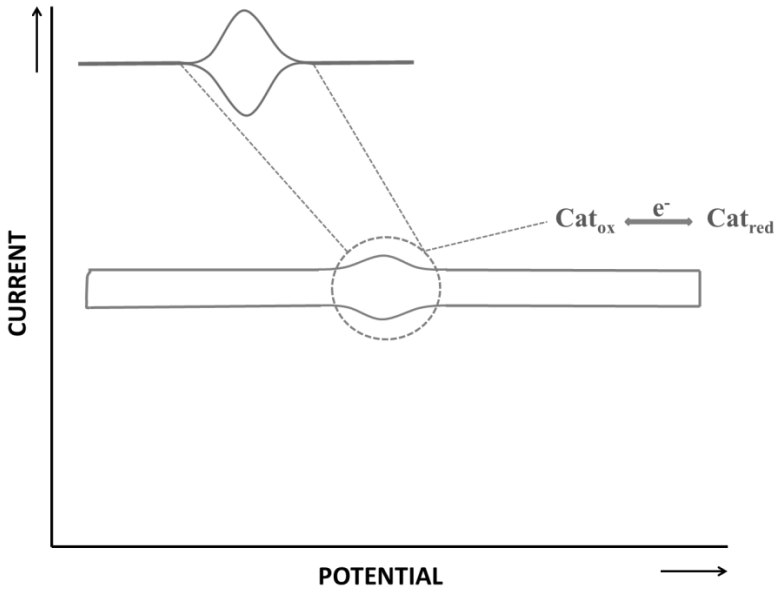

Figure 2.4 Schematic representation of a voltammogram of an ideal surface-confined catalyst (Cat) under non-turnover conditions revealing non-catalytic peaks typical of reversible catalysts. Depicted in the upper left corner are the background-subtracted non-turnover peaks.

During catalytic turnover, in the absence of mass transport limitations, the catalyst cycles between reduced and oxidized states as it conveys electrons to/from the electrode

for the oxidation/reduction of the substrate (Figure 2.5) (Bard et al., 2003; Leger et al., 2003; Armstrong et al., 1997). The value of the current in the plateau region of the voltammogram (i_∞) is a function of the catalytic rate constant, k_{cat} ($i_\infty = k_{cat} \cdot Q$). When substrate diffusion is limiting the catalytic conversion, the voltammetric response resembles the one described in Section 2.1.1.1.

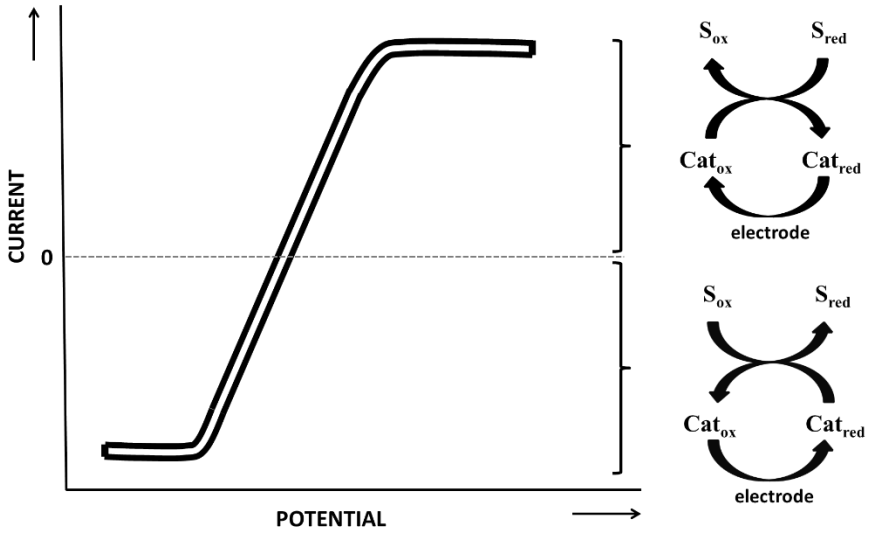

Figure 2.5 Schematic representation of a voltammogram of an ideal surface-confined catalyst (Cat) under turnover conditions, i.e. in the presence of the substrate "S", revealing the catalytic wave shape typical for reversible catalysts (a steady-state flux of substrate is typically ensured under turnover conditions by mixing the solution in the electrochemical cell or rotating the working electrode at high speed).

2.1.2 Chronoamperometry

Chronoamperometry consists of stepping the potential of the working electrode from a value at which no faradaic current is flowing to a value at which a redox process takes place (the current response is monitored as a function of time) (Bard et al., 2003; Bard and Faulkner, 2001; Zoski, 2001; Wang, 2000). Chronoamperometry can be used to study mechanisms of electrode processes as well as for determining working electrode surface areas, diffusion coefficients or the quantity of adsorbed electro-active species. A

multitude of potential steps can be employed, giving rise to complex potential sequences. The simplest involves a single potential step (Figure 2.6A).

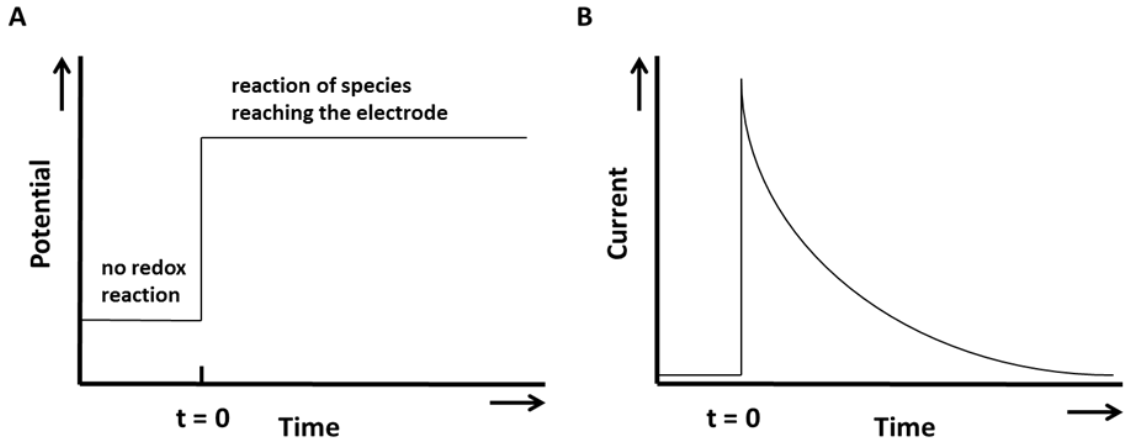

Figure 2.6 Chronoamperometric experiment: (A) the applied excitation / potential-time waveform; (B) the current-time response corresponding to the perturbation described in (A) in the case of a diffusion-limited system.

In the case of diffusion-limited systems, the corresponding current response will consist of a sharp change from zero to a maximum/minimum value followed by a relaxation back to zero (Figure 2.6B). The current-time curve reflects the change in concentration gradient of the electroactive species in the vicinity of the surface. At a planar electrode, the response current decays with the square root of time (Figure 2.6B). Such a decay is described by the *Cottrell equation* (Equation 21).

$$i(t) = \frac{n \cdot F \cdot A \cdot C \cdot D^{1/2}}{\pi^{1/2} \cdot t^{1/2}} \quad (21)$$

In the case of systems that are not diffusion-limited, the corresponding current response will consist of a sharp change from zero to a maximum/minimum value followed by a constant current level. When a catalytic system is adsorbed on the electrode (see Section 1.1.3.1 and 2.1.1.2) and an inhibitor is injected alongside the continuous supply of

substrate, a drop in current will be observed (Figure 2.7). This allows the probing of the inhibition kinetics, especially in combination with complex potential step sequences that are used to poise the catalyst being investigated in various redox states.

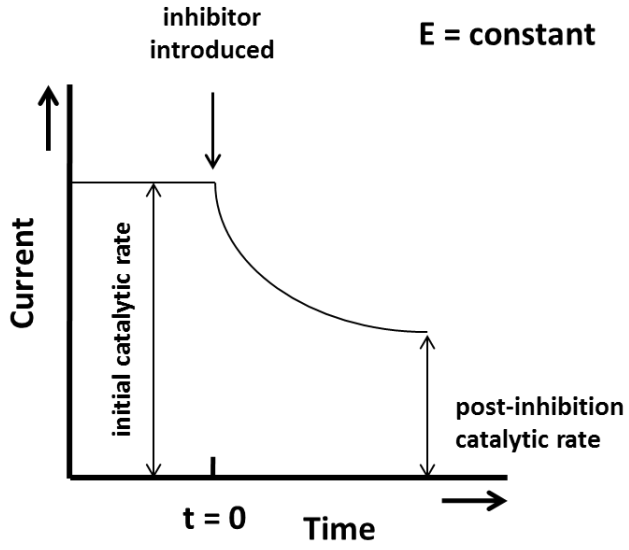

Figure 2.7 Chronoamperometric experiment showing the evolution of the recorded current upon the introduction of an inhibitor in the electrochemical cell (the electrode potential is held constant and stirring ensures that the supply of substrate is not diffusion-limited; t=0 is the time of injection of the inhibitor).

It is important to note that the use of potential steps leads to the occurrence of capacitive currents due to changes in the charge of the electrolyte double layer at the electrode interface on applying the step. The capacitive current occurs in parallel to the faradaic current and contributes to the overall current response. The double layer charging can be estimated by carrying out replicate experiments in the absence of the redox active species being investigated.

2.1.3 Electrochemical impedance spectroscopy

Electrochemical impedance spectroscopy (EIS) consists of applying small amplitude periodic (usually sinusoidal) electrical perturbations and monitoring the electrical

response over a range of perturbation frequencies. It is a noninvasive technique that can be used for investigating bulk as well as interfacial electrochemical processes (Bard et al., 2003; Zoski, 2001; Macdonald, 1992). The amplitude of the applied perturbations is small enough to give rise to a linear response of the system at steady state (Figure 2.8).

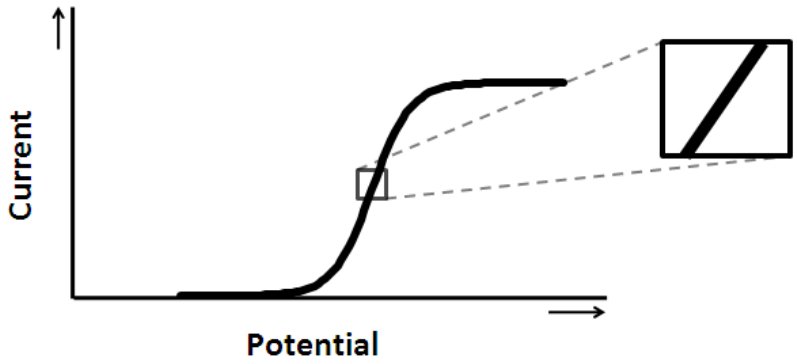

Figure 2.8 Current-voltage domain showing pseudo-linearity.

In a linear (or pseudo-linear) system, a sinusoidal perturbation of the applied voltage at time *t* (E(t); Equation 22) will generate a sinusoidal current response (i(t)) at the same frequency and shifted in phase (Equation 23).

$$E(t) = E_0 \cdot \sin(\omega \cdot t) \quad (22)$$

$$i(t) = i_0 \cdot \sin(\omega \cdot t + \Phi) \quad (23)$$

E_0 is the voltage amplitude, i_0 is the current amplitude, ω is the radial frequency (rad s^{-1}), and Φ is the phase angle. Radial frequency is related to frequency f (measured in Hz) in the following way: $\omega = 2\pi f$.

The electrochemical impedance of an electrochemical cell (Z) is defined as the ratio between the voltage across the cell ($E(t)$) and the resulting current response ($i(t)$;

Equation 24) (Bard et al., 2003; Zoski, 2001). Impedance has the same unit of measurement as the electrical resistance (R, Ω).

$$Z = \frac{E(t)}{i(t)} \quad (24)$$

As any other vector quantity (having a magnitude, Z_0, and a phase, Φ), impedance can be expressed as a complex number (Equation 25).

$$Z = Z_0 \cdot (\cos\Phi + j \cdot \sin\Phi) = Z' + j \cdot Z'' \quad (25)$$

Z' is the real part and *Z"* is the imaginary part of the impedance, while *j* is equal to $(-1)^{1/2}$.

Admittance (*Y*) is the reciprocal of the impedance (measured in Siemens, Ω^{-1}; Equation 26) and it can also be expressed as a complex number.

$$Y = \frac{1}{Z} \quad (26)$$

EIS data can be presented in many forms. The most common form is the so-called *Nyquist plot*, in which *–Z"* is plotted against *Z'*. In order to include frequency information, Bode plots are used in which the phase angle (Φ) or the absolute values of impedance (*Z'* or *Z"*) are plotted against ω or log(ω). When EIS data is more convenient to be analysed in terms of admittance (*Y*), *Y'* and Y'/ω are plotted against *–Y"* and $-Y''/\omega$, respectively (Bard et al., 2003; Zoski, 2001; McCafferty, 1997; Macdonald, 1992). Admittance plots in the form of Y'/ω vs $-Y''/\omega$ have the advantage of allowing the direct extraction of capacitance values (see below).

In order to extract key physical or chemical parameters from the acquired impedance data, an equivalent electrical circuit that mimics the electrical response of the investigated electrochemical system has to be chosen. In the case of moderately complex systems (involving simple reversible charge-transfer reactions), simple equivalent circuits can be used to derive the parameters of interest. The chosen circuit should be constructed solely based on the chemical and physical characteristics of the investigated system and should not contain arbitrarily chosen elements.

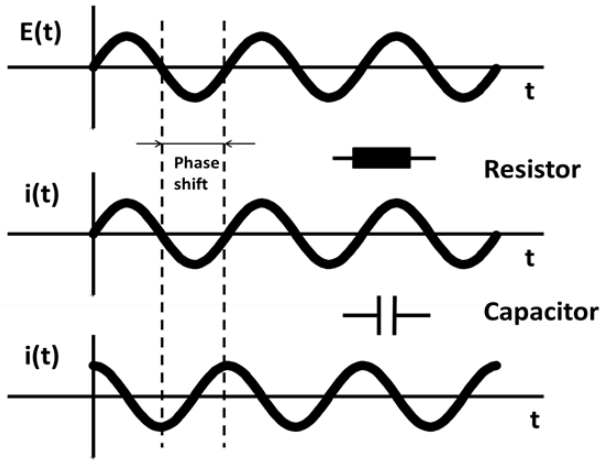

Figure 2.9 Schematic representation of the effect of a resistor (R) and a capacitor (C) on the phase of an alternating current i(t) with respect to the applied voltage E(t).

The equivalent circuit usually contains elements like resistances and capacitances combined in series or in parallel. The impedance of a resistor, for example, is entirely real having no imaginary component and is independent of frequency (Equation 27).

$$Z_R = R \quad (27)$$

The impedance of a capacitor is entirely imaginary and depends on the frequency employed (Equation 28, where C is capacitance, measured in Farrads, F). The current through a capacitor exhibits a phase shift of -90 degrees (Figure 2.9).

$$Z_C = \frac{1}{j \cdot \omega \cdot C} \quad (28)$$

For the modelling of a three-electrode electrochemical cell there are three essential parameters to consider when constructing the equivalent circuit: the electrolyte resistance (R_e), the double layer capacitance (C_d), and the faradaic impedance (Z_f; or the charge transfer impedance). The electrolyte or solution resistance depends on the conductivity of the solution or electrolyte employed and on the geometry of the cell. At the interface between the electrode and the electrolyte, ions from the solution and the counter charges of the electrode form a double layer, which acts as a parallel plate capacitor. The capacitance of the double layer (C_d) is determined by the electrode characteristics (area, roughness, oxide layers, impurity adsorption etc.) and by the electrolyte characteristics (nature of ions, ionic strength, and permittivity). The faradaic impedance has a component called the charge transfer resistance (R_{ct}) which accounts for the kinetics of the electron transfer process and a component called the Warburg impedance (Z_w) which accounts for the mass transport process (Bard et al., 2003; Zoski, 2001; McCafferty, 1997; Macdonald, 1992). The Warburg impedance, also called the mass transfer impedance, can be expressed as a complex number with both the imaginary and the real component depending on the radial frequency ω (Equation 29).

$$Z_w = \sigma \cdot \omega^{-1/2} - j \cdot \sigma \cdot \omega^{-1/2} \quad (29)$$

Equation 29, where σ is the Warburg coefficient (Equation 30) applies only to cases of semi-infinite linear diffusion.

$$\sigma = \frac{R \cdot T}{n^2 \cdot F^2 \cdot A \cdot \sqrt{2}} \cdot \left(\frac{1}{C_{Ox}^{*} \cdot D_{Ox}^{1/2}} \cdot \frac{1}{C_{\mathrm{Red}}^{*} \cdot D_{\mathrm{Red}}^{1/2}} \right) \quad (30)$$

In Equation 30, C^{*}_{Ox} and C^{*}_{Red} are the bulk concentrations of the oxidized and reduced species, respectively.

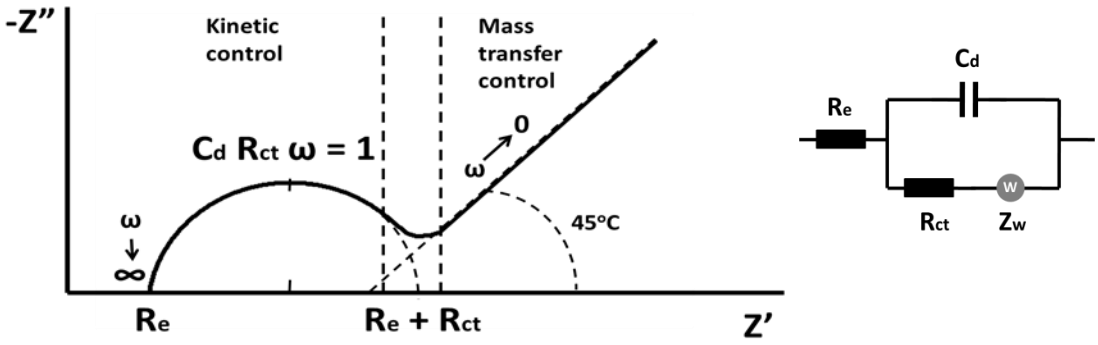

Figure 2.10 Schematic representation of a Nyquist plot for a reversible electrochemical system with diffusion-limited behaviour at low frequencies (left) and the corresponding equivalent Randles circuit (right).

Using the four circuit components based on the four parameters described above (R_e, R_{ct}, Z_w, and C_d), a three electrode electrochemical cell can be modelled using the equivalent circuit depicted in Figure 2.10 (right). The equivalent electrical circuit, called a *Randles circuit*, consists of C_d combined in parallel with R_{ct} and Z_w and in series with R_e. The frequency-dependent impedance response of an electrochemical cell that can be modelled using a Randles circuit is presented schematically in Figure 2.10 in the form of a Nyquist plot. The values of R_e, R_{ct}, and C_d can be extracted graphically and the total

impedance variation can be explained based on the impedance response of the individual circuit components.

The semicircle in the Nyquist plot is caused by the charge-transfer-controlled reaction. At high frequencies ($\omega \rightarrow \infty$), the impedance of the double-layer capacitance (Z_C) has a small value (Equation 28) and the charge transfer resistance is "shorted out". Thus, the intercept of the semicircle with the Z' axis at high frequencies represents the electrolyte resistance (R_e). As the frequency decreases, the impedance of the double-layer capacitance increases and the contribution of the charge transfer resistance to the least resistive current path, and implicitly to the total impedance, increases. The diameter of the semicircle represents the charge transfer resistance (R_{ct}). At the top of the semicircle, where the imaginary part of the impedance reaches its maximum, Equation 31 applies which allows the determination of the time constant of the faradaic process, τ (Equation 32).

$$\omega = \frac{1}{R_{ct} \cdot C_d} \quad (31)$$

$$\tau = R_{ct} \cdot C_d \quad (32)$$

At low frequencies ($\omega \rightarrow 0$), the impedance of the double-layer capacitance is larger than the faradaic impedance (Z_f) and the total impedance is determined by the charge transfer resistance and the electrolyte resistance. Thus the intercept of the semicircle with the Z' axis at low frequency represents the sum of the charge transfer resistance (R_{ct}) and the electrolyte resistance (R_e). The "tail" of the impedance spectrum, which is a straight line

with the slope of 1, is generated by the Warburg impedance which accounts for the purely diffusion-controlled reaction at the lower end of the frequency interval.

When no redox species is present, the impedance response of an electrode can be emulated by a simple circuit used to model any purely capacitive coating: a resistance corresponding to the electrolyte solution (R_e) in series with the double layer capacitance (C_d). The response gives rise to a straight vertical line in a Nyquist plot. The intercept with the *Z'* axis represents the electrolyte resistance (R_e) (Bard et al., 2003; Zoski, 2001). An electrode functionalized with a redox inactive self-assembled monolayer (SAM) exhibits the same impedance response (Figure 2.11)

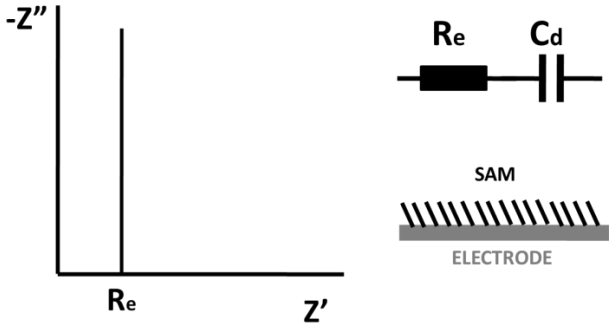

Figure 2.11 Schematic representation of the Nyquist plot (left) obtained for the elementary circuit (top right) used to model the response of a self-assembled monolayer (lower right).

The impedance data in Figure 2.11, plotted as frequency-normalised admittance (Y/ω), appears as a semi-circle, from which the double layer capacitance (C_d) can be determined (Figure 2.12). The diameter of the semi-circle is equivalent to C_d. The response of capacitors is ideal in the mid-frequency range, which spans about four orders of magnitude (e.g. 1-10^4 Hz) (Hitzbleck et al., 2013). At the apex of the semi-circle Equation 31 applies, which allows the calculation of C_d. Experimentally, real systems give rise to depressed semi-circles (with the centre below the x-axis) due to the

occurrence of a distribution of time constants (τ) around the real value (McCafferty, 1997).

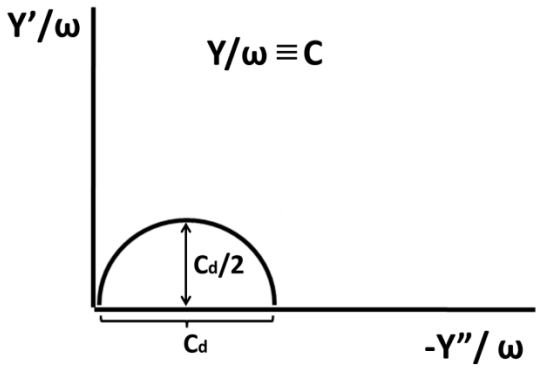

Figure 2.12 Schematic representation of the radial frequency normalised admittance spectrum for the circuit in Figure 2.11. The radial frequency normalised admittance, Y/ω (measured in s/Ω), is equivalent to capacitance, C (measured in F, C/V ≡ s/Ω). The diameter of the semicircle is equivalent to the double layer capacitance (C_d).

The impedance response of tethered artificial lipid membranes (see Section 2.2) can be emulated with a circuit consisting of the electrolyte resistance (R_e) in series with the membrane resistance (R_m) (accounting for residual charge transfer across the boundary), which is in parallel with the membrane capacitance (C_m), and continued, in series, with the double layer capacitance (C_d) (Figure 2.13) (Jadhav et al., 2008; Janshoff and Steinem, 2006; Schiller et al., 2003).

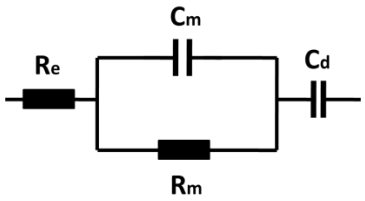

Figure 2.13 Schematic representation of the circuit used to analyse the impedance response of artificial membranes.

The impedance data from the circuit in Figure 2.13, plotted as frequency-normalised admittance (Y/ω), allows the direct determination of the tethered membrane capacitance (C_m) and of the double layer capacitance (C_d) (Figure 2.14).

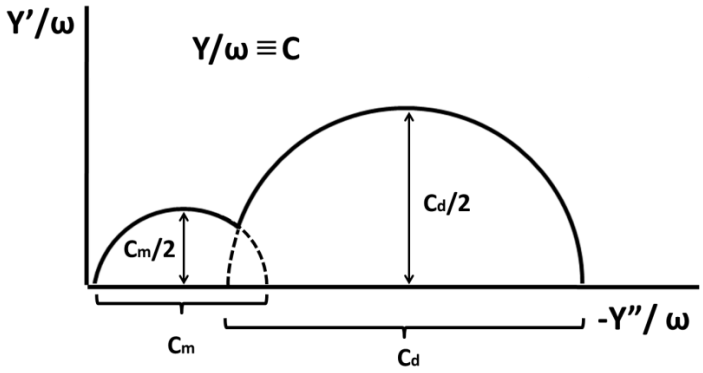

Figure 2.14 Schematic representation of the radial frequency normalised admittance spectrum for the circuit in Figure 2.13.

In order to account for the non-ideal behaviour of systems like tethered membranes incorporating proteins, which can induce defects in the lipid bilayer, complex equivalent circuits have to be constructed. The response of a tethered artificial membrane can be fitted using a circuit that consists of the elements of the circuit in Figure 2.15 plus the resistance (R_{sp}) and the constant-phase element (CPE_{sp}) corresponding to the space layer between the membrane and the electrode surface (Figure 2.15) (Friedrich et al., 2008ab). The constant phase element is used to emulate real electrical double layers, which behave like imperfect capacitors (Macdonald, 1984). The impedance of a CPE is dependent on ω, and two constants, n and Q (Equation 33).

$$Z_{CPE} = \frac{1}{(j \cdot \omega)^n \cdot Q} \quad (33)$$

The phase angle (Φ) of a CPE is independent of frequency and has a value of -90·n degrees. When the empirical constant n equals 1, the CPE resembles a capacitor with Q

having units of capacitance. Despite the many theories advanced so far for explaining the non-ideal behaviour (including surface roughness, non-uniform current distribution, composition and thickness variations), the exact physical phenomena that a CPE emulates are unknown (Jorcin et al., 2006; Bisquert et al., 1998). A CPE is used as a modelling element and has no corresponding real equivalent circuit component.

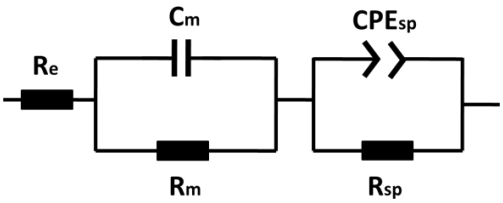

Figure 2.15 Schematic representation of a complex circuit used to analyse the impedance response of systems consisting of tethered artificial membranes taking into account the non-ideal behaviour induced by defects.

The impedance data obtained from a circuit like the one in Figure 2.15, plotted as frequency-normalised admittance (Y/ω), allows the direct determination of the capacitance of the tethered membrane system (Figure 2.16) (Friedrich et al., 2008ab).

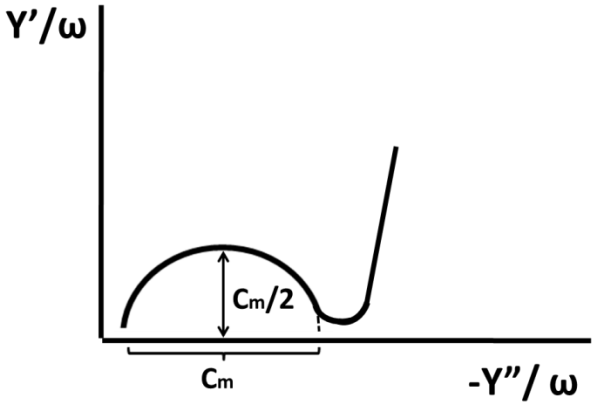

Figure 2.16 Schematic representation of the radial frequency normalised admittance spectrum for the circuit in Figure 2.15. The radial frequency normalised admittance, Y/ω (measured in s/Ω), is equivalent to capacitance, C (measured in F, C/V ≡ s/Ω). The diameter of the semicircle is equivalent to the membrane capacitance (C_m).

2.2 Electrode design for redox membrane enzymes

Electrochemical investigation of the catalytic properties of redox-active membrane enzymes requires the attachment of the enzyme molecules to a conductive support in their integral form. The critical aspects of the immobilisation strategies are enzyme stability, the efficiency and type (direct/mediated) of electron transfer between the enzyme and the electrode, and the control of the catalytic process. Graphite surfaces have been successfully used to immobilise water-soluble proteins and membrane associated proteins that possess a single transmembrane helix (Clarke et al., 2008; Blanford and Armstrong, 2006; Leger et al., 2003). In the case of membrane-bound protein complexes bound to graphite electrodes, it was shown that electron transfer could bypass the membrane-integral subunit (Elliott et al., 2004).

The use of functionalised metal surfaces improves adsorption, but interfacial electron transfer can be slow (Christenson et al., 2008) or can bypass the membrane subunit due to unfavourable protein orientation (Sezer et al., 2011). Typically, thiols adsorbed on gold or silver substrates are used to form self-assembled monolayers (SAMs), which serve as functional surfaces for protein adsorption. In order to improve the stability of membrane enzymes, new approaches have been designed to ensure the immobilisation of protein complexes within lipid membranes resembling the natural lipid environment. Like the thiol SAMs, lipid membranes are formed via self-assembly. The incorporation of the enzyme is achieved by first immobilising the detergent-solubilised protein and then replacing the detergent by lipids via dialysis. Alternatively, protein-containing vesicles can be fused with pre-formed lipid bilayers (Jeuken, 2009; Friedrich et al.,

2008abc). The coverage and thickness as well as the electrical properties of bilayers vary depending on the preparation technique.

2.2.1 Tethered enzymes

Lipid-embedded enzymes can be tethered to the metal surface via the affinity tag (Figure 2.17). The metal ion (Ni^{2+}) in the tag tether was proposed to mediate electron transfer (Friedrich et al., 2008ac), which was shown to be sluggish possibly due to the large distance between the protein metal cofactors and the support (> 50 Å) (Hrabakova et al., 2006). The "sealing" properties of the lipid bilayer are also proposed to hinder electron transfer (Friedrich et al., 2008b). However, by improving the control of the enzyme orientation, via the affinity tag positioning, and using another enzyme as a mediator (e.g. a binding partner like cytochrome *c* for cytochrome *c* oxidase), fast electron exchange is observed (Friedrich et al., 2008ac; Ataka et al., 2006).

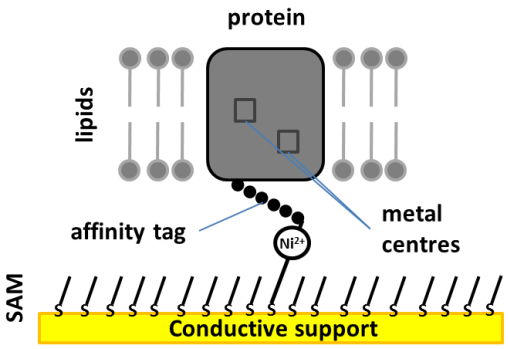

Figure 2.17 Schematic representation of a lipid-reconstituted membrane protein attached to an electrode via its affinity tag (the tag binds to a transition metal complex like Ni^{2+}-nitrilotriacetic acid that is surface-bound via a thiol moiety).

2.2.2 Solid-supported lipid bilayers

Enzyme molecules incorporated in thiopeptide-supported lipid bilayers (Figure 2.18), typically classified as solid-supported lipid bilayers, also require an additional enzyme

to mediate electron transfer to the electrode (Naumann et al., 1999). Cytochrome *c* oxidase, embedded in such a lipid membrane, was found to exchange electrons via cytochrome *c*.

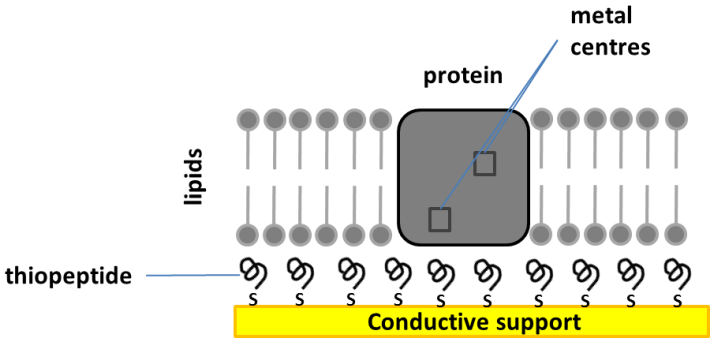

Figure 2.18 Schematic representation of a solid-supported lipid bilayer.

Direct electron transfer was achieved with a strategy involving the covalent attachment of the protein to the electrode and the formation of the lipid bilayer on top of the protein film via lipidic tails that anchor the protein to the membrane (Figure 2.19) (Gutierrez-Sanchez et al., 2011). The recorded H_2 oxidation activity of *Desulfovibrio vulgaris* Hildenborough [NiFeSe] hydrogenase showed that the lipid bilayer enhances protein stability.

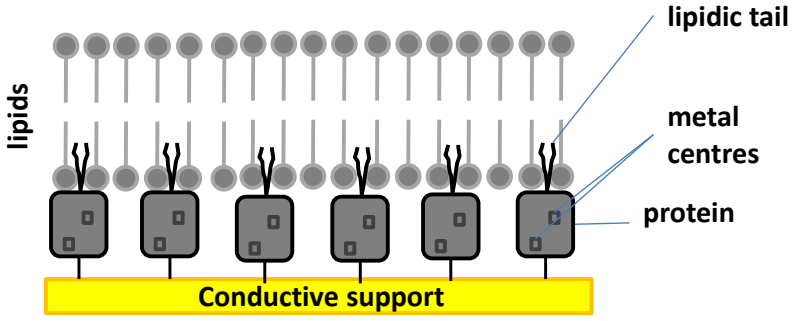

Figure 2.19 Schematic representation of a solid-supported lipid bilayer formed on top of a layer of proteins attached covalently to the electrode.

2.2.3 Hybrid lipid bilayers

The immobilisation of cytochrome *c* oxidase in a hybrid membrane made of a partially formed thiol SAM intertwined with a lipid bilayer (Figure 2.20) has been proposed to allow direct electron transfer between the enzyme and the electrode (Cullison et al., 1994). However, it was found that electron transfer in this kind of setup is slow, limiting enzyme turnover (Su et al., 2004). The cause of slow interfacial electron transfer was attributed to non-optimal protein orientation.

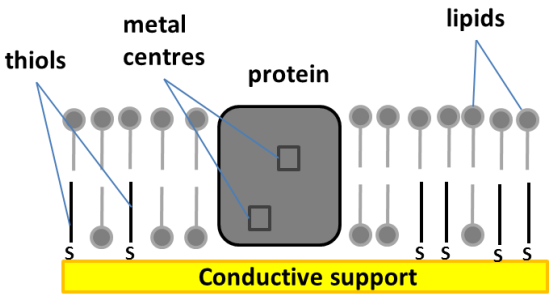

Figure 2.20 Schematic representation of a membrane protein incorporated in a thiol-containing lipid membrane adsorbed on a support.

Hybrid lipid bilayers can also be formed inside a non-conductive microporous structure attached to a conductive support. Such a setup was constructed from an aluminium oxide microporous layer attached to a gold electrode (Marchal et al., 2001). Lipid bilayers were formed on alkane thiol monolayers adsorbed on both the gold and the aluminium oxide surfaces inside the pores. Ubiquinone-8, a lipid soluble natural electron carrier, was used as an electron mediator. The catalytic turnover of the quinone-dependent pyruvate oxidase was efficiently controlled via the redox state of the quinone pool.

2.2.4 Tethered bilayer lipid membranes

The use of thiol-functionalised lipids mixed with short-chain alkane thiols allows the incorporation of transmembrane proteins into tethered bilayer lipid membranes (tBLMs) (Figure 2.21). When these mixed SAMs phase separate on the electrode surface, regions of tethered lipid bilayer are formed that can accommodate transmembrane protein domains (Jeuken et al., 2007a; Jeuken et al., 2006). This approach also enables the immobilisation of native membrane extracts, which eliminates the need for enzyme purification and maintains the natural lipid environment of the protein (Weiss et al., 2009; Jeuken, 2009; Jadhav et al., 2008; Jeuken et al., 2005; Dodd et al., 2003). Direct electron transfer has not been reported so far for redox enzymes in tBLMs. However, by incorporating natural quinones, mediated electron transfer occurs via quinone/quinol redox cycling (see Section 2.2.4.1).

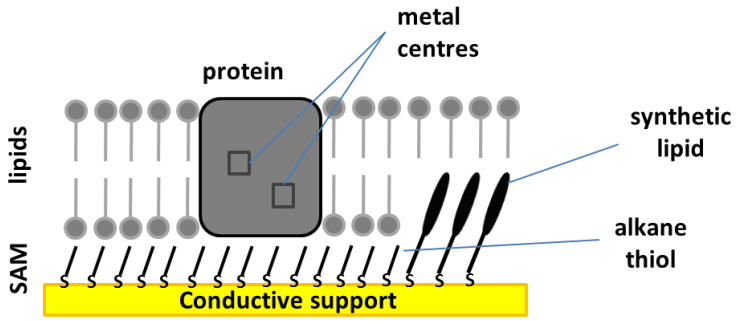

Figure 2.21 Schematic representation of a membrane protein incorporated in a tethered bilayer lipid membrane.

Tin-doped indium (ITO) oxide electrodes have also been used to form lipid bilayers containing thiol-functionalised lipids (Devadoss and Burgess, 2002). The activity of cholesterol oxidase inserted in such a bilayer was only partially characterised via electrochemical detection of hydrogen peroxide reduction with no evaluation of the kinetics of the catalytic process.

2.2.4.1 The tethered bilayer lipid membrane system employed in this thesis

The approach used in this study for immobilizing the protein makes use of tethered bilayer lipid membranes (tBLMs). The configuration used here employs the formation of a mixed SAM onto a gold surface. The mixed SAM is composed of a cholesterol derivative (EO3-cholesteryl), which acts as a tether, and 6-mercaptohexan-1-ol that fulfils the role of a spacer (Figure 2.22). Both the tether and the spacer molecule possess thiol groups that ensure the adsorption onto the gold surface. The cholesteryl moiety of the EO3-cholesteryl, separated from the thiol group by three ethylene-oxy units, is inserted in the lower leaflet of the lipid bilayer (Boden et al., 1997).

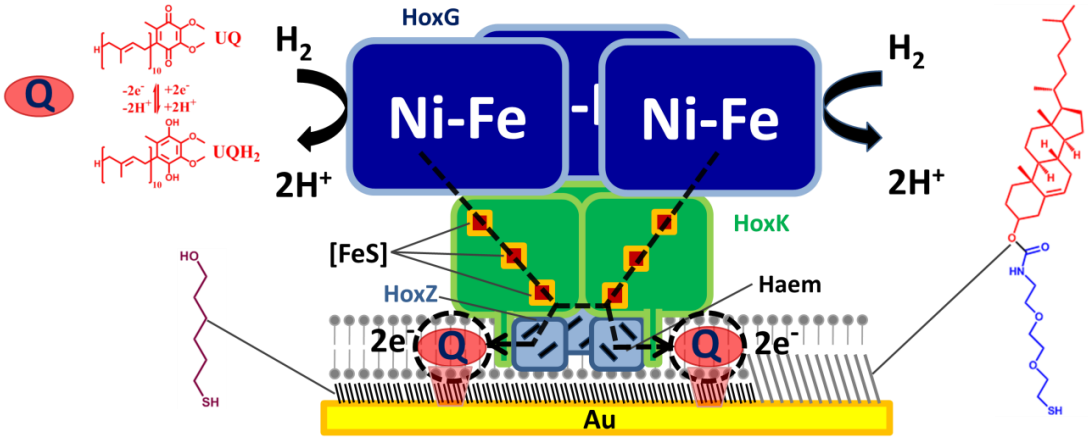

Figure 2.22 Schematic representation of the *R. eutropha* MBH as part of the supercomplex of heterotrimers inserted in the tBLM, which is tethered to a gold electrode via a mixed SAM. The chemical structures of the tether (EO3-cholesteryl) and the spacer (6-mercaptohexanol) in the SAM are depicted in red/blue and dark red. The redox cycling reactions of ubiquinone ($UQ \leftrightarrow UQH_2$) are represented in the top left corner: ubiquinone (UQ) is reduced by the cytochrome *b* (HoxZ subunit) to ubiquinol (UQH_2) which is oxidized at the electrode surface.

The lipid bilayer is formed by adhesion and rupture of phospholipid vesicles in the presence of calcium ions (Ca^{2+}). The lipid vesicles are formed by extrusion. Calcium ions, further added as fusing agents, are thought to screen negative charges and therefore

modify electrostatic interactions (Richter et al., 2006; Jeuken et al., 2005). The *E. coli* lipid extracts used in this study contain approximately 20-35 % cardiolipin and phosphatidylglycerol, which are negatively charged phospholipids at neutral pH (Avanti Polar Lipids, www.avantilipids.com). The positively charged calcium ions are assumed to reduce the electrostatic repulsions between the lipid vesicles favouring the formation of the tethered lipid bilayer membrane (Weiss et al., 2010; Jeuken et al., 2007b).

The incorporation of proteins into the tethered bilayer is achieved by mixing lipid vesicles with cytoplasmic membrane extracts and subjecting them to a series of freeze/thaw cycles followed by extrusion (Dodd et al., 2008). This leads to the formation of mixed vesicles containing the protein having the membrane integral domain inserted into the vesicle wall. Electron transfer is mediated by quinones, such as ubiquinone-8, ubiquinone-10 or menaquinone-7, which are mixed with the lipids used in vesicle preparation. The redox state of the quinone pool is controlled via the electrode potential. In this way, the catalytic activity of the electro-active enzyme, found in equilibrium with the quinone pool, can be driven electrochemically (Figure 2.22). Lipid-soluble quinones, like ubiquinone, are known to have high enough short-range diffusion coefficients ($D = 10^{-6}$ cm^2 s^{-1}) (Di Bernardo et al., 1998; Fato et al., 1986; Lenaz and Fato, 1986) in a phospholipid lipid bilayer (~ 5 nm thickness) (Jeuken et al., 2006) to drive the activity of mitochondrial redox complexes, which can maintain turnover frequencies exceeding 1000 s^{-1} (Fato et al., 1986; Lenaz and Fato, 1986). The use of high overpotentials ensures the poising of the quinone pool in the fully oxidized or reduced state during enzyme turnover (Jeuken et al., 2008). Quinones are typically added in excess of the physiological two-dimensional concentration of 2-3 pmol cm^{-2}

(Marchal et al., 2001; Hackenbrock et al., 1986; Wallace and Young, 1977) to ensure that enzyme turnover is not limited by quinone conversion.

3. Materials and methods

3.1 Chemicals

All electrochemical experiments and membrane preparations were carried out using the following buffer solution: 20 mM MOPS (3-morpholinopropane-1-sulfonic acid) (Sigma-Aldrich), 30 mM Na_2SO_4 (Sigma-Aldrich), pH 7.4. For the pH dependency experiments the following mixed buffer solution was used: MOPS, MES (2-(*N*-morpholino)ethanesulfonic acid) (Sigma-Aldrich), TAPS (3-[[1,3-dihydroxy-2-(hydroxymethyl)propan-2-yl]amino]propane-1-sulfonic acid) (Sigma-Aldrich), CHES (2-(Cyclohexylamino)ethanesulfonic acid) (Sigma-Aldrich), sodium citrate (Sigma-Aldrich) at 20 mM concentration, and 30 mM Na_2SO_4, pH 5-9. The pH was adjusted to the desired value with concentrated NaOH and H_2SO_4 solutions. All aqueous solutions were prepared using purified water (Millipore, 18.2 MΩ cm). All organic solvents were HPLC grade and were used without further purification. EO3-cholesteryl was made as previously described by Boden et al., 1997 (provided by the group of R. J. Bushby, University of Leeds). 6-Mercapto-1-hexanol (Sigma-Aldrich) was used without further purification. Ubiquinone-10 (Sigma-Aldrich) (Figure 3.1) and menaquinone-7 (Wako Chemicals) (Figure 3.1) were used as solutions in chloroform (1 mg/mL) and stored at -20 ^{o}C. *E. coli* polar lipid extracts (Avanti Polar Lipids) were stored in 5 mg dry aliquots under nitrogen at -20 ^{o}C. CCCP (Carbonyl cyanide *m*-chlorophenyl hydrazine) (Sigma-Aldrich) was stored as a 1 mg/mL stock solution in methanol.

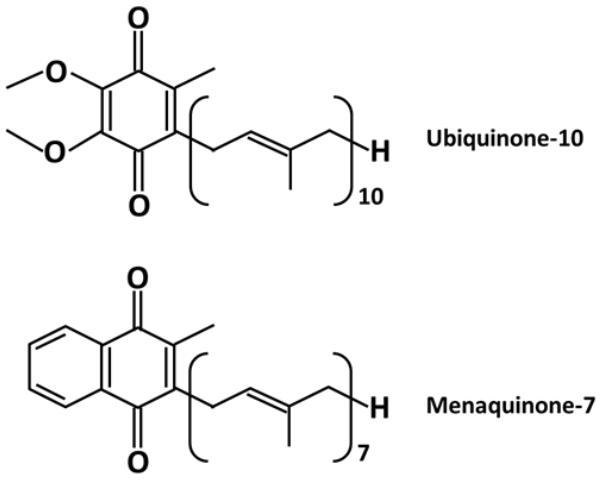

Figure 3.1 The chemical structures of ubiquinone-10 and menaquinone-7.

3.2 Preparation of cytoplasmic membrane extracts of *R. eutropha*

Cytoplasmic membranes were prepared from total membranes of *R. eutropha* HF632 (MBH^{wt} expression strain), HF690 (Δ*hoxK* control strain lacking the MBH small subunit), and HP29 ($MBH^{C19G/C120G}$ expression strain) by sucrose gradient centrifugation. The total membrane samples were provided by Dr. Stefan Frielingsdorf and Prof. Dr. Oliver Lenz at the Technische Universität Berlin (Germany). The fresh total membranes were tested for H_2 oxidation activity using the spectrophotometric assay (see below) before and after being sent to the University of Leeds (Schink and Probst, 1980). To separate the cytoplasmic membranes from outer membranes, total membrane pellets were resuspended in 25% (w/w) sucrose in MOPS/Na_2SO_4 buffer and loaded as the top layer of a 30% (w/w) to 55% (w/w) sucrose gradient. The sucrose layers were then centrifuged at 38000 rpm (Ti45 rotor, Beckman) for 16 hours with minimum acceleration and no breaking. The two bands were found next to each other with no clear separation. Consequently, the lower outer membrane fraction (light brown)

contains cytoplasmic membrane particles (dark brown). The cytoplasmic membrane fraction was washed by centrifuging two times in MOPS/Na_2SO_4 buffer at 41000 rpm (Ti45 rotor, Beckman) for 1 hour. Protein content was determined by BCA assay and SDS-PAGE (Figures 3.2, 3.3, and 3.4). The H_2 oxidation activity of inner membrane samples was checked via the spectrophotometric assay. The cytoplasmic membranes were resuspended in MOPS/Na_2SO_4 buffer and stored at -80 ^oC.

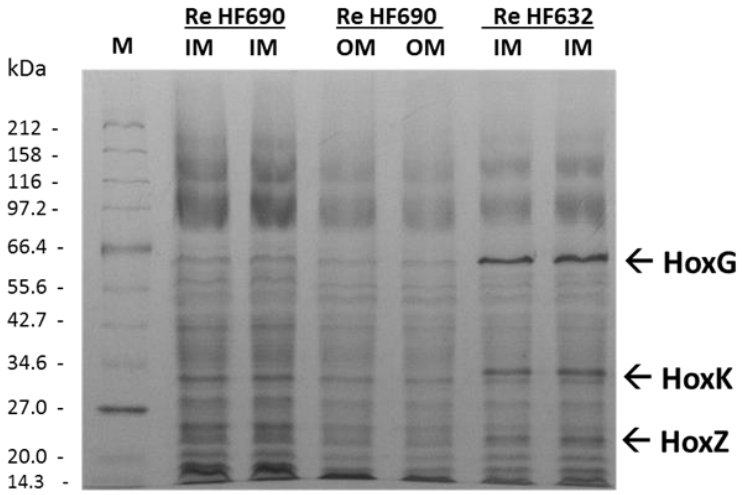

Figure 3.2 Expression level of MBH^{wt} in *R.eutropha* HF632 by comparison to *R.eutropha* HF690 expressing ΔHoxK MBH (12.5 % acrylamide SDS-PAGE; Coomasie staining; 80 µg total protein from the membrane extract; M- marker; IM – inner (cytoplasmic) membrane; OM - outer membrane). The expression level is higher in the HF632 strain compared to the control strain HF690 strain based on the intensity of the bands corresponding to the large subunit (HoxG, 67.2 kDa), the small subunit (HoxK, 34.6 kDa), and the cytochrome b_{562} subunit (HoxZ, 27.6 kDa). The inner membrane fraction was separated from the outer membrane fraction by sucrose gradient centrifugation as explained in the text.

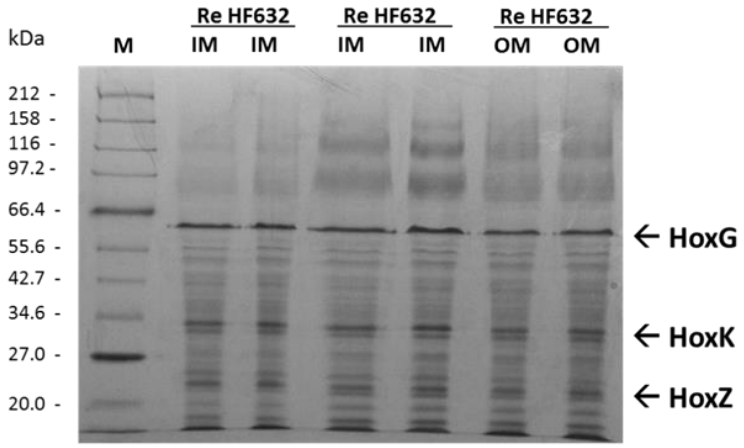

Figure 3.3 Expression level of MBH^{wt} in the inner membrane fraction by comparison to the outer membrane fraction of *R.eutropha* HF632 (12.5 % acrylamide SDS-PAGE; Coomasie staining; 80 μg total protein from the membrane extract; M- marker; IM – inner (cytoplasmic) membrane; OM - outer membrane). The inner membrane fraction was separated from the outer membrane fraction by sucrose gradient centrifugation as explained in the text. The outer membrane fraction contains inner membranes due to the poor separation of the bands on the sucrose gradient.

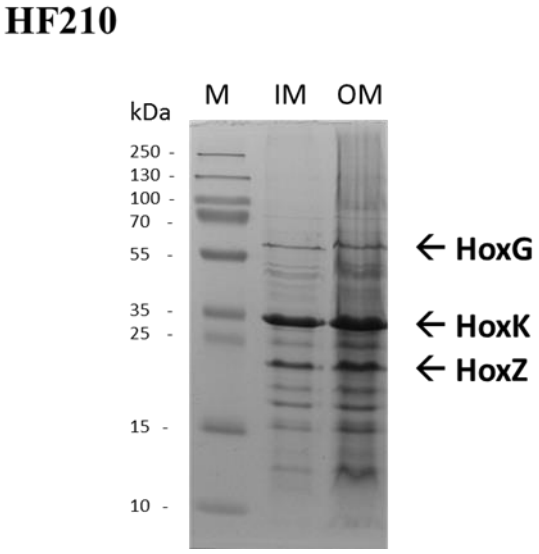

Figure 3.4 Expression level of MBH$^{C19G/C120G}$ in *R.eutropha* HF210 (12.5 % acrylamide SDS-PAGE; Coomasie staining; 140 μg total protein from the membrane extract;M- marker; IM – inner membrane; OM - outer membrane).

3.3 Spectrophotometric activity assay

A 1 mL septum-capped cuvette containing 100 μM methylene blue buffered solution was saturated with H_2 (MOPS/Na_2SO_4 buffer, pH 7.4). Immediately after stopping H_2 purging, a sample of cytoplasmic membranes containing 45-50 μg of total protein was injected into the cuvette. Methylene blue reduction was assessed by monitoring the drop in absorbance at 570 nm (ε = 13.1 cm^2/mol) using a SHIMADZU UV-2450 UV-VIS spectrophotometer. Activity was calculated as μmol H_2/minute·mg of enzyme. All the samples were prepared on the bench. The inner (cytoplasmic) membrane samples retained at least 50% of activity (15 μmol H_2/minute·mg) compared to the total membranes samples (29 μmol H_2/minute·mg, measured after isolation from disrupted cells).

3.4 Electrode preparation and SAM formation

Template stripped gold (TSG) surfaces were prepared as follows. Polished silicon wafers (Rockwood Riddings Wafer Reclaim) were cleaned by sonication in purified water (three times for 5 minutes) and dichloromethane (three times for 5 minutes) and dried under nitrogen. A layer of 150 nm gold (Goodfellows) was deposited by evaporation on the silicon wafers using an Edwards Auto 306 evaporator at < 2 x 10^{-6} mbar. Glass slides were then glued to the gold surfaces using EPO-TEK 377 (Epoxy Technology) which was cured for 2 hours at 120 ^oC. The glass slides were detached from the silicon wafers to expose the TSG surfaces whenever needed. Self-assembled monolayers (SAMs) were prepared by immersing TSGs in 1 mM thiol solutions in 2-propanol (Fischer) for 18 hours at room temperature. The thiol solutions contained EO3-

cholesteryl and 6-mercapto-1-hexanol in ratios ranging from 9%/91% to 12%/88% (mol%). The TSGs were then washed with 2-propanol several times and dried under a flow of nitrogen. The thiol surface coverage was estimated via electrochemical impedance spectroscopy (EIS), assuming that the capacitance of a mixed SAM is a linear combination of the surface area fractions with the capacitances of pure thiol SAMs ($C_{SAM} = \chi_{EO3\text{-}cholesteryl} \cdot C_{EO3\text{-}cholesteryl} + \chi_{6\text{-}mercaptohexanol} \cdot C_{6\text{-}mercaptohexanol}$, where "C" is capacitance and "χ" is the surface fraction; $C_{EO3\text{-}cholesteryl} = 0.78\ \mu F/cm^2$ and $C_{6\text{-}mercaptohexanol} = 4.3\ \mu F/cm^2$) (Jeuken et al., 2006).

3.5 Formation of tethered bilayer lipid membranes (tBLMs)

Ubiquinone or menaquinone were mixed with *E. coli* polar lipids dissolved in chloroform (ubiquinone in dry lipids - 1% w/w; menaquinone in dry lipids - 2% w/w). The *E. coli* phospholipid polar extract contains 67% phosphatidylethanolamine, 23.2% phosphatidylglycerol, and 9.8% cardiolipin. The chloroform solution containing *E. coli* polar lipids and quinone was kept for 15 minutes under nitrogen to evaporate chloroform. In order to ensure the complete removal of chloroform the dry *E. coli* lipids-quinone mixture was kept under vacuum for two hours. The dry mixture was then resuspended in MOPS/Na_2SO_4 buffer (pH 7.4) and extruded through a 200 nm track-etched membrane using a mini-extruder (Avanti Polar Lipids). The obtained vesicles were mixed with cytoplasmic membrane extracts from *R. eutropha* to obtain a ratio of dry lipids (*E. coli* polar lipids) to dry total protein (from the cytoplasmic membrane extract) of 1:10, 3:10 or 4:10 (w/w). The obtained mixture was subjected to three freeze-thaw cycles and extruded through a 400 nm track-etched membrane to obtain mixed vesicles. TBLMs were formed by adding mixed vesicles, at a final lipid

concentration of 0.45 mg/mL, to the TSG/SAM (with a surface coverage of EO3-cholesteryl between 30-50%) in the presence of 10 mM $CaCl_2$ in MOPS/Na_2SO_4 buffer (pH 7.4). The formation of the bilayer was verified by monitoring the drop of the double layer capacitance using electrochemical impedance spectroscopy (EIS) measurements. The impedance data was recorded at the open circuit potential (i.e. 0.2 V). After the formation of the tBLM (1h), the surface was rinsed with MOPS buffer (20 mM MOPS, 30 mM Na_2SO_4, pH 7.4) to remove remaining vesicles, with 1mM EDTA-MOPS buffer to remove Ca^{2+} ions, and again with MOPS buffer to remove EDTA. The integrity of the bilayer-SAM system was checked after washing and throughout the experiment via EIS (0.2 V). The EIS data, along with CV data, confirmed that the tBLM was stable in the potential range of -0.4 V to +0.6 V at high temperature (up to 50 °C) under nitrogen, hydrogen and/or oxygen conditions. Based on the area of the voltammetric redox signals, ubiquinone coverage was found to lie between 6-8 pmol/cm^2. It was previously noted that the commercially obtained *E. coli* polar lipids extracts contain small amounts of ubiquinone-8 (footnote 56 in Jeuken et al., 2006). Accordingly, the mixed vesicle preparation with 2% (w/w) menaquinone-7 (without added ubiquinone-10) also contains ubiquinone-8 (1-1.4 pmol/cm^2). It is possible that part of the ubiquinone-8 originates from the cytoplasmic membrane extracts of *R. eutropha*, which are also likely to contain ubiquinone-8, although this was not confirmed independently.

3.6 Electrochemistry

Electrochemical measurements were carried out in a thermostatically controlled three electrode electrochemical cell (Soham Scientific), which holds 2 mL of buffer solution.

The water bath used for temperature control (Optima, Grant Scientific) was connected to the water jacket of the glass cell through soft tubing. A silver-silver chloride (Radiometer Analytical) or a mercury-mercury sulphate (Radiometer Analytical) electrode were used as reference electrodes. A platinum wire was used as a counter electrode. The gold working electrode was secured at the open base of the cell with rubber o-rings and a PTFE [poly(tetrafluoroethylene)] electrode holder. A 5 mm × 10 mm cross-shape magnetic stirrer bar added to the cell allowed stirring with the use of a magnetic stirrer plate placed underneath the cell (Figure 3.5).

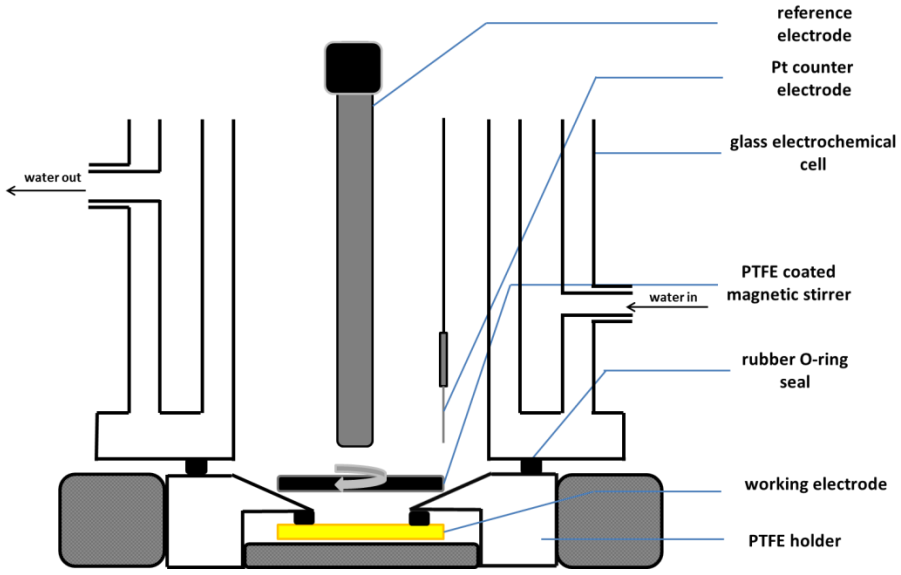

Figure 3.5 Schematic representation of the cross-section of the electrochemical cell with magnetic stirring.

Alternatively, an electrochemical cell with the reference electrode housed in a non-isothermal side-container (Soham Scientific) was used in conjunction with mechanical stirring (using a Caframo stirrer) (Figure 3.6).

All potentials are quoted versus the SHE ($E_{SHE}=E_{Hg/Hg2SO4}$ + 651 mV at 25 ^{o}C; $E_{SHE}=E_{Ag/AgCl}$ + 199 mV at 25 ^{o}C). The reference potential was corrected with respect

to temperature using the data provided in the operating instruction manual (Reference Electrodes, Radiometer Analytical) (Table 3.1).

Table 3.1 The reference potential (mV versus SHE) as a function of temperature (°C).

Temperature (°C)	10	20	25	30	40	50	60
$E_{Ag/AgCl}$ (mV)	214	204	199	194	184	173	163
$E_{Hg/Hg2SO4}$ (mV)	664	655	651	647	639	631	623

Chronoamperometric data obtained with magnetic stirring was smoothed using a moving average procedure (10-25 data points averaging at a sampling rate of 10 data points/second).

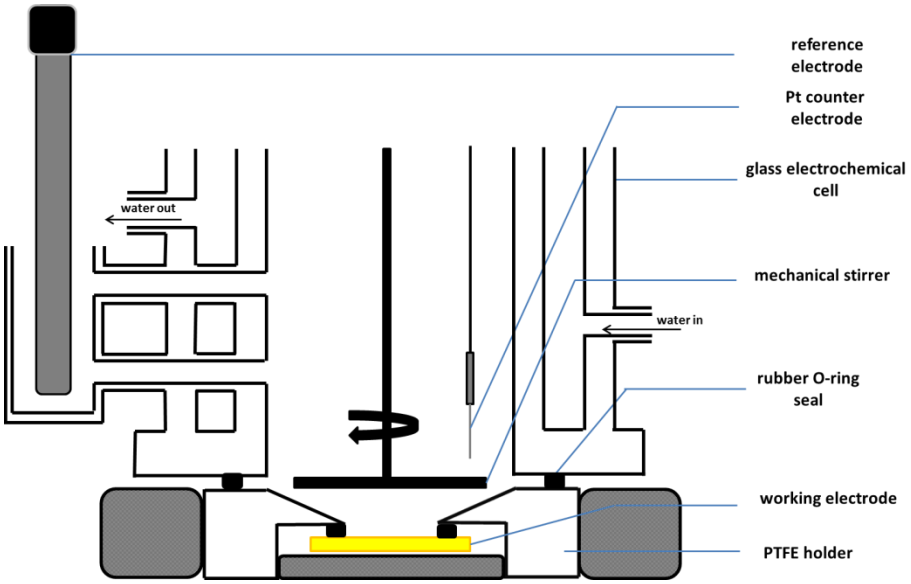

Figure 3.6 Schematic representation of the cross-section of the electrochemical cell with mechanical stirring and the reference electrode housed in a non-isothermal side-container.

Unless stated otherwise, the electrochemical cell was housed in a Faraday cage (for electrical noise minimization) inside a nitrogen-filled glove box (MBraun Lab Master sp) which maintains oxygen levels below 0.1 ppm. Gases were bubbled into the cell solution at constant flow rates using two gas mass flow controllers (Smart-Trak Series

100, Sierra Instruments, accuracy: 1% of full range) connected to 5-μm-rated polyethylene mini filters (Master Pneumatic, FD50-2T) for solid impurity retention. The gases used were hydrogen (BOC), nitrogen (oxygen-free, BOC), medical air (BOC), and a 95% nitrogen - 5% hydrogen mixture (BOC). Gas-saturated aliquots were inserted into the electrochemical cell via an epidural catheter tube (Sarsted). Electrochemical measurements were carried out using an Autolab (Eco-chemie) electrochemical analyzer equipped with a PGSTAT30 potentiostat, SCANGEN module and a FRA2 frequency analyzer.

4. Immobilisation and parameters of activity monitoring of MBH

The formation of lipid bilayers containing MBH was monitored by electrochemical impedance spectroscopy (EIS, see Section 2.1.3 and Section 3.5). EIS has the advantage of probing the adsorbed SAMs and tBLMs without poising the potential at values that would disturb the electrochemical equilibrium. Cyclic voltammetry was employed for probing the dependency of the activity of MBH on pH, temperature, and the composition of the quinone pool in the tBLM. This allowed the determination of the optimum conditions for monitoring the catalytic properties of MBH.

Activity assays based on membrane extracts are prone to interferences from co-expressed enzymes. The probing of control variants is crucial in this case. As mentioned previously, *R. eutropha* expresses four hydrogenases. While the reversible NADH-dependent (SH) and the regulatory hydrogenase (RH) are water-soluble, the actinobacterial hydrogenase (AH) possesses a small subunit C-terminal extension similar to that of the small subunit (HoxK) of MBH, which might favour fixation to the membrane (Schäfer et al., 2016). It was therefore necessary to test whether the cytoplasmic membrane extracts exhibit H_2 oxidation activity in addition to that attributable to the MBH. This was done using cytoplasmic membrane samples from a mutant, HF690, expressing an MBH variant (*ΔHoxK*) which lacks the hydrophilic subunits containing the metal active site and the [FeS] relay.

The $K_M^{H_2}$ was determined in order to provide a measure of the affinity for H_2 of the heterotrimeric MBH in equilibrium with the quinone pool as well as evidence of the correct preservation of the active site structure.

4.1 Immobilisation of MBH

4.1.1 Capacitance and protein content of tBLMs

As emphasized above, the electrochemical properties of the tBLMs employed in the study were assessed using EIS and cyclic voltammetry. The capacitances of lipid bilayers and SAMs can be directly extracted from frequency-normalised admittance plots obtained with EIS. Based on the equivalent electrical circuit models of the SAMs and the tBLMs described in Section 2.1.3, the diameter of the semi-circles in Figure 4.1 and 4.2 is equivalent to the double layer capacitance of the SAMs and the capacitance of tBLMs. As these are the only crucial parameters necessary for verifying the correct formation of the tBLMs, the EIS data sets were not fitted with simulated spectra derived from equivalent circuits to determine other electrical properties. The surface coverages of the SAM thiols were determined based on the value of the capacitance (see Section 3.5).

It was found that SAMs with EO3-cholesteryl coverages between 50% and 80% ensure the formation of tBLMs, incorporating cytoplasmic membranes of *R. eutropha*, with capacitances in the interval 0.7-0.9 $\mu F/cm^2$ (Figure 4.1). According to previous studies, typical artificial tethered bilayer capacitances vary between 0.4 and 0.8 $\mu F/cm^2$ (Schiller at el., 2003; Jadhav et al., 2008), although values one order of magnitude higher have been reported when proteins are incorporated (Friedrich et al., 2008ab).

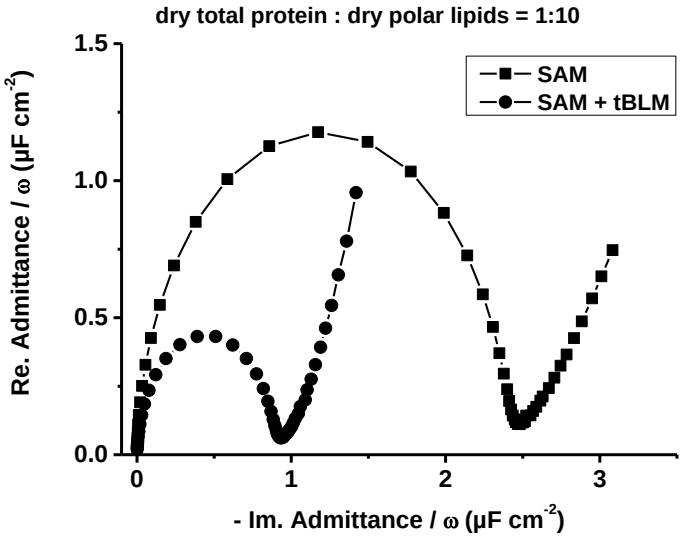

Figure 4.1 Overlay of EIS spectra measured at 0.199 V vs SHE showing the decrease of the double layer capacitance upon formation of a tBLM of *E. coli* polar lipids incorporating inner membranes containing the MBH (the diameter of the half circle is equivalent to the double layer capacitance; 55% EO3-cholesteryl coverage; ratio of dry enzyme to dry polar lipids of 1:10).

In order to improve the level of the recorded catalytic current, the ratio of dry total protein to dry polar lipids in the mixed vesicle preparation was optimised by varying its value between 1/10 and 4/10. H_2 oxidation activity was found to increase with the protein-to-lipid ratio. The increase in enzyme activity upon increasing the ratio from 1/10 to 4/10 was in the range of 3- to 5-fold (compare the current levels at 30 ^{o}C and pH 7.4 in Figure 4.10 with the ones in Figure 4.8 at 30 ^{o}C and pH 7). The increase of the protein-to-lipid ratio had no effect on the capacitance (compare Figure 4.1 and 4.2) or on the stability of the tBLM at high temperature and high electrode potential (see Section 4.2 and Section 4.4). In addition, the activity level was found to increase with tBLM capacitance (approximately 20% increase in activity per 1 μF/cm^2 increase in capacitance in the interval 0.9-1.5 μF/cm^2 and 40-50% in the interval 1.5-2.5 μF/cm^2). EO3-cholesteryl coverages between 30% and 50% were found to lead to tBLM

capacitances of 0.9-2.5 μF/cm^2, which is indicative of incomplete tBLM coverage. These lipid bilayers allowed the probing of enzyme activity for more than six hours, showing the same stability as the tBLMs with capacitance values below 0.9 μF/cm^2. Consequently, most of the experiments described in the following chapters were conducted using tBLMs with capacitances in the interval 0.9-2.5 μF/cm^2.

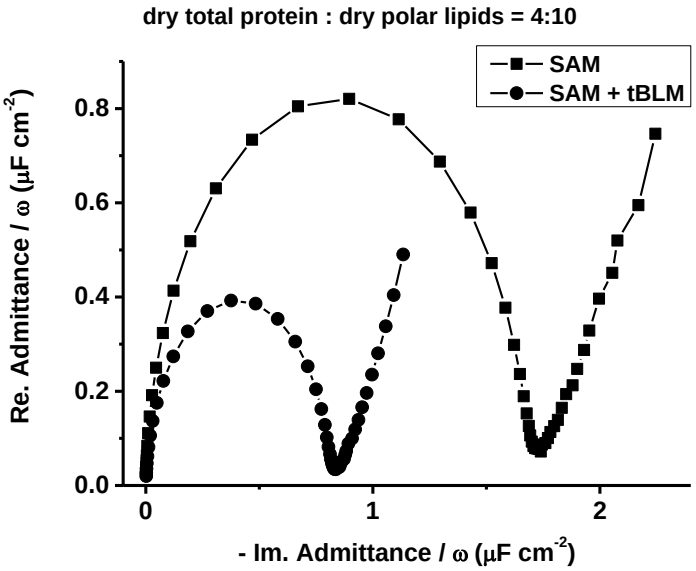

Figure 4.2 Overlay of EIS spectra measured at 0.199 V vs SHE showing the decrease of the double layer capacitance upon formation of a tBLM of *E. coli* polar lipids incorporating inner membranes containing the MBH (the diameter of the half circle is equivalent to the double layer capacitance; 74% EO3-cholesteryl coverage; ratio of dry enzyme to dry polar lipids of 4:10).

The increase in activity with tBLM capacitance may be caused by an enhancement of the H^+ transfer from/to the quinone pool facilitated by a change in the packing density of the lipid bilayer. Quinone redox conversion is gated by protonation/deprotonation steps, which are rate-determining in highly insulating (low-capacitance) lipid bilayers (Gordillo and Schiffrin, 2000). The area of the quinone redox peaks was also found to increase with tBLM capacitance. By lowering the EO3-cholesteryl fraction on the electrode surface, incomplete bilayers are formed, which have higher capacitances (0.9-

2.5 μF/cm^2) and higher permeability to protons. Cholesterol is known to have a rigidifying effect on lipid bilayers, increasing their viscosities (Lenaz and Fato, 1986). Previously it was determined that an EO3-cholesteryl coverage of 30% is optimum for observing quinone peaks (Jeuken et al., 2005). Consequently, lowering of the EO3-cholesteryl fraction on the electrode surface might improve H^+ transfer due to the decrease of the lipid bilayer viscosity.

4.1.2 Activity measurements

Cyclic voltammetry experiments were used to test the integrity of tBLMs and assess the activity of MBH. The stability potential window of the SAM-tBLM system was found to be in the interval of -0.3 to 0.6 V at 10 mV/s. Consequently, in all voltammetric experiments at slow scan rates, the potential was cycled between these values. This impedes the investigation of the H^+ reduction activity of MBH, which is detectable at potentials below -0.3 V at physiologically relevant pH values of 5 to 8.

The scans recorded under 100% N_2 reveal the ubiquinone reduction and ubiquinol oxidation peaks (Figure 4.3, grey line). The large peak separation (~0.4 V) at 10 mV/s is caused by the aforementioned coupling of electron transfer with protonation/deprotonation steps, which are slow in the lipid phase (Gordillo and Schiffrin, 2000). As expected, the redox peak potentials shift with scan rate due to the quasi-reversibility of the quinone/quinol couple (see Section 2.1.1.1). The H^+ gating of the redox conversion of the quinone couple also causes the quinone peaks to shift with pH (see Section 4.2.1), temperature (see Section 4.2.2 and Section 4.4), and the

capacitance of the tBLM, which might influence H^+ transfer from/to the quinone pool (see Section 4.1.1).

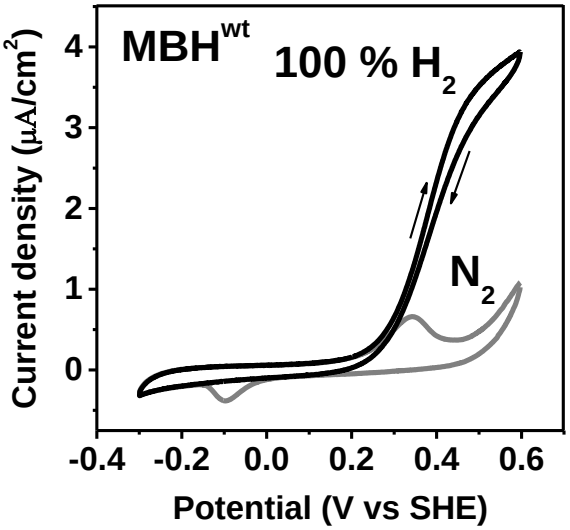

Figure 4.3 Overlay of cyclic voltammograms of MBH^{wt} inserted in the tBLM (10 mV/s; ubiquinone-containing tBLM; 4:10 dry total protein to dry polar lipids; pH 7.4; 30 °C; grey line-100% N_2; black line-100% H_2). The arrows indicate the direction of scan.

The scans recorded under 100% H_2 reveal catalytic wave shapes typical for H_2 oxidation activity (Figure 4.3, black line). No current plateaus in the high potential region of the scans are observed, possibly due to the aforementioned slow H^+-coupled ubiquinol oxidation in the lipid bilayer. However, changing the pH did not significantly alter the shape of the wave (see Section 4.2.1). The same outcome was observed with the addition of the ionophore CCCP (carbonyl cyanide *m*-chlorophenyl hydrazine), which improves the permeability of lipid membranes to protons (Figure 4.4). Scans recorded with menaquinone-loaded tBLMs showed the same residual slope at high potential despite the bigger activity potential window (see Section 4.4). The current slope might be a consequence of the poor coupling to the quinone pool due to tBLM defects in the

proximity of proteins, but the lack of suitable alternative lipid-soluble redox mediators did not allow the testing of such a hypothesis.

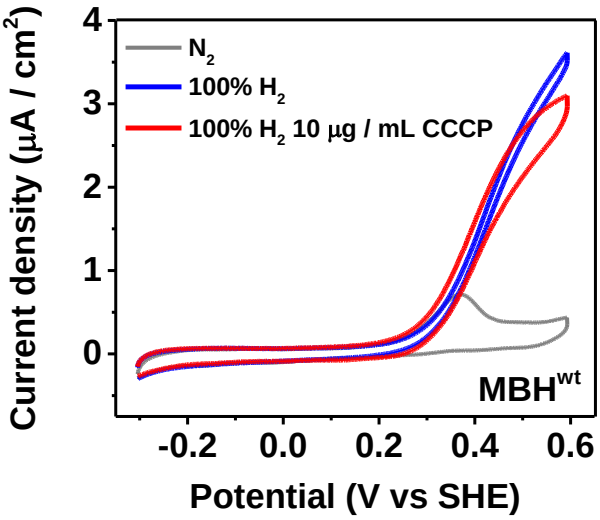

Figure 4.4 Overlay of cyclic voltammograms showing the effect of CCCP (Carbonyl cyanide *m*-chlorophenyl hydrazine) on the shape of the catalytic wave of H_2 oxidation (10 mV/s; ubiquinone-containing tBLM; 4:10 dry total protein to dry polar lipids; 30 ^{o}C; pH 7.4).

The onset of H_2 oxidation coincides with the onset of ubiquinol oxidation at the electrode, confirming the fact that electron transfer between MBH and the electrode takes place via the quinone pool (Figure 4.3, black line). The ubiquinone reduction peak is absent in the scan recorded in the presence of H_2 due to the complete reduction of the ubiquinone pool by MBH. Under 100% H_2, MBH shows no anaerobic inactivation even at scan rates as low as 1 mV/s (Figure 4.5).

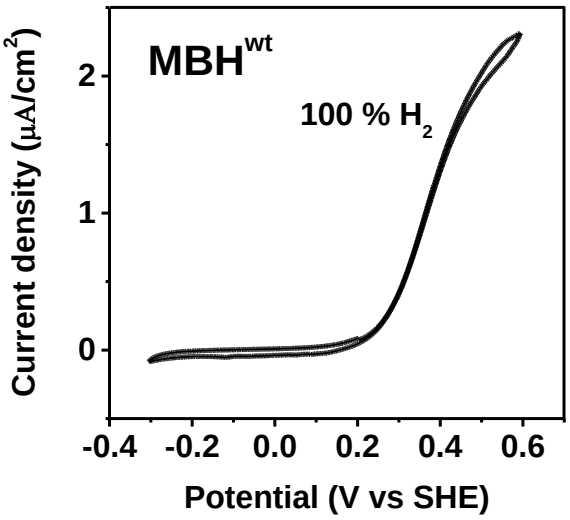

Figure 4.5 Cyclic voltammogram of MBH^{wt} inserted in the tBLM
(1 mV/s; ubiquinone-containing tBLM; 4:10 dry total protein to dry polar lipids pH 7.4; 30 ºC).

4.1.3 Control experiments

Control experiments were carried out by recording voltammograms of the *ΔHoxK* MBH variant (Figure 4.6), which lacks the small (HoxK) and the large (HoxG) subunits.

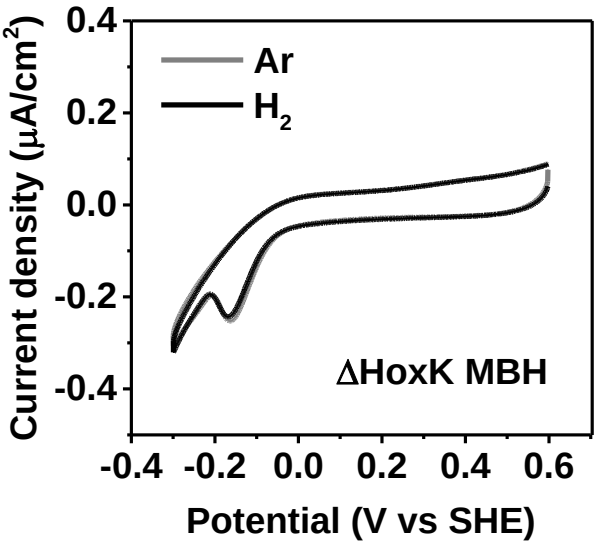

Figure 4.6 Overlay of cyclic voltammograms of *ΔHoxK* MBH
(10 mV/s; ubiquinone-containing tBLM; 1:10 dry total protein to dry polar lipids; pH 7.4; 30 ºC; grey line-100% Ar; black line-100% H_2).

The scans recorded under H_2 show no catalytic oxidation current, which proves that there are no other enzymes with H_2 oxidation activity in the cytoplasmic membranes in addition to MBH (Figure 4.6). Small O_2 reduction currents can be observed at low potential (below -0.2 V) in Figure 4.6 due to the fact that these experiments were carried out on the bench and trace amounts of O_2 reach the electrode surface despite purging of the electrochemical cell with Ar. In these conditions, quinone-converting enzymes present in the cytoplasmic membranes of *R. eutropha* (e.g. ubiquinol oxidases) couple O_2 reduction to ubiquinol oxidation. Due to this, less ubiquinol is oxidized at the electrode leading to the absence of clearly defined ubiquinol oxidation peaks (Figure 4.6).

Additional control experiments were conducted using tBLMs containing *E. coli* polar lipids only. As expected, no H_2 oxidation catalytic current was observed in the scans recorded under 100% H_2 (Figure 4.7). The ubiquinone redox peaks show no change when switching from N_2 to H_2.

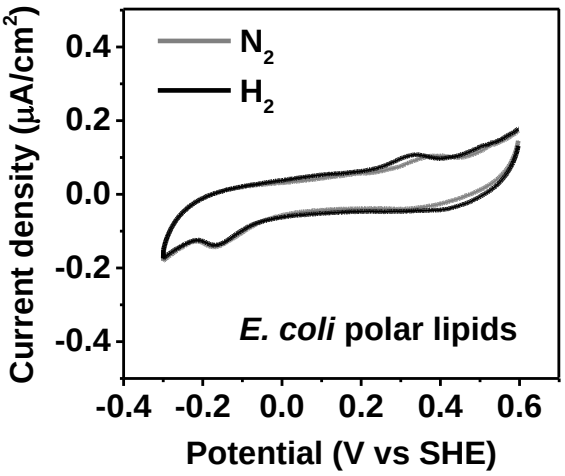

Figure 4.7 Overlay of cyclic voltammograms of a tBLM containing only *E. coli* polar lipids and ubiquinone (10 mV/s; pH 7.4; 30 °C; grey line-100% N_2; black line-100% H_2; ubiquinone-containing tBLM).

4.2 Influence of pH and temperature on the activity of MBH

4.2.1 pH dependence

The pH dependence of the enzymatic activity was tested in the interval 5-9. The onset of H_2 oxidation shifts to lower potentials with increasing pH (Figure 4.8) due to the decrease of the potential of H^+-coupled ubiquinol oxidation (Figure 4.9).

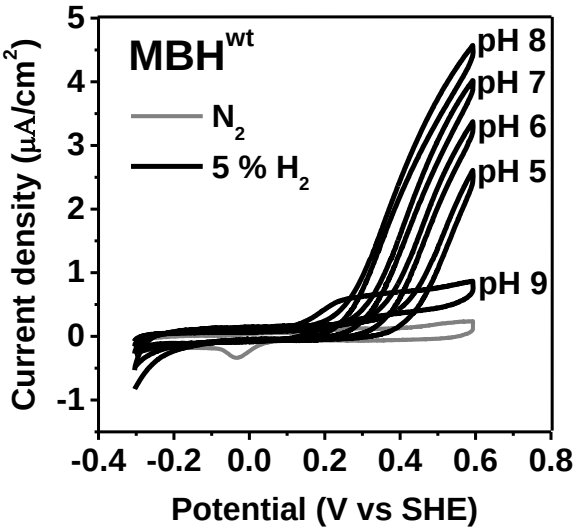

Figure 4.8 Overlay of cyclic voltammograms showing the effect of pH on the H_2 oxidizing activity of MBH^{wt} (10 mV/s; ubiquinone-containing tBLM; 4:10 dry total protein to dry polar lipids; 30 ^oC; grey line-100% N_2; black line-5% H_2; mixed buffer solution: MOPS, MES, TAPS, CHES, sodium citrate at 20 mM concentration, and 30 mM Na_2SO_4).

At pH 9, the enzyme loses activity almost completely. No recovery is observed upon lowering the pH, suggesting that inactivation is caused by irreversible denaturation of the protein complex in the tBLM. Based on the activity potential window, the optimum pH range for monitoring the H_2 oxidation activity of MBH is in the interval of 7-8. In contrast, the optimum pH range of the heterodimeric sub-complex of MBH on pyrolytic graphite electrodes is reported to be in the interval 4.5-6.5 (Ludwig et al., 2009; Goldet

et al., 2008; Vincent et al., 2005ab). Schink and Schlegel (1979) found approximately the same optimum pH ranges for the heterodimeric and the heterotrimeric complex using assays based on artificial redox dyes.

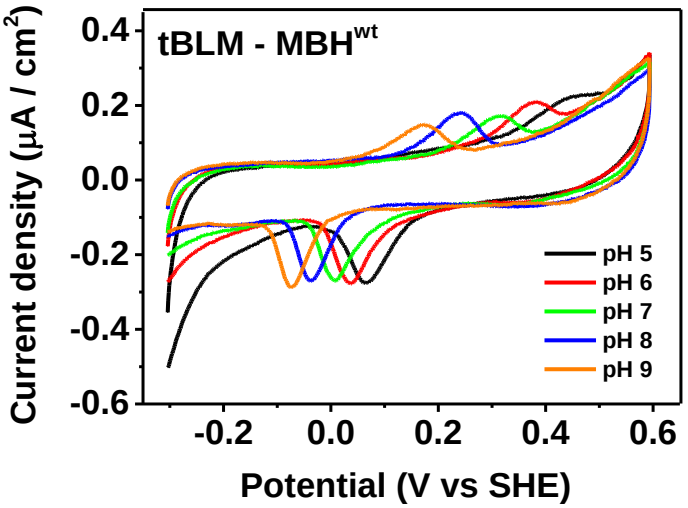

Figure 4.9 Overlay of cyclic voltammograms showing the pH dependence of ubiquinone redox cycling (10 mV/s; ubiquinone-containing tBLM; 4:10 dry total protein to dry polar lipids; 30 ^{o}C; 100% N_2).

4.2.2 Temperature dependence

The temperature dependence of the MBH activity was probed in the interval 20-50 ^{o}C (Figure 4.10). The level of activity increases with temperature. At temperatures of 20 ^{o}C - 30 ^{o}C the SAM-tBLM system is stable for more than six hours. Due to small activity losses (<5%) between scans at temperatures of 40 ^{o}C and 50 ^{o}C, all remaining experiments in the thesis were conducted at 30 ^{o}C.

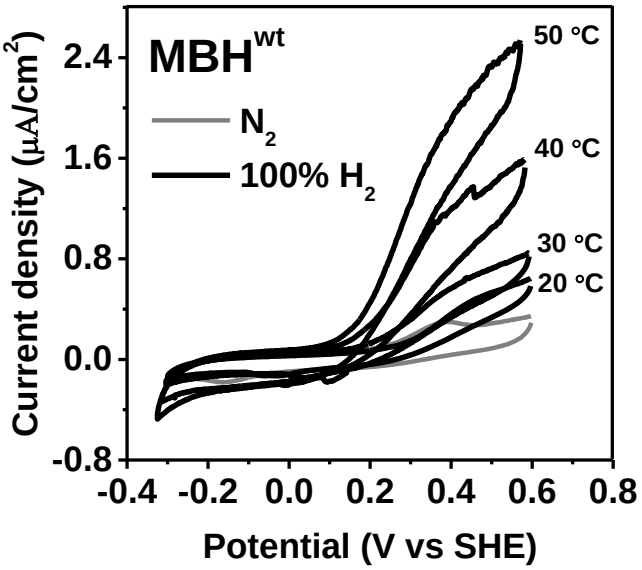

Figure 4.10 Overlay of cyclic voltammograms showing the effect of temperature on the H_2 oxidizing activity of MBH^{wt} (10 mV/s; ubiquinone-containing tBLM; pH 7.4; 1:10 dry total protein to dry polar lipids; grey line-100% N_2; black line-100% H_2).

4.3 Determination of $K_M^{H_2}$

4.3.1 Determination of $K_M^{H_2}$ by transient measurements

Transient measurements make use of the time-dependent evolution of the current response following a short pulse of substrate or inhibitor, while the driving force is kept constant via the electrode potential. The resulting catalytic response, obtained with chronoamperometry, is analysed to determine various kinetic inhibition/activation parameters (Ludwig et al., 2009; Leger et al., 2004).

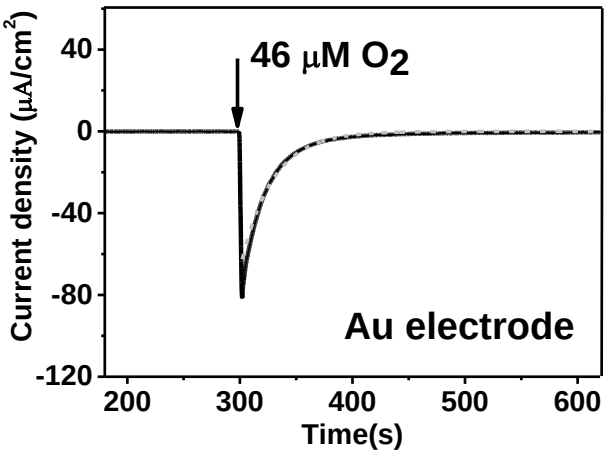

Figure 4.11 Chronoamperogram showing the exponential decay of the O_2 reduction current at a bare Au electrode following a pulse of O_2 (-0.353 V; 30 °C; pH 7.4; N_2 flushing; O_2 concentration after injection: 46 μM). The dashed trace (light gray) is the exponential fit to the current decay ($C(t)=C(0)\cdot\exp(-t/\tau)$; *C* is concentration, and *t* is time).

In the case of hydrogenases, both substrates and inhibitors are gases, which can be removed by flushing with another gas (preferably inert gases like N_2 or Ar). Concomitant stirring of the electrochemical cell solution ensures the exponential removal of the added gas. In order to determine the time constant for exponential gas removal (τ in Equation 5, Section 1.1.3.2.4), O_2 was used as a probe. O_2 reduction at a bare gold electrode was monitored following the injection of an air-saturated aliquot of buffer solution into a N_2-flushed electrochemical cell (Figure 4.11). The value of τ was determined to be 22 s. For the determination of $K_M^{H_2}$, a H_2-saturated aliquot of buffer was injected into the electrochemical cell solution while the electrode potential was held at a value which maintains the quinone pool in the tBLM completely oxidized. Upon substrate injection, the current increases up to a plateau value corresponding to the maximum enzyme turnover under the given H_2 concentration (Figure 4.12).

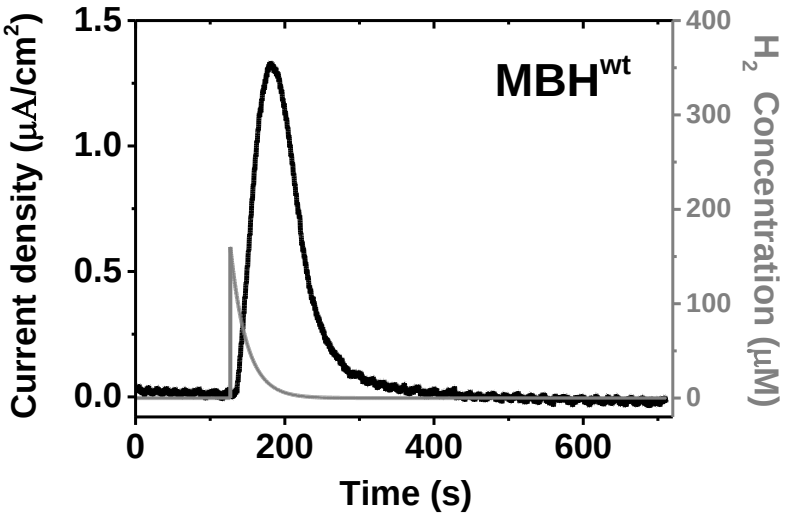

Figure 4.12 Chronoamperogram showing the evolution of the H_2 oxidation activity of MBH^{wt} following a pulse of H_2 (0.497 V; 30 ºC; pH 7.4; ubiquinone-containing tBLM; 4:10 dry total protein to dry polar lipids; time of injection: 126 s; N_2 flushing; H_2 concentration after injection: 160 μM).

It was observed that there is a delay of about 60 s between the point of injection and the point of maximum current. This is caused by the reactivation of the enzyme from the Ni-B state (See Chapter 6). The heterodimeric sub-complexes of O_2 tolerant MBHs display the same delay in PFE-based experiments (Lukey et al., 2010; Ludwig et al., 2009). Due to the aforementioned delay and the fast depletion of H_2, the enzyme reaches maximum activity when the substrate concentration reaches less than 20% of the initial value. Consequently, the observed maximum current plateaus are short lived. After reaching the maximum value, the catalytic current decays as H_2 is flushed out of the electrochemical cell. The flow of H_2 back into the electrochemical cell (through gas permeable components like rubber seals) can sometimes lead to deviations from the ideal exponential towards the end of the current decay. In the region where the H_2 concentration is expected to reach the zero value, the catalytic current is non-zero due to

the presence of H_2 that leaked back into the electrochemical cell. The data points in this region were not fitted (Figure 4.13).

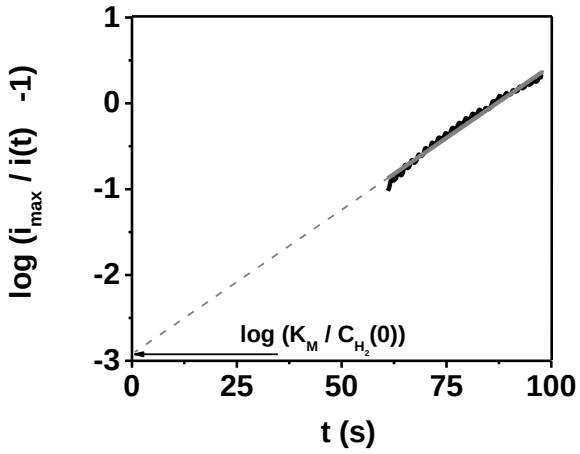

Figure 4.13 Plot for determining the value of $K_M^{H_2}$. The transient decay data in Figure 4.12 was plotted according to equation 32. The continuous grey line represents the fit to the data points (t = 0 s represents the time of injection; the slope is equal to 1 / 2.3 τ; 0.497 V; 30 ºC; pH 7.4; ubiquinone-containing tBLM; 4:10 dry total protein to dry polar lipids; N_2 flushing; H_2 concentration after injection: 160 μM; the dashed gray line representing the extrapolation indicates the intercept with the *y*-axis).

$K_M^{H_2}$ was determined at varying electrode potentials using the linear form of equation 5 (Equation 34) (Figure 4.13).

$$\log\left(\frac{i_{\max}}{i(t)}-1\right)=\log_{10}\left(\frac{K_M}{C_{H_2}(0)}\right)+\frac{t}{2.3\cdot\tau} \quad (34)$$

$K_M^{H_2}$ was found to increase with the applied electrode potential (Table 4.1). This indicates that H_2 oxidation of MBH might be limited to some extent by the redox cycling of the ubiquinone pool and that this rate limitation might have a more pronounced effect at lower potential.

Table 4.1 The value of $K_M^{H_2}$ (± S.E.M.) at different potentials determined via transient measurements (*n* is the number of experiments).

Potential (V vs. SHE)	+0.397	+0.497	+0.597
$K_M^{H_2}$ (μM)	1.5 ± 0.3 (n=3)	2.1 ± 0.9 (n=8)	9.2 ± 2.7 (n=5)

4.3.2 Determination of $K_M^{H_2}$ by titration

In order to validate the $K_M^{H_2}$ values obtained via transient experiments, H_2 titration experiments were carried out. Cyclic voltammograms were recorded at increasing H_2 concentrations in the range 0.1 - 4% (v/v) in N_2, which corresponds to a concentration in solution in the range of 0.8-32 μM (Figure 4.14A). $K_M^{H_2}$ was obtained by fitting Michaelis-Menten curves to data points representing current values from return scans recorded in triplicate.

The values determined at 0.4 and 0.5 V were in good agreement with the ones determined by transient measurements (Table 4.2). The $K_M^{H_2}$ value at 0.6 V is significantly lower than the one determined via transient experiments at the same potential. This disparity between titration and transient measurements at high potential might be related to the duration of oxidative poise, which is significantly longer in the case of transient measurements. It has been determined with the heterodimeric sub-complex that high potentials have a significant effect on the affinity for H_2 of the active site of MBH (Cracknell et al., 2009). In addition, the turnover of the enzyme under low substrate concentration at high potential might be influenced by the reduction of the proximal cluster (see Chapter 6).

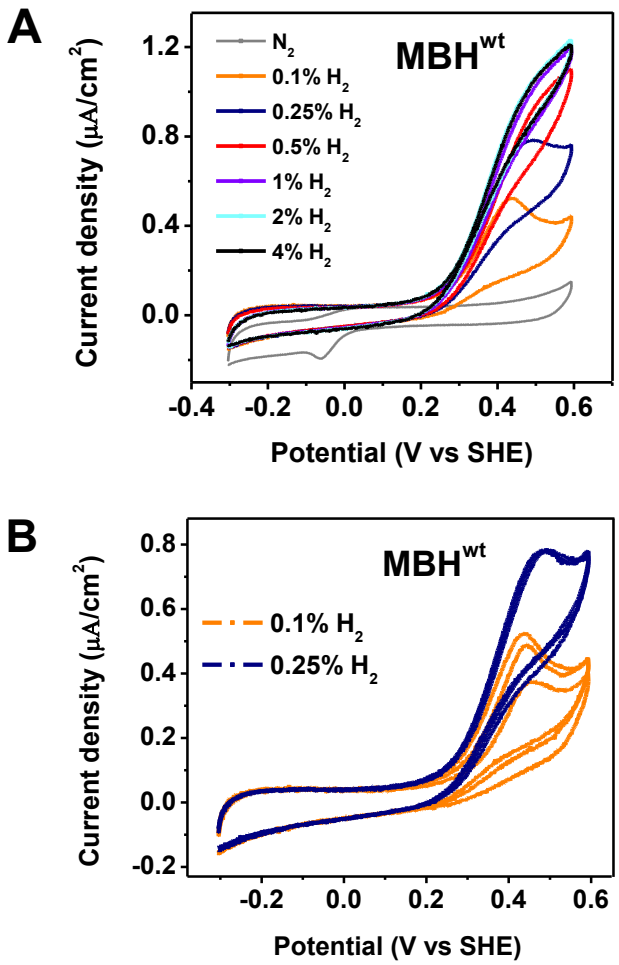

Figure 4.14 (A) Overlay of cyclic voltammograms of MBH^{wt} recorded at varying H_2 concentrations (10 mV/s; ubiquinone-containing tBLM; 4:10 dry total protein to dry polar lipids; pH 7.4; scans were recorded in triplicate). (B) The scans recorded under 0.1% H_2 and 0.25% H_2 in triplicate.

The voltammograms in Figure 4.14A also show that MBH does not undergo significant anaerobic inactivation under low substrate conditions. The decrease in current observed on the forward scans recorded under 0.1% H_2 and 0.25 % H_2 is caused by ubiquinol depletion due to the low turnover of MBH, although some oxidative inactivation cannot be excluded (Figure 4.14B). On the return scans, slight inflections can be observed around 0.4 V, indicative of reactivation. Taking into account the fact that three

consecutive scans were recorded showing the same shape characteristics, it can be assumed that the putative oxidative inactivation is fully reversible.

Table 4.2 The value of $K_M^{H_2}$ at different potentials determined from H_2 titration experiments (the errors in brackets are fitting errors).

Potential (V vs. SHE)	+0.397	+0.497	+0.594
$K_M^{H_2}$ (µM)	2.6 (± 0.5)	2.5 (± 0.6)	1.7 (± 0.4)

4.4 The influence of the quinone pool composition on the activity of MBH

In addition to ubiquinone, menaquinone was also proposed to act as an electron acceptor of MBH (Frielingsdorf et al., 2011). The catalytic activity of MBH in equilibrium with menaquinone was tested as with ubiquinone. Tethered lipid bilayers prepared with menaquinone also contain trace levels of ubiquinone originating from the *E. coli* lipid extract and, possibly, the cytoplasmic membranes of *R. eutropha*. The faint reduction peak centred at approximately -0.05 V (Figure 4.15, grey trace) corresponds to ubiquinone reduction.

Menaquinol oxidation starts at a potential of about -0.1 V, which is approximately 0.3 V lower than the onset potential of ubiquinol oxidation (Figure 4.15, grey trace). It should be noted that the difference between the reduction potentials of the two quinones is only 0.15 V. The additional 0.15 V shift in the oxidation potential is caused by the difference between the deprotonation rates of menaquinol and ubiquinol in the lipid phase of the tBLM. The onset of catalytic H_2 oxidation is observed at approximately -0.1 V, coinciding with the onset of menaquinol oxidation (Figure 4.15, black trace). The local

current enhancement peaking at 0.35 V is due to the oxidation of the ubiquinol produced by MBH from the trace amounts of ubiquinone found in the tBLM.

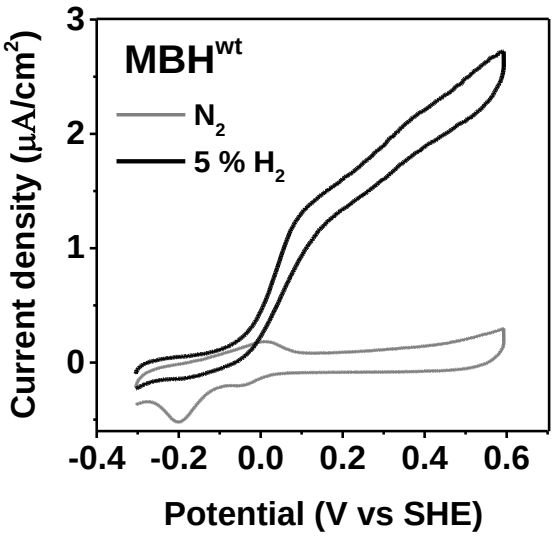

Figure 4.15 Overlay of cyclic voltammograms of MBH^{wt} inserted in a menaquinone-containing tBLM (10 mV/s; pH 7.4; 30 ^{o}C; 4:10 dry total protein to dry polar lipids; grey line-100% N_2; black line-5% H_2).

Enzyme activity was also tested at various temperatures using a tBLM containing menaquinone as well as ubiquinone. Based on the surface coverages derived from the redox peak areas, the ratio of ubiquinone to menaquinone in the lipid bilayers varied between 1.5 and 2.5. Activity levels increase with temperature (Figure 4.16), as observed with ubiquinone (Figure 4.10) and menaquinone (Figure 4.17) as sole electron mediators. At a potential of about 0.25 V, the ubiquinol oxidation current adds to the menaquinol oxidation current, which leads to a change in the shape of the catalytic wave.

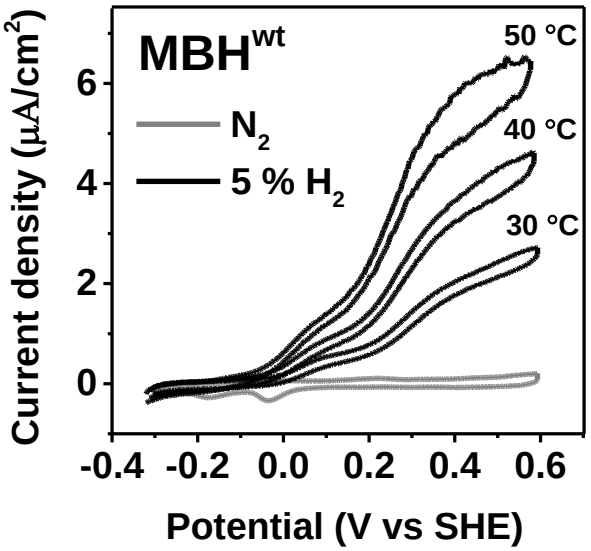

Figure 4.16 Overlay of cyclic voltammograms showing the effect of temperature on the H_2 oxidizing activity of MBH^{wt} inserted into a tBLM containing both menaquinone and ubiquinone (10 mV/s; pH 7.4; 4:10 dry total protein to dry polar lipids; grey line-100% N_2; black line-5% H_2).

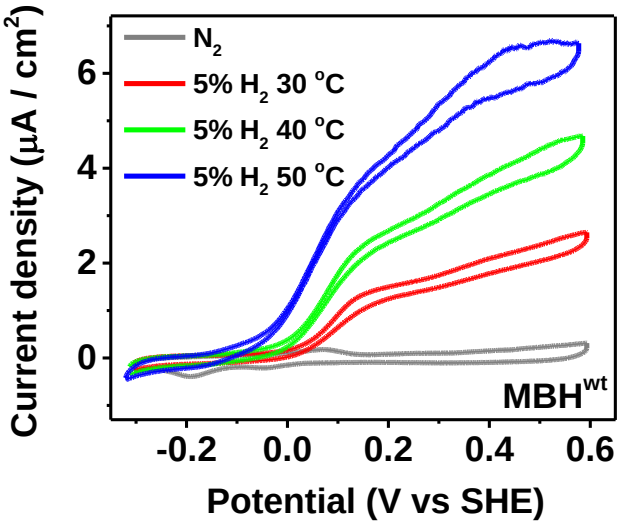

Figure 4.17 Overlay of cyclic voltammograms showing the effect of temperature on the H_2 oxidizing activity of MBH^{wt} inserted into a tBLM containing menaquinone (10 mV/s; pH 7.4; 4:10 dry total protein to dry polar lipids). The onset potential for H_2 oxidation shifts to lower values with temperature due to the decrease of the oxidation potential of menaquinol.

4.5 Conclusions

The catalytic activity of MBH on the electrode increases with tBLM capacitance and the protein-to-lipid ratio. The experiments described in the following chapters were conducted using tBLMs with capacitances in the interval 0.9-2.5 μF/cm^2 and a ratio of dry total protein to dry polar lipids of 4:10.

Cyclic voltammetry experiments revealed that, unlike the heterodimeric sub-complex of MBH, the full heterotrimeric protein complex does not undergo anaerobic inactivation at high potential under 100% H_2, even at scan rates of 1 mV/s. Electron transfer between the enzyme and the electrode was demonstrated to proceed via the quinone pool in the tBLM.

The MBH catalytic wave was found to shift to lower potential with pH. The optimum pH range for monitoring activity in the tBLM setup was determined to lie between 7 and 8. MBH activity significantly increases with temperature, but the stability of the system reduces at temperatures above 40 ^oC. The optimum temperature for monitoring H_2 oxidation activity was found to be 30 ^oC. The experiments described in the following chapters were conducted at 30 ^oC and pH 7.4, as in the case of the control and the preliminary experiments.

The heterotrimeric MBH shows high affinity for H_2, based on the $K_M^{H_2}$ values (1.7-9.2 μM) determined by H_2 titration and transient measurements (0.4-0.6 V). This is in agreement with the H_2 affinity data reported for the heterodimeric sub-complex of MBH (6.1 μM at -0.108 V; 6.0 μM at -0.058 V) (Ludwig et al., 2009; Cracknell et al., 2009). Cyclic voltammetry scans recorded under low H_2 concentrations (<4%) at 10 mV/s

revealed that heterotrimeric MBH does not undergo anaerobic inactivation at high potential like the heterodimeric sub-complex.

Voltammetric data from tBLMs containing a mixed quinone pool revealed that MBH uses both menaquinone and ubiquinone as electron acceptors, alone and in tandem in the lipid bilayer. In addition, no reversible anaerobic inactivation was observed at high potential in any of the scans recorded from menaquinone and/or ubiquinone-containing tBLMs.

5. Inactivation of MBH under oxidizing conditions

5.1 Anaerobic inactivation

The heterodimeric sub-complexes of O_2 tolerant MBH were shown to undergo reversible inactivation at high electrode potential in anaerobic conditions (Pandelia et al., 2010; Lukey et al., 2010; Armstrong et al., 2009; Goldet et al., 2008; Vincent et al., 2005a). Inactivation is observed in cyclic voltammetry experiments as a drop in the catalytic current on the forward scan as the potential is increased, while reductive reactivation leads to a current recovery on the return scan as the potential is lowered (Figure 1.6 in Section 1.1.3.2.2). The inactivation and reactivation kinetics are consistent with the formation of the ready Ni-B state (See Section 1.1.3.2.2). Spectroelectrochemistry experiments have confirmed the accumulation of Ni-B under anaerobic oxidizing conditions (Hidalgo et al., 2015).

The rate of anaerobic inactivation in the case of the heterodimeric sub-complexes of O_2-tolerant MBHs was found to be dependent on substrate concentration (Lukey et al., 2010; Goldet et al., 2008). Cyclic voltammograms recorded under low substrate concentrations revealed a more pronounced drop of the catalytic current at oxidizing potentials. For the heterotrimeric MBH, the voltage was scanned under 0.5% H_2 (equivalent to 4 μM in solution) for 3 cycles in a row at 10 mV/s. No inactivation was observed at potentials up to 0.6 V (Figure 5.1).

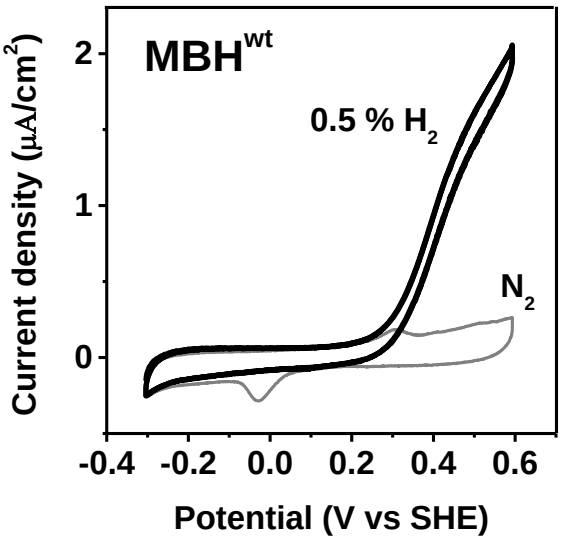

Figure 5.1 Overlay of cyclic voltammograms of MBH^{wt} under N_2 and under 0.5% H_2 (10 mV/s; ubiquinone-containing tBLM; 4:10 dry total protein to dry polar lipids; pH 7.4; 30 ^{o}C; grey line-100% N_2; black line-3 consecutive cycles under 0.5% H_2).

As the accumulation of the Ni-B state in anaerobic conditions is known to be slow (Evans et al., 2013; Lukey et al., 2010; Goldet et al., 2008), the potential was scanned at 1 mV/s to probe slow inactivation kinetics (Figure 5.2). The scans show that the enzyme does not undergo oxidative inactivation under 0.5% H_2. In fact, the level of the current on the return scan in the high potential region of the voltammogram in Figure 5.2 was slightly higher than the one on the forward scan. A crossover can be observed at about 0.3 V. This feature could be due to slow changes in the charge distribution on the SAM surface (due to protonation or reorientation of the thiol molecules), which might lead to changes in quinone electrochemistry in the tBLM, although conclusive evidence has not been obtained.

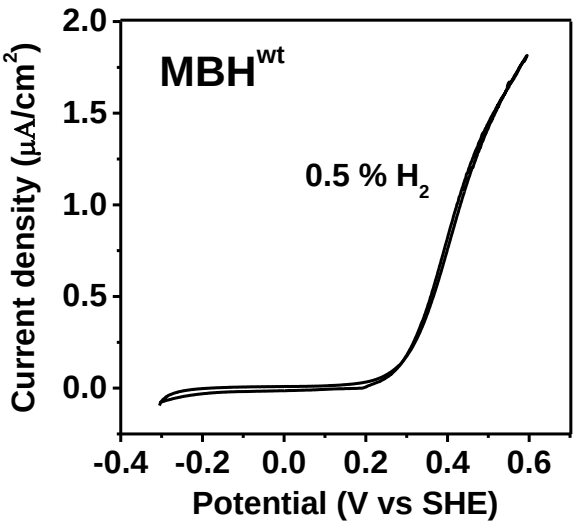

Figure 5.2 Cyclic voltammogram of MBH^{wt} inserted in the tBLM under 0.5% H_2 (1 mV/s; ubiquinone-containing tBLM; 4:10 dry total protein to dry polar lipids; pH 7.4; 30 ^{o}C; the background scan was not recorded in order to minimize possible tBLM damage or protein denaturing).

Scans recorded at 1 mV/s under 0.1% H_2 (0.8 μM in solution, significantly below the average value of $K_M^{H_2}$ of MBH) revealed that in the high potential region the current levels on the return scan are slightly lower than expected based on the value of the capacitive current (Figure 5.3), indicative of inactivation. Scans recorded under 0.5% H_2, following a scan recorded under 0.1% H_2, showed no inactivation (Figure 5.3b).

Compared to the heterodimeric sub-complexes of O_2-tolerant MBHs, the heterotrimeric MBH from *R. eutropha* appears to undergo anaerobic inactivation at much slower rates. The extent of inactivation observed under 0.1% H_2 is much smaller relative to the inactivation observed in PFE experiments, under similar oxidizing conditions, with the heterodimeric sub-complexes of MBHs.

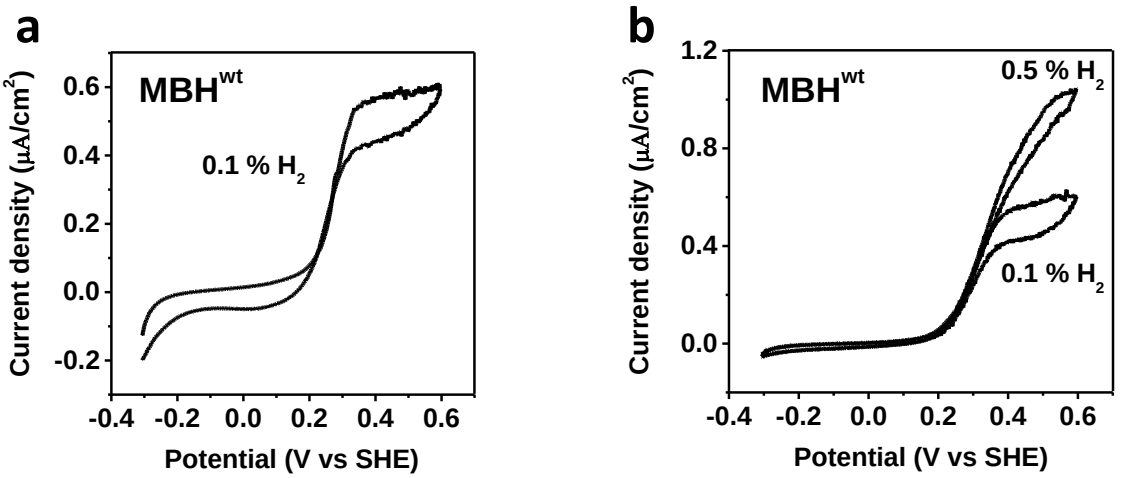

Figure 5.3 Cyclic voltammogram of MBH^{wt} under 0.1% H_2 (a) and 0.1% /0.5% H_2 (b) (1 mV/s; ubiquinone-containing tBLMs; 4:10 dry total protein to dry polar lipids; pH 7.4; 30 ^oC; background scans were not recorded in order to minimize possible tBLM damage or protein denaturing). The 0.5% H_2 scan (b) was recorded after the scan recorded under 0.1% H_2.

5.2 Aerobic inactivation

The heterodimeric sub-complexes of O_2 tolerant MBHs maintain H_2 oxidation activity at ambient O_2 concentration and fully recover activity after exposure to aerobic conditions (Bowman et al., 2014; Evans et al., 2013; Goris et al., 2011; Lukey et al., 2011; Lukey et al., 2010; Pandelia et al., 2010; Ludwig et al., 2009; Vincent et al., 2005a). As in the case of anaerobic inactivation, the reactivation kinetics are consistent with reduction from the Ni-B state. The sub-complex of MBH from *R. eutropha* was reported to maintain about 70% of activity at a potential of -0.008 V under an O_2 concentration equivalent to the ambiental aqueous concentration (Ludwig et al., 2009).

Investigation of the O_2 tolerance of the heterodimeric sub-complexes of MBHs at high electrode potential is complicated by the concomitant occurrence of anaerobic inactivation. The selection of the electrode potential in chronoamperometric experiments probing the O_2 tolerance of the sub-complexes of MBHs has been restricted

by anaerobic inactivation at oxidizing potentials and O_2 reduction at mildly reducing potentials (Lukey et al., 2010; Ludwig et al., 2009; Vincent et al., 2005b). Therefore, the full heterotrimeric MBH, which undergoes anaerobic inactivation to a very small extent (see Section 5.1), can provide an insight into the catalytic behaviour under aerobic conditions at high electrode potential. However, the cytoplasmic membrane extracts employed in this study might contain other membrane-bound enzymes that are coupled to the quinone pool (e.g. ubiquinol oxidases) (Cramm, 2009), which might interfere with the measurement of the tolerance to O_2 of MBH.

5.2.1 Transient experiments

The catalytic properties of MBH under oxidizing conditions after the application of short pulses of O_2 were tested via transient measurements. Aliquots of air-saturated buffer solution were injected into the H_2-flushed electrochemical cell, while the electrode potential was poised at a value that maintains the quinone pool completely oxidized. Upon adding 57 μM O_2 (equivalent to approximately a quarter of the aqueous ambient concentration; Weiss, 1970), the recorded current drops very fast to 75±1.4% (n=12) of the initial level at potentials of 0.4-0.6 V (Figure 5.4).

Current recovery commences long before the complete depletion of O_2 from the cell solution and is completed within 2 minutes after the injection, without requiring reducing potentials. The observed current decrease might be caused by aerobic inactivation of the enzyme (conversion to the Ni-B state) as observed with the heterodimeric sub-complex. The current trace mirrors the O_2 concentration profile, suggesting that the active enzyme might be in equilibrium with the Ni-B state. It is also

possible that the current decrease is caused by quinol oxidases in the cytoplasmic membrane extracts and that the observed current recovery is only a consequence of the exponential decline of the O_2-dependent quinol oxidase activity. An estimation of the contribution of this competing reaction at oxidizing potentials is complicated by the lack of suitable specific irreversible inhibitors of the oxido-reductases coupled to the quinone pool. Reconstitution of the purified heterotrimeric MBH into tBLMs would allow the investigation of the O_2 tolerance without any interference from quinone-coupled membrane enzymes.

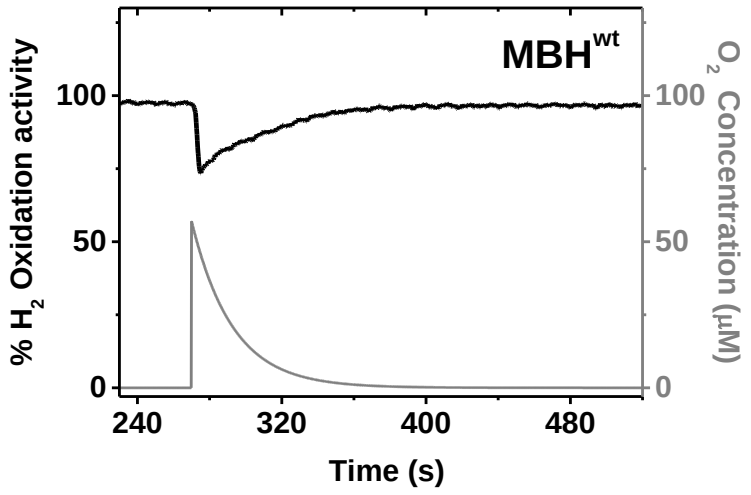

Figure 5.4 Chronoamperogram showing the evolution of the recorded current from a tBLM with MBH^{wt} after a pulse of O_2 (0.397 V; ubiquinone-containing tBLM; 30 ºC; pH 7.4; 4:10 dry total protein to dry polar lipids; 100% H_2 flushing; O_2 concentration after injection: 57 μM; the exponential decay of the O_2 concentration was plotted, as already described in Section 4.3.1, according to the equation: $C(t) = C(0)\cdot\exp(-t/\tau)$, where *C* is concentration, τ=22 s, and *t* is time).

5.2.2 Continuous O_2 flushing experiments

The tolerance of MBH towards O_2 was also assessed through experiments employing continuous purging with gas mixtures containing O_2. Cyclic voltammograms were recorded at 5 mV/s under 2.5% H_2 in N_2 and under 2.5% H_2/10% O_2 in N_2 on the

laboratory bench (i.e. outside the glove box) (Figure 5.5). In the scan recorded under 2.5% H_2 in N_2, due to the presence of trace amounts of O_2 in the electrochemical cell, catalytic currents corresponding to ubiquinol oxidase activity can be observed at potentials below -0.1 V (Figure 5.5, red trace). In the presence of 10% O_2, the catalytic current levels in the high potential region drop approximately 25% compared to the scan recorded under 2.5% H_2 in N_2 (Figure 5.5, blue trace). The currents occurring below -0.1 V are caused by O_2 reduction catalysed by quinol oxidases and to some extent by O_2 reduction directly at the electrode. The lower current levels observed at high potential in the presence of O_2 might be only an effect of quinol oxidases consuming the ubiquinol that should be oxidized at the electrode. Full recovery of activity was confirmed by a scan recorded under 5% H_2 after O_2 treatment (data not shown).

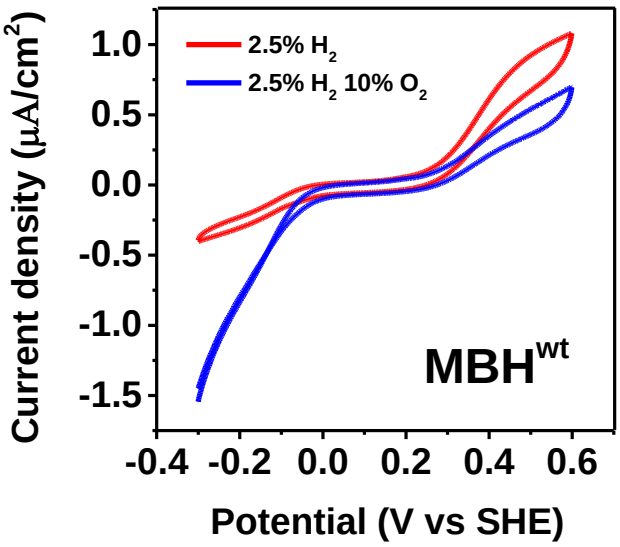

Figure 5.5 Overlay of cyclic voltammograms of MBH^{wt} inserted in the tBLM under 2.5% H_2/2.5% H_2 + 10% O_2 in N_2 (5 mV/s; ubiquinone-containing tBLM; 30 ºC; pH 7.4; 4:10 dry total protein to dry polar lipids; red line: 2.5% H_2 in N_2; blue line: 2.5% H_2 + 10% O_2 in N_2).

To further assess the MBH tolerance towards O_2, chronoamperometric experiments were conducted to probe the enzyme under continuous supply of O_2 as depicted in Figure 5.6. The electrode potential was poised at a value that maintains the quinone pool oxidized and after flushing 5% H_2 for 10 minutes, the gas mixture was changed to 2.5% H_2/10% O_2 for another 10 minutes, after which the gas mixture was switched back to 5% H_2 in N_2 to test the activity recovery. The drop in H_2 concentration from 5% to 2.5% is not expected to affect the activity level as the equivalent aqueous concentrations are well above the $K_M^{H_2}$ value at 0.5 V (5% H_2 is equivalent to 40 µM in solution, 2.5% H_2 is equivalent to 20 µM in solution, while the value of $K_M^{H_2}$ at 0.5 V lies in the range 1.2 – 3.1 µM - see Section 4.3).

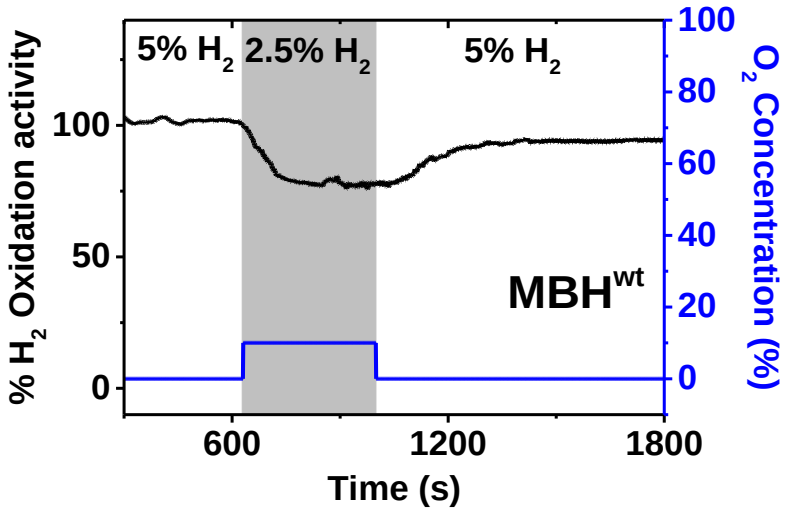

Figure 5.6 Chronoamperogram showing the evolution of the recorded current of MBH^{wt}, embedded in a tBLM, upon switching between anaerobic and aerobic gaseous environments (0.5 V; ubiquinone-containing tBLM; 30 °C; pH 7.4; 4:10 dry total protein to dry polar lipids). The aerobic gas mixture was obtained by mixing medical air (20% O_2/80% N_2) with 5% H_2 in N_2 in a ratio of 1:1.

Under 10% O_2 the current level is 25% lower than the initial level (Figure 5.6). Immediately after switching the gas back to 5% H_2, the current starts to increase and, in

about 5 minutes, recovery amounts to about 94%. Complete recovery was not observed, which might be due to tBLM/SAM damaging during the long duration experiment carried out on the bench and possibly due to protein denaturing (Figure 5.7).

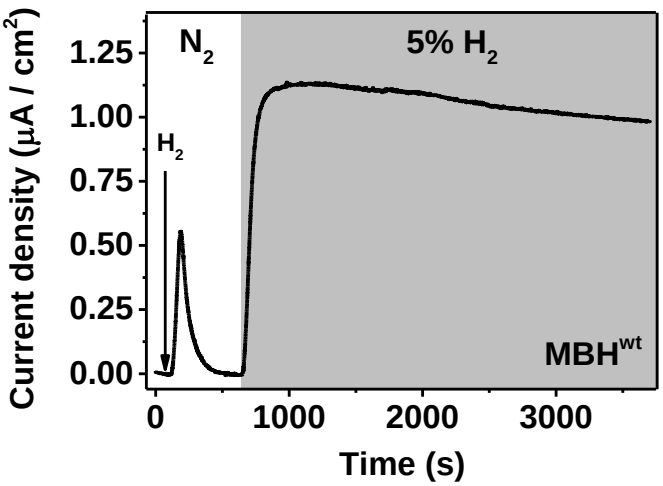

Figure 5.7 Chronoamperogram showing the evolution of the H_2 oxidation activity of MBH^{wt} after the injection of one aliquot of H_2-saturated buffer into the cell solution and under 5% H_2 (0.499 V vs SHE; ubiquinone-containing tBLM; 30 ^oC; pH 7.4; final H_2 concentration after injection: 100 μM). The decrease of the current level under continuous purging with 5% H_2 might be caused by slow SAM-tBLM desorption or MBH denaturing.

The current drop observed under 10% O_2 in these experiments varied from 25 to 50% of the initial level (Figure 5.8). Even when the current drop was 50%, recovery was almost complete after switching to anaerobic conditions. As the ratio of ubiquinol oxidases to MBH is expected to vary with each tBLM preparation, the variable extent of current drop observed in these experiments might be indicative of the influence of ubiquinol oxidases on the oxidation state of the quinone pool in aerobic conditions. Therefore, it is very likely that the apparent activity loss of MBH in the presence of O_2 is mainly due to the ubiquinol oxidation activity of the quinone-coupled oxido-reductases in the tBLM.

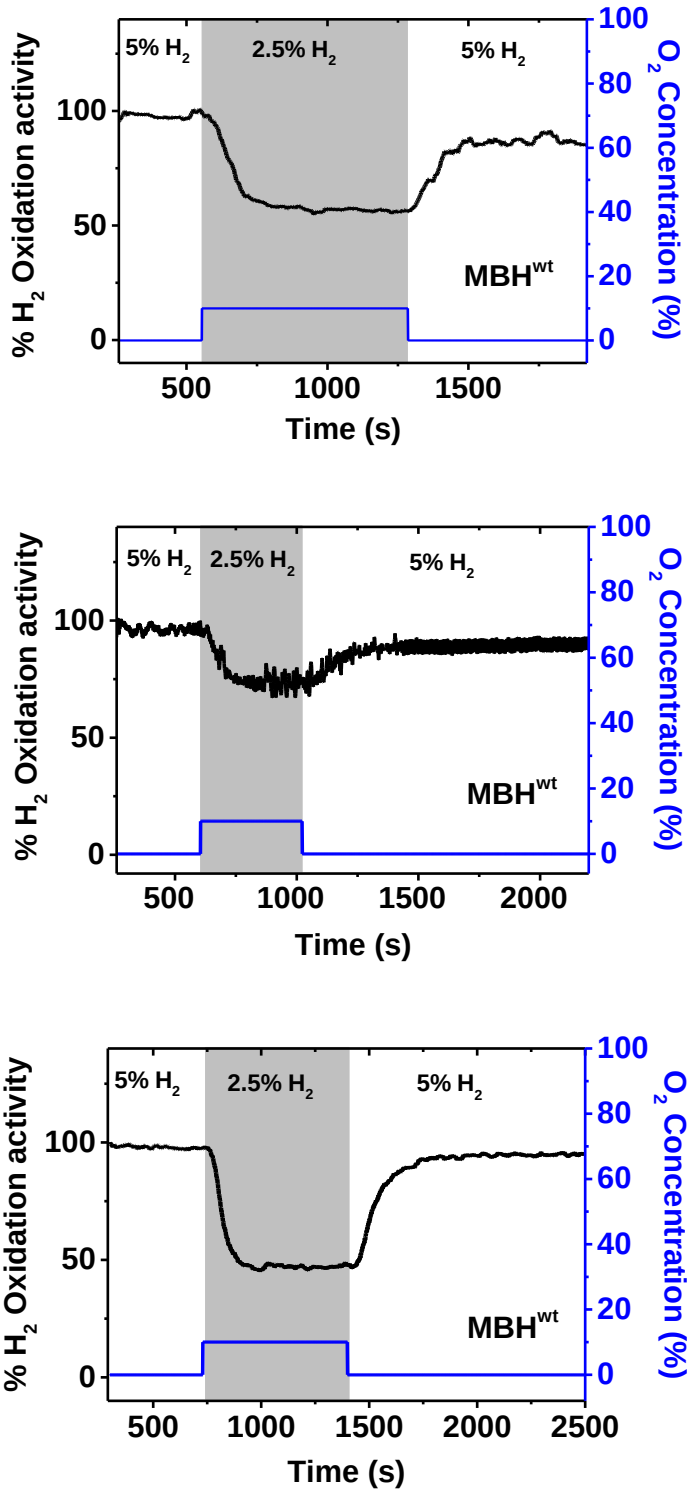

Figure 5.8 Chronoamperograms showing the evolution of the recorded current of different tBLMs with MBH^{wt} upon switching from anaerobic to aerobic and then back to anaerobic conditions (0.5 V; ubiquinone-containing tBLMs; 30 °C; pH 7.4; 4:10 dry total protein to dry polar lipids). The sequence was designed to assess the recovery of activity after prolonged exposure to O_2.

5.3 Conclusions

As a full heterotrimeric protein complex, in equilibrium with the quinone pool, MBH appears to undergo reactivation from the Ni-B state under oxidizing conditions even under substrate limiting conditions. Hence, the accumulation of Ni-B is slow even under 0.1% H_2. It is possible that reverse electron flow from quinol to the active site might ensure the reducing conditions necessary for reactivation from the Ni-B state, but, at high potential, the quinone pool remains in the oxidized state. Thus, it is very unlikely that Ni-B accumulation is prevented by the quinone pool acting as a redox buffer.

Alternatively, the reactivation properties of MBH might be related to its quaternary structure. It should be noted that the oligomerisation of the MBH in the cytoplasmic membrane might enable a reactivation pathway (Volbeda et al., 2013). Intermolecular electron transfer within the supercomplex of heterotrimers, possible through the distal cluster located close the surface of the small subunit, could be advanced as an explanation for the reactivation kinetics of MBH under oxidizing conditions. The fast reactivation of MBH from the Ni-B state at high potential can be promoted by the provision of electrons from a neighbouring active MBH.

The heterotrimeric MBH, in equilibrium with the ubiquinone pool, was also probed in aerobic conditions at high electrode potentials. Assuming the activity of quinol oxidases to be completely absent and the observed current drop to be solely due to aerobic enzyme inactivation, the O_2-tolerance of MBH is still higher than the tolerance reported for the heterodimeric sub-complexes of O_2-tolerant MBHs. MBH recovers completely after O_2 treatment even at potentials as high as 0.5 V under low substrate concentrations

(2.5-5% H_2). Considering the high O_2 reduction activity of quinol oxidases observed under the employed O_2 levels, it can also be hypothesised that the current drop at high potentials is mainly due to enzymatic ubiquinol oxidation. Consequently, the MBH tolerance to O_2 might be much higher than what the experimental results in this chapter suggest. I therefore propose that the oligomeric state of the protein complex in the native cytoplasmic membrane plays a crucial role in maintaining high H_2 oxidation activity under aerobic conditions.

6. The role of the proximal [4Fe-3S] cluster in the reactivation of MBH in electron-deficient conditions

The unusual [4Fe-3S] proximal cluster in O_2 tolerant MBHs ensures the formation of the Ni-B state under oxidizing conditions without any Ni-A accumulation (Evans et al., 2013; Lukey et al., 2011; Goris et al., 2011; Fritsch et al., 2011b; Saggu et al., 2009). This leads to the fast recovery of activity observed under both anaerobic and aerobic conditions. The proximal cluster undergoes two redox transitions to provide electrons for O_2 reduction (See Section 1.1.1). The reduction of the most oxidized state of the cluster, called the "superoxidized state", to the partially reduced state is accompanied by major structural rearrangements (Frielingsdorf et al., 2014). The standard [4Fe-4S] proximal cluster does not access a superoxidized state, undergoing only one redox transition. Comparing hydrogenases carrying a [4Fe-3S] proximal cluster and hydrogenases carrying a standard [4Fe-4S] proximal cluster in terms of reactivation kinetics would reveal the role played by the second electron provided by the unusual [4Fe-3S] cluster. This chapter describes the reactivation kinetics of wild-type MBH (MBH^{wt}) and that of a double mutant carrying a [4Fe-4S] proximal cluster ($MBH^{C19G/C120G}$). The MBH^{wt} and the $MBH^{C19G/C120G}$ were probed under oxidizing conditions and low substrate concentrations.

6.1 Reactivation of MBH^{wt}

In the absence of H_2, the heterotrimeric MBH resides in the Ni-B state (Hidalgo et al., 2015; Saggu et al., 2009), which is thought to protect the active site from irreversible damage (Vincent et al., 2005a). Accumulation of MBH in the Ni-B state in electron

deficient conditions can be reversed upon treatment with low amounts of substrate. Reactivation from the Ni-B state in transient conditions leads to a lag between H_2 exposure and maximum activity, a feature observed in the transient experiments employed for determining $K_M^{H_2}$ (Figure 4.12). Experiments utilising series of short H_2 pulses were carried out to test the kinetics and the reversibility of the reactivation of heterotrimeric MBH at high electrode potentials (Figure 6.1).

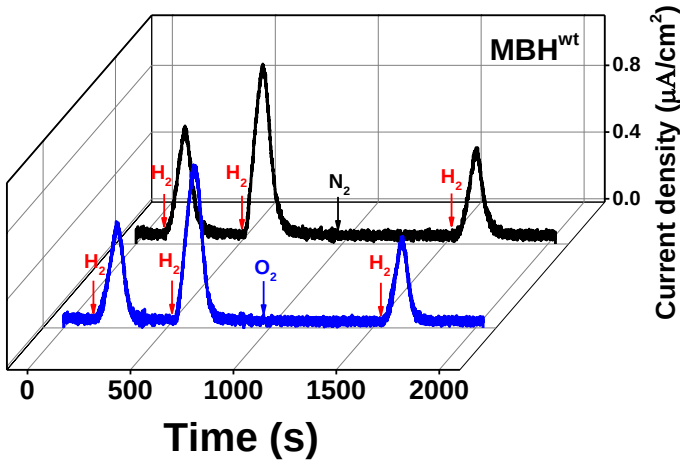

Figure 6.1 Chronoamperograms showing the evolution of the H_2 oxidation current of MBH^{wt} upon applying H_2 pulses intercalated with O_2 and N_2 pulses (0.499 V vs SHE; ubiquinone-containing tBLM; N_2 flushing; 30 °C; pH 7.4; 4:10 dry total protein to dry polar lipids; H_2 concentration after injection: 100 μM; O_2 concentration after injection: 28 μM; the value of τ was determined to be 50 s in the setup employing mechanical stirring, which was used for these experiments).

It was observed that the rate of reactivation after the second pulse of H_2 was 1.5 times higher compared to the rate after the first pulse, based on the slope of the linear domain of current increase at a potential of 0.5 V SHE (normalised rate at 1st reactivation: 92.2 (±13.9) x 10^{-4} s^{-1} (n=9); 2nd reactivation: 136.6 (±11.5) x 10^{-4} s^{-1} (n=9); the time between injections was 449±37 s; the current levels were normalised against the current plateau of the second peak). The treatment with O_2 at different electrode potentials (Figure 6.1, blue trace, and Figure 6.2) did not change the reactivation kinetics upon a third pulse of

H_2 (comparing the reactivation kinetics after O_2 treatment, Figure 6.1 blue trace, with the reactivation kinetics after N_2 treatment, Figure 6.1 black trace). This indicates that after complete substrate depletion, active MBH is converted to the Ni-B state in anaerobic oxidizing conditions.

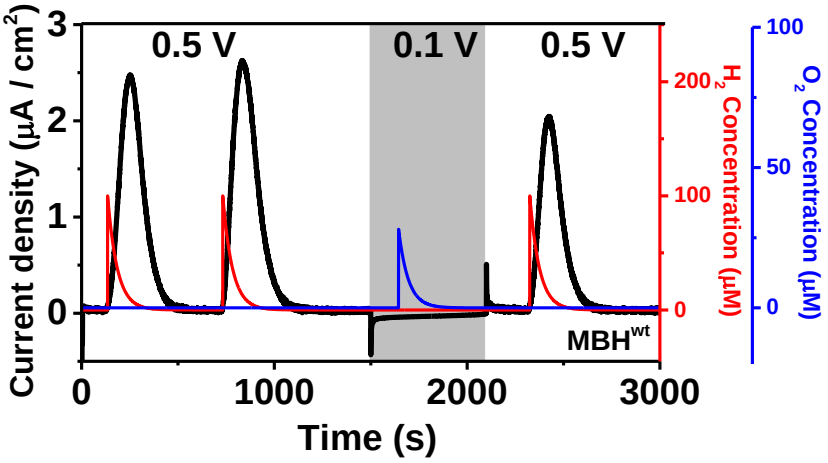

Figure 6.2 Chronoamperogram showing the evolution of the H_2 oxidation current of MBH^{wt} upon applying H_2 pulses intercalated with one O_2 pulse at a potential of 0.1 V (30 °C; pH 7.4; ubiquinone-containing tBLM; 4:10 dry total protein to dry polar lipids; N_2 flushing; H_2 concentration after injection: 100 μM; O_2 concentration after injection: 28 μM; the value of τ was determined to be 50 s in the setup employing mechanical stirring, which was used for these experiments).

The time of oxidative poise between the second and the third H_2 pulse was varied to probe the change in reactivation kinetics. It was found that the rate of reactivation decreases with the time of oxidative poise (Figure 6.3). Conversion to the Ni-B state is almost complete in about 400 s after the total depletion of H_2 from the electrochemical cell. Applying H_2 pulses before the complete conversion to Ni-B leads to the variation in reactivation kinetics caused by the small fractions of reduced/partially reduced enzyme, which contribute to a faster current increase after substrate injection. As expected, after converting the MBH to Ni-B (approximately 650 s after the previous injection of H_2),

the reactivation kinetics are slightly slower or match the ones observed for the first injection (Figure 6.3). The reactivation rates obtained after applying oxidative poises longer than 1000 s are slightly slower than expected. This may be caused by the degradation (or desorption) of the SAM/tBLM at high oxidizing potential during the long-duration experiment, which might lead to a poor coupling of the enzyme to the quinone pool.

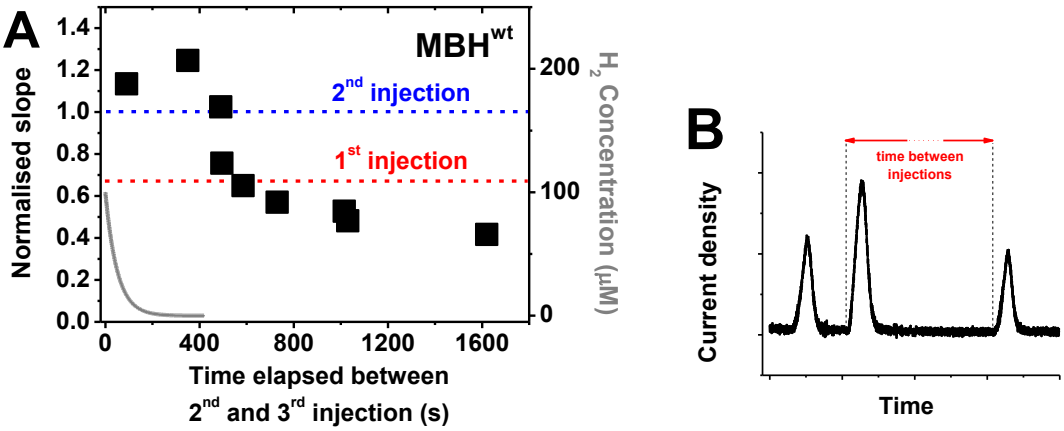

Figure 6.3 (A) The reactivation rate after the third injection of H_2 (based on the slope of the current increase) as a function of the time elapsed between the second and the third injection under N_2. The rates are normalised against the rate obtained after the second injection (MBH^{wt}; 0.499 V vs SHE; ubiquinone-containing tBLMs; 30 °C; pH 7.4; blue dotted line: rate after the second injection; red dotted line: rate after the first injection). The H_2 concentration decay after an injection is plotted in gray (the exponential decay was plotted, as described in Section 4.3.1, according to the equation: $C(t) = C(0)\cdot\exp(-t/\tau)$, where *C* is concentration, and *t* is time; the value of τ was determined to be 50 s in the setup employed for these experiments). (B) Schematic drawing showing the time of oxidative poise between injections that was varied to obtain the time dependency described in (A).

The rate of reactivation was found to increase with temperature (Figure 6.4a). Using the slope of the reactivation trace as the temperature-dependent parameter, the activation energy (E_a) was determined to be 141.5 (±5.0) kJ/mol (n=3) at 0.3 V, in agreement with values obtained for Hyd-1 for which E_a varied from a value of 56.8 (±0.3) kJ/mol at 0.035 V to 96.3 (±0.8) kJ/mol at 0.235 V (Evans et al., 2013). The value of E_a at 0.5 V

was determined to be 131.5 (±9.1) kJ/mol (single data set fitting). The high value of E_a for Ni-B reactivation compared to the activation energy for H_2 oxidation (26 kJ/mol) (Hallahan et al., 1987; Schink and Schlegel, 1979) may be explained on the basis of the major structural changes the [4Fe-3S] proximal cluster undergoes when it performs the redox transitions between the three redox states during the (re)activation process (Frielingsdorf et al., 2014).

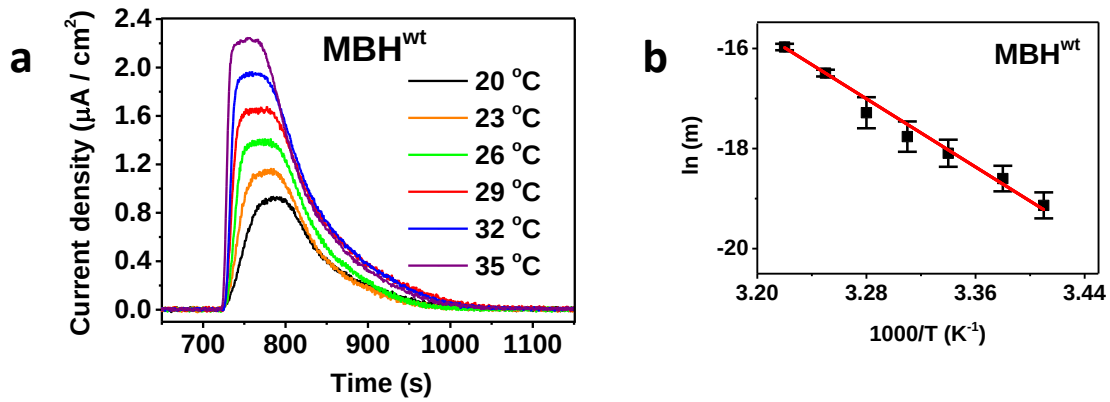

Figure 6.4 (a) Overlay of chronoamperometric traces showing the evolution of the H_2 oxidation current for MBH^{wt} after applying H_2 pulses at different temperatures (0.299 V vs SHE; electron carrier: menaquinone; pH 7.4; 4:10 dry total protein to dry polar lipids; H_2 concentration after injection: 100 µM). (b) Arrhenius plot for Ni-B reactivation of MBH^{wt} (traces were recorded in triplicate in the temperature interval 20-38 °C).

The potential dependence of the reactivation kinetics was investigated in the potential window of 0.2-0.5 V. Instead of ubiquinone-10, which was used as electron mediator in the experiments described so far in this chapter, menaquinone-7 was employed as the oxidation potential of menaquinol is lower compared to ubiquinol, enabling the probing of a wider potential window.

Higher potentials lead to faster turnover (higher plateau currents) due to the increase in the oxidation rate of menaquinol (Figure 6.5). In contrast, the rate of reactivation only

marginally changes with the applied potential. There is a 6% decrease of the slope of the reactivation trace when increasing the potential from 0.2 V to 0.3 V and an 11% drop from 0.3 V to 0.4 V. The heterodimeric sub-complexes of the MBHs from *A. aeolicus* and *E. coli*, display a similar potential dependency of Ni-B reactivation (Evans et al., 2013; Pandelia et al., 2010).

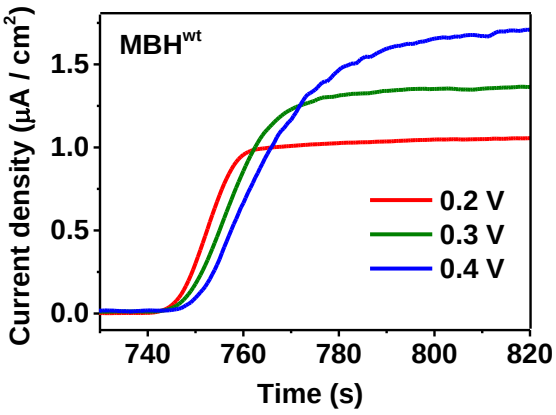

Figure 6.5 Chronoamperograms showing the evolution of the MBH^{wt} H_2 oxidation current after applying H_2 pulses at different potentials (electron carrier: menaquinone; pH 7.4; 30 ^oC; 4:10 dry total protein to dry polar lipids; H_2 concentration after injection: 100 μM).

In order to estimate the fraction of inactive enzyme residing in the Ni-B state under oxidizing conditions, experiments similar to the two-step methods, described in previous PFE studies, were conducted under low substrate concentrations (Evans et al., 2013; Pandelia et al., 2010; Fourmond et al., 2010). Under 0.25% H_2 (equivalent to 2 μM in solution), a potential of 0.5 V was applied for 250 s followed by the reduction of the quinone pool at low potential (-0.2 V) to promote the complete reduction of the enzyme (for 300 s). Afterwards the potential was poised back to the initial value at which MBH oxidizes H_2 (Figure 6.6).

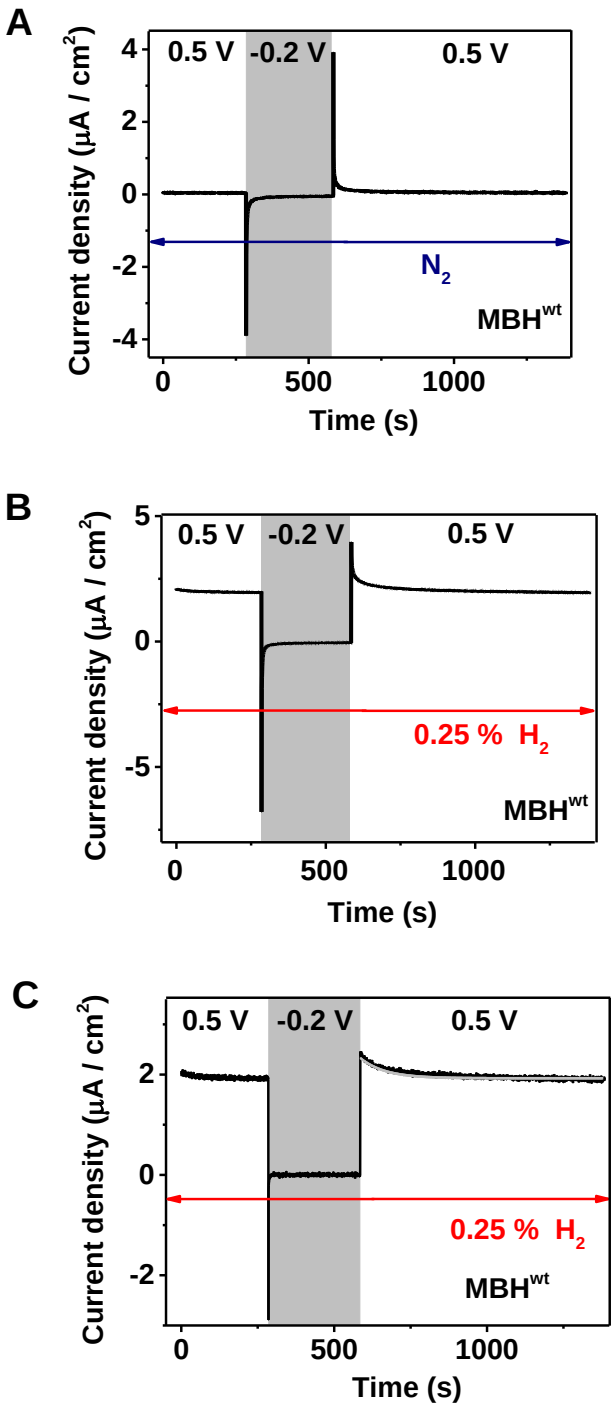

Figure 6.6 Chronoamperograms showing the current response obtained from a tBLM incorporating MBH^{wt} subjected to the potential sequence depicted at the top of each figure (MBH^{wt}; ubiquinone-containing tBLMs; 30 °C; pH 7.4; 4:10 dry total protein to dry polar lipids). (A) Background trace recorded under N_2. (B) Trace recorded under 0.25% H_2. (C) Background-subtracted trace with the fit (according to Equation 35) to the current decay after switching the potential back to 0.5 V (light gray line).

Based on the current level after stepping the potential back to 0.5 V, 16.9±1.2% (n=3) of the enzyme resides in the Ni-B state under low substrate turnover conditions (the ratio of inactive enzyme was obtained by dividing the difference between the current level after the second potential step and the initial current level to the current level after the second potential step). Fitting of the current relaxation curves following reactivation at low potential allowed the determination of the activation (k_a) and inactivation (k_{in}) rate constants. The data treatment was carried out as previously described in studies using two-step methods for determining (in)activation rate constants (Evans et al., 2013; Fourmond et al., 2010). Fitting of the chronoamperometric data using equation 35 yields the rate constant of the exponential relaxation (k_{tot}), which is the sum of k_a and k_{in} (in Equation 35, i_0 is the initial current and i_∞ is the final current).

$$i(t) = (i_0 - i_\infty)\exp(-k_{tot}\, t) + i_\infty \quad (35)$$

The value of k_a can be calculated knowing the initial fraction of active enzyme (A_0), which is assumed to be 1 after reactivation at low potential (Equation 36).

$$k_a = A_0 \frac{i_\infty}{i_0} k_{tot} \quad (36)$$

It was determined that the value of k_{in} is 8.7 (±1.9) x10^{-4} s^{-1} (n=3), about 5 times higher than the k_{in} for the heterodimeric Hyd-1 from *E. coli* (Evans et al., 2013). PFE studies found k_{in} to be independent of the applied potential (Evans et al., 2013; Pandelia et al., 2010). The value of k_a was found to be 37.2 (±11.4) x10^{-4} s^{-1} (n=3), 10 times higher than the k_a of Hyd-1 at +0.235 V (at 5 ^oC, under 100% H_2) (Evans et al., 2013). Inactivation of the heterotrimeric MBH under oxidizing conditions is faster than that of the

heterodimeric Hyd-1. On the other hand, reactivation of the heterotrimeric MBH is one order of magnitude faster than that of the heterodimeric Hyd-1 and four times faster than inactivation. This was expected as it was shown that, unlike the heterodimeric sub-complexes, the heterotrimeric MBH reactivates fast under oxidizing substrate-limiting conditions without requiring the application of reducing electrode potentials, which means that the reactivation rate greatly exceeds inactivation (see Chapter 5).

6.2 Reactivation of MBH$^{C19G/C120G}$

The MBH variant MBH$^{C19G/C120G}$, was probed in the same way as MBH^{wt}. MBH$^{C19G/C120G}$, having glycine residues in the place of the supernumerary cysteines in the small subunit, carries a [4Fe-4S] proximal cluster, and its catalytic properties resemble those of standard [NiFe] hydrogenases. It was shown that MBH$^{C19G/C120G}$ loses almost entirely its activity upon prolonged exposure to O_2, being more sensitive than MBH^{wt} (Goris et al., 2011). However, short O_2 pulses lead to a small extent of inactivation as observed with MBH^{wt} and not full inactivation as observed with standard [NiFe] hydrogenases, possibly due to the retention of some features of O_2 tolerant [NiFe] hydrogenases not pertaining to the coordination sphere of the electron relay.

The activity of MBH$^{C19G/C120G}$ was 4 to 5 times lower compared to MBH^{wt} in the tBLM (Figure 6.7), which can be attributed to the higher sensitivity towards O_2, which leads to irreversible inactivation of the enzyme during extraction from *R. eutropha*. This was previously observed for this variant with spectrophotometric assays (Supplementary Table 1 of Goris et al., 2011). The scans in Figure 6.7 also prove that MBH$^{C19G/C120G}$ can use both menaquinone and ubiquinone as electron acceptor.

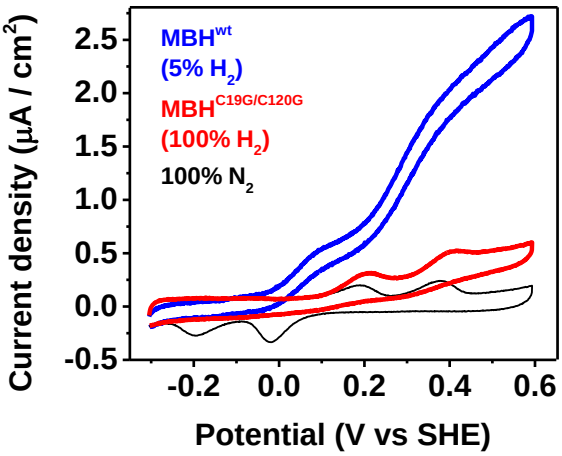

Figure 6.7 Cyclic voltammograms showing the activity level for MBH^{wt} (blue) and $MBH^{C19G/C120G}$ (red) (10 mV/s; tBLMs containing both menaquinone and ubiquinone; 30 ºC; pH 7.4; 4:10 dry total protein to dry polar lipids; the $MBH^{C19G/C120G}$ scan and the blank 100% N_2 scan were recorded on the same tBLM; the quinol oxidation peaks are shifted to higher potentials due to the low capacitance of the tBLM as explained in Section 4.1).

It was found with transient chronoamperometric measurements that $MBH^{C19G/C120G}$ reactivates 7 times faster than MBH^{wt} (Figure 6.8). The normalised rate of current increase for $MBH^{C19G/C120G}$ after a H_2 pulse was determined to be 1027.7 (±41.7) $x10^{-4}$ s^{-1} (n=11).

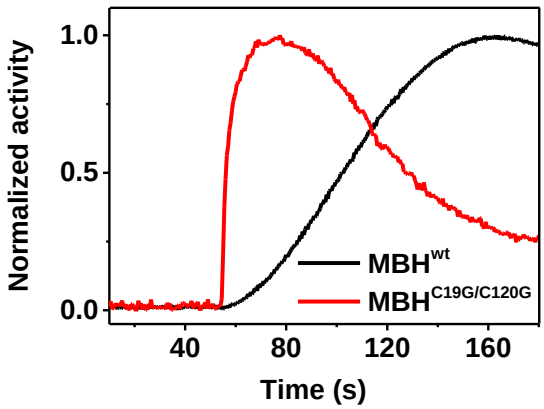

Figure 6.8 Chronoamperometric traces showing the reactivation of MBH^{wt} (black) and $MBH^{C19G/C120G}$ (red) (0.499 V; 30 ºC; pH 7.4; ubiquinone-containing tBLMs; 4:10 dry total protein to dry polar lipids).

In contrast to MBH^{wt}, the reactivation kinetics of MBH$^{C19G/C120G}$ are independent of the time of exposure to oxidizing electrode potentials (Figure 6.9).

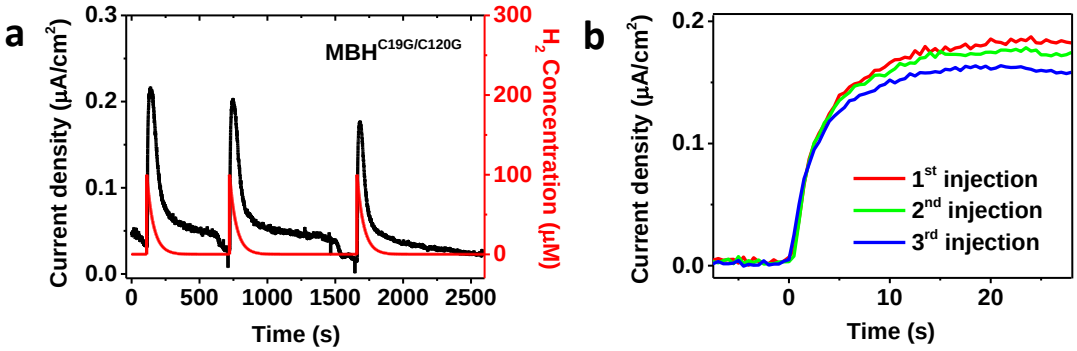

Figure 6.9 Chronoamperograms showing the evolution of the H_2 oxidation activity of MBH$^{C19G/C120G}$ after three H_2 pulses: (a) trace showing the three consecutive pulses; (b) overlay of the background-corrected traces (0.499 V vs SHE; ubiquinone-containing tBLM; 30 °C; pH 7.4; 4:10 dry total protein to dry polar lipids; H_2 concentration after injection: 100 µM).

The temperature-dependence of the reactivation kinetics of MBH$^{C19G/C120G}$ was tested between 30 °C and 36 °C (Figure 6.10a). The temperature window was restricted by the low stability of the variant above 36 °C and the low signal to noise ratio obtained below 30 °C. E_a, calculated in the same way as for the MBH^{wt}, was determined to be 22.2 (±8.1) kJ/mol (n=4) at 0.5 V (Figure 6.10b). The reactivation energy barrier is significantly lower than in the case of MBH^{wt} (141.5 (±5.0) kJ/mol at 0.3 V) and comparable to the E_a for H_2 oxidation (Leger et al., 2002b; Hallahan et al., 1987; Schink and Schlegel, 1979). This indicates that the slower reactivation kinetics of MBH^{wt} might be caused by the the structural rearrangements of the proximal [4Fe-3S] cluster associated with the reduction from the superoxidized state.

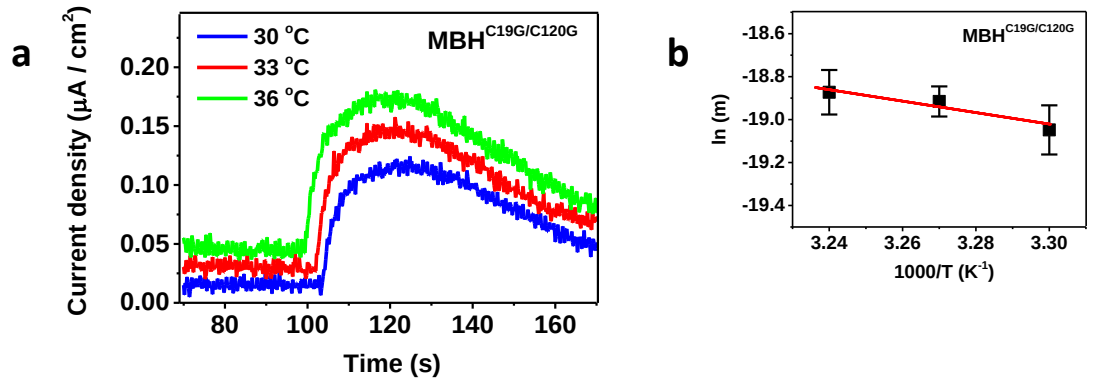

Figure 6.10 (a) Chronoamperograms showing the evolution of the H_2 oxidation current after applying H_2 pulses at different temperatures for $MBH^{C19G/C120G}$ (0.499 V vs SHE; electron carrier: ubiquinone; pH 7.4; 4:10 dry total protein to dry polar lipids; H_2 concentration after injection: 100 μM; the traces are offset for clarity). (b) Arrhenius plot for $MBH^{C19G/C120G}$ Ni-B reactivation (0.499 V; ubiquinone-containing tBLMs; 11 traces were recorded at 30 °C and 4 traces at 33 °C and 36 °C; the slope of the reactivation trace, m, was taken as the temperature-dependent variable as in the case of MBH^{wt}).

6.3 Conclusions

It was shown that, like the heterodimeric sub-complexes of O_2-tolerant MBHs, the heterotrimeric MBH resides in the Ni-B state at high potential in the absence of H_2. Under substrate limiting conditions, approximately 16% of the enzyme molecules are found in the Ni-B state.

Reactivation from the Ni-B state was found to be strongly dependent on temperature. The higher reactivation energy barrier of MBH^{wt} compared to $MBH^{C19G/C120G}$ points to a differentiation of the reactivation pathways determined by the electrochemical properties of the proximal cluster. The data presented in this chapter indicate that, after prolonged exposure to oxidizing conditions in the absence of H_2, the proximal cluster of MBH^{wt} resides in the most oxidized state ($[4Fe\text{-}3S]^{5+}$). It can also be hypothesised that the reactivation kinetics of MBH^{wt} are rate limited by the reduction of the superoxidized $[4Fe\text{-}3S]^{5+}$ cluster. The relatively slow reduction of the $[4Fe\text{-}3S]^{5+}$ cluster compared to

that of other [FeS] clusters can be explained by the chemical reorganisation that is coupled to this step (Frielingsdorf et al., 2014; Fritsch et al., 2011a).

O_2-tolerant [NiFe] hydrogenases like the ones from *R. eutropha* and *A. aeolicus* display a higher rate of anaerobic inactivation compared to standard [NiFe] hydrogenases like the ones from *Allochromatium vinosum* and *Desulfovibrio gigas* (Pandelia et al., 2010; Vincent et al., 2005a). The faster inactivation of O_2-tolerant hydrogenases, associated to Ni-B formation, might be related to the oxidation of the proximal cluster to the 5+ state (Evans et al., 2013; Fritsch et al., 2011ab). It can be hypothesized that the slow reduction of the superoxidized cluster, which retards enzyme reactivation, prevents irreversible damage to the active site under aerobic conditions. Impaired electron transfer to the [NiFe] active site would halt the formation of radical oxygen species, which normally would lead to complete loss of enzymatic activity after reacting at the metal centre. Unlike O_2-tolerant [NiFe] hydrogenases, standard [NiFe] hydrogenases maintain electron transfer to the active site via the electron relay under aerobic conditions. The continuous supply of electrons to the active site favours the formation of damaging reactive oxygen species, which might result in the accumulation of the inactive Ni-A state. One would therefore infer that O_2-tolerant [NiFe] hydrogenases avoid the accumulation of unready states in highly oxidizing conditions via superoxidation of the proximal cluster, which slows down reverse electron transfer through the [FeS] relay, resulting in the shutdown of the active site reactivity.

7. General conclusions

O_2 tolerant MBHs are distinguished as peculiar in the class of [NiFe] hydrogenases due to their catalytic properties under oxidizing conditions. Electron availability at the active site plays a major role in selective H_2 oxidation. The very low $K_M^{H_2}$ values ensure that the number of reactive encounters at the active site is greater for H_2 than for O_2 molecules. Electron availability controls the outcome of the very seldom "successful" O_2 encounters. The change in the oxidation state brought about by the O_2 molecule via the Ni-B state is controlled by the unusual proximal [4Fe-3S] cluster, which provides two of the electrons necessary for the formation of the bridging OH^- at the active site. In the case of the heterodimeric sub-complexes of MBHs, the electron required for the reactivation to the active Ni-S state is provided under reducing conditions. The data presented in this thesis show that reactivation from the Ni-B state can take place under oxidizing conditions. The full heterotrimeric MBH, in equilibrium with the quinone pool, displays a higher level of tolerance to anaerobic oxidizing conditions compared to the heterodimeric sub-complexes of MBHs and recovers from O_2 inactivation without requiring reducing conditions. It was also shown that the proximal [4Fe-3S] cluster might play a role in the protection of the active site from oxidative damage under substrate scarce conditions. Protection would be achieved not only by trapping the O_2 molecules as an OH^-, but also by halting the delivery of electrons, which lowers the active site reactivity under oxidizing conditions.

Oligomerization of MBHs in the cytoplasmic membrane, which was proposed in the case of several organisms growing on H_2 (Bowman et al., 2014; Volbeda et al., 2012;

Frielingsdorf et al., 2011; Shomura et al., 2011), was suggested to enable intermolecular electron transfer via the distal [4Fe-4S] cluster (Volbeda et al., 2013; Fritsch et al., 2013). The provision of the electron required for reactivation from the Ni-B state would be possible in an oligomeric complex when the active and the inactive metal centres of the proteins are in electrochemical equilibrium. Reactivation through this pathway would be possible even under oxidizing conditions, which is what was observed in the experiments described in this thesis. The heterotrimeric MBH in the cytoplasmic membrane recovered activity rapidly even in aerobic conditions (before the complete removal of O_2). Recently published data comparing the catalytic properties of the monomeric Hyd-1 from *E. coli* with its oligomeric form also supports the hypothesis that intermolecular electron transfer enhances the tolerance towards oxidizing conditions, underlining the role of the quaternary structure in H_2 catalysis by O_2 tolerant MBHs (Wulff et al., 2016).

Hydrogenase reactivation achieved by placing in electrochemical equilibrium active enzyme molecules with inactive ones has indeed been reported for a biofuel-cell operating under oxidizing conditions (Wait et al., 2010). An anode with adsorbed inactive Hyd-1 from *E. coli* was connected to another anode prepared in the same way with active enzyme. Activity recovery was rapid despite maintaining the two anodes in the same oxidizing conditions that inactivated the first anode (4% H_2 / 96% air).

The fine tuning of electron availability could be at the basis of the properties of hydrogenases under oxidizing conditions. The probing of redox enzymes in their native environment and in equilibrium with their native redox partners could offer answers regarding the complex mechanism of H_2 activation under parameters similar to the ones

encountered in organisms relying on hydrogenases for energy conversion. The mild operating conditions (low temperature and almost neutral pH) under which hydrogenases can convert fuel to electricity represent a crucial aspect to be taken into consideration in the design of concepts of efficient and sustainable processes for energy technologies. Therefore, the experimental results regarding redox processes involved in enzymatic H_2 cycling should be evaluated in terms of efficient tuning of electron availability under oxidizing conditions.

References

Abou Hamdan, A., Dementin, S., Liebgott, P.-P., Gutierrez-Sanz, O., Richaud, P., De Lacey, A. L., Rousset, M., Bertrand, P., Cournac, L., and Leger, C. (2012). Understanding and Tuning the Catalytic Bias of Hydrogenase. J. Am. Chem. Soc. 134, 8368-8371.

Abou Hamdan, A., Burlat, B., Gutierrez-Sanz, O., Liebgott, P. P., Baffert, C., De Lacey, A. L., Rousset, M., Guigliarelli, B., Leger, C., and Dementin, S. (2013). O_2-Independent Formation of the Inactive States of NiFe-Hydrogenase. Nat. Chem. Biol. 9, 15-18.

Adamska, A., Silakov, A., Lambertz, C., Rüdiger, O., Happe, T., Reijerse, E., and Lubitz, W. (2012). Identification and Characterization of the "Super-Reduced" State of the H-Cluster in [FeFe] Hydrogenase: A New Building Block for the Catalytic Cycle? Angew. Chem., Int. Ed. 51, 11458-11462.

Adzic, R., Zhang, J., Sasaki, K., Vukmirovic, M., Shao, M., and Wang, J. (2006). DOE 2006 Annual Progress Report, U.S. Department of Energy, 783-786.

Ahluwalia, R. K., Wang, X., and Kumar, R. (2006). DOE 2006 Annual Progress Report, U.S. Department of Energy, 870–874.

Alonso-Lomillo, M. A., Rüdiger, O., Maroto-Valiente, A., Velez, M., Rodriguez-Ramos, I., Munoz, F. J., Fernández, V. M., and de Lacey, A. L. (2007). Hydrogenase-Coated Carbon Nanotubes for Efficient H_2 Oxidation. Nano Lett. 7, 1603-1608.

Armstrong, F. A., Heering, H. A., and Hirst, J. (1997). Reactions of complex metalloproteins studied by protein-film voltammetry. Chem. Soc. Rev. 26, 169-179.

Armstrong, F. A. (2004). Hydrogenases: active site puzzles and progress. Curr. Opin. Chem. Biol. 8, 133–140.

Armstrong, F. A., Belsey, N. A., Cracknell, J. A., Goldet, G., Parkin, A., Reisner, E., Vincent, K. A., and Wait, A. F. (2009). Dynamic electrochemical investigations of hydrogen oxidation and production by enzymes and implications for future technology. Chem. Soc. Rev. 38, 36–51.

Ataka, K., Richter, B., and Heberle, J. (2006). Orientational Control of the Physiological Reaction of Cytochrome *c* Oxidase Tethered to a Gold Electrode. J. Phys. Chem. B 110, 9339–9347.

Atkins, P., and de Paula, J. (2006). Atkins' Physical Chemistry, Oxford University Press, Oxford.

Baffert, C., Demuez, M., Cournac, L., Burlat, B., Guigliarelli, B., Bertrand, P., Girbal, L., and Léger, C. (2008). Hydrogen-Activating Enzymes: Activity Does Not Correlate with Oxygen Sensitivity. Angew. Chem. Int. Ed. 47, 2052-2054.

Bard, A. J., and Faulkner, L. R. (2001). Electrochemical Methods: Fundamentals and Applications, 2nd Ed., John Wiley and Sons, Inc., New York.

Bard, A. J., Stratmann, M., and Unwin, P. R. (2003). Encyclopedia of Electrochemistry, Vol. 3, Instrumentation and Electroanalytical Chemistry, Wiley-VCH, Weinheim.

Baur, J., Le Goff, A., Dementin, S., Holzinger, M., Rousset, M., and Cosnier, S. (2011). Three-dimensional carbon nanotube-polypyrrole-[NiFe] hydrogenase electrodes for the efficient electrocatalytic oxidation of H_2. Int. J. Hydrogen Energ. 36, 12096-12101.

Berggren, G., Adamska, A., Lambertz, C., Simmons, T. R., Esselborn, J., Atta, M., Gambarelli, S., Mouesca, J. M., Reijerse, E., Lubitz, W., Happe, T., Artero, V., and Fontecave, M. (2013). Biomimetic assembly and activation of [FeFe]-hydrogenases. Nature 499, 66-69.

Bernhard, M., Benelli, B., Hochkoeppler, A., Zannoni, D., and Friedrich, B. (1997). Functional and structural role of the cytochrome *b* subunit of the membrane-bound hydrogenase complex of *Alcaligenes eutrophus* H16. Eur. J. Biochem. 248, 179-186.

Bisquert, J., Garcia-Belmonte, G., Bueno, P., Longo, E., and Bulhoes, L. O. S. (1998). Impedance of constant phase element (CPE)-blocked diffusion in film electrodes. J. Electroanal. Chem. 452, 29 – 234.

Blanford, C. F., and Armstrong, F. A. (2006). The pyrolytic graphite surface as an enzyme substrate: microscopic and spectroscopic studies. J. Solid State Electrochem. 10, 826–832.

Bleijlevens, B., Faber, B. W., and Albracht, S. P. J. J. (2001). The [NiFe] hydrogenase from Allochromatium vinosum studied in EPR-detectable states: H/D experimentsthat yield new information about the structure of the active site. Biol. Inorg. Chem. 6, 763-769.

Boden, N., Bushby, R.J., Clarkson, S., Evans, S.D., Knowles, P.F., and Marsh, A. (1997). The design and synthesis of simple molecular tethers for binding biomembranes to a gold surface. Tetrahedron 53, 10939–10952.

Bowman, L., Flanagan, L., Fyfe, P. K., Parkin, A., Hunter, W. N., Sargent, F. (2014). How the structure of the large subunit controls function in an oxygen-tolerant [NiFe]-hydrogenase. Biochem. J. 458, 449–458.

Brecht, M., van Gastel, M., Buhrke, T., Friedrich, B. and Lubitz, W. (2003). Direct detection of a hydrogen ligand in the [NiFe] center of the regulatory H_2-sensing hydrogenase from Ralstonia eutropha in its reduced state by HYSCORE and ENDOR spectroscopy. J. Am. Chem. Soc. 125, 13075–13083.

Cammack, R., Fernandez, V. M., Hatchikian, E. C. (1994). Nickel-Iron Hydrogenase. Methods Enzymol. 243, 43-68.

Chidsey, C. E. D. (1991). Free Energy and Temperature Dependence of Electron Transfer at the Metal-Electrolyte Interface. Science 251, 919-922.

Christenson, A., Gustavsson, T., Gorton L., and Hägerhäll, C. (2008). Direct and mediated electron transfer between intact succinate: quinone oxidoreductase from *Bacillus subtilis* and a surface modified gold electrode reveals redox state-dependent conformational changes. Biochim. Biophys. Acta. Bioenerg. 1777, 1203–1210.

Ciaccafava, A., De Poulpiquet, A., Techer, V., Giudici-Orticoni, M. T., Tingry, S., Innocent, C., and Lojou, E. (2012). An innovative powerful and mediatorless H_2/O_2 biofuel cell based on anoutstanding bioanode. Electrochem. Commun. 23, 25-28.

Clarke, T. A., Kemp, G. L., Van Wonderen, J. H., Doyle, R., Cole, J. A., Tovell, N., Cheesman, M. R., Butt, J. N., Richardson, D. J., and Hemmings, A. M. (2008). Role of a Conserved Glutamine Residue in Tuning the Catalytic Activity of *Escherichia coli* Cytochrome *c* Nitrite Reductase. Biochemistry 47, 3789–3799.

Constant, P., Chowdhury, S. P., Hesse, L., Pratscher, J., and Conrad, R. **(**2011). Genome data mining and soil survey for the novel group 5 [NiFe] hydrogenase to explore the diversity and ecological importance of presumptive high-affinity H_2-oxidizing bacteria. Appl. Environ. Microbiol. 77, 6027–6035.

Cracknell, J. A., Vincent, K. A., Ludwig, M., Lenz, O., Friedrich, B., and Armstrong, F. A. (2008a). Enzymatic Oxidation of H_2 in Atmospheric O_2: The Electrochemistry of Energy Generation from Trace H_2 by Aerobic Microorganisms. J. Am. Chem. Soc. 130, 424-425.

Cracknell, J. A., Vincent, K. A., and Armstrong, F. A. (2008b). Enzymes as Working or Inspirational Electrocatalysts for Fuel Cells and Electrolysis. Chem. Rev. 108, 2439–2461.

Cracknell, J. A., Wait, A. F., Lenz, O., Friedrich, B., and Armstrong, F. A. (2009). A kinetic and thermodynamic understanding of O_2 tolerance in [NiFe] hydrogenases. Proc. Natl. Acad. Sci. USA 106, 20681–20686.

Cramm, R., (2009). Genomic View of Energy Metabolism in Ralstonia eutropha H16. J. Mol. Microbiol. Biotechnol. 16, 38–52.

Cullison, J. K., Hawkridge, F. M., Nakashima, N., and Yoshikawa, S. (1994). A Study of Cytochrome c Oxidase in Lipid Bilayer Membranes on Electrode Surfaces. Langmuir 10, 877–882.

De Poulpiquet, A., Ranava, D., Monsalve, K., Giudici-Orticoni, M.-T., and Lojou, E. (2014). Biohydrogen for a New Generation of H_2/O_2 Biofuel Cells: A Sustainable Energy Perspective. ChemElectroChem 1, 1724-1750.

De Poulpiquet, A., Ciaccafava, A., Szot, K., Pillain, B., Infossi, P., Guiral, M., Opallo, M., Giudici-Orticoni, M. T., and Lojou, E. (2013). Exploring Properties of a Hyperthermophilic Membrane-Bound Hydrogenase at Carbon Nanotube Modified Electrodes for a Powerful H_2/O_2 Biofuel Cell. Electroanalysis 25, 685-695.

Dementin, S., Leroux, F., Cournac, L., De Lacey, A. L., Volbeda, A., Leger, C., Burlat, B., Martinez, N., Champ, S., Martin, L., Sanganas, O., Haumann, M., Fernandez, V. M., Guigliarelli, B., Fontecilla-Camps, J. C., and Rousset, M. (2009) Introduction of Methionines in the Gas Channel Makes [NiFe] Hydrogenase Aero-Tolerant. J. Am. Chem. Soc. 131, 10156-10164.

Devadoss, A., and Burgess, J. D. (2002). Detection of Cholesterol through Electron Transfer to Cholesterol Oxidase in Electrode-Supported Lipid Bilayer Membranes. Langmuir 18, 9617–9621.

Di Bernardo, S., Fato, R., Casadio, R., Fariselli, P., and Lenaz, G. (1998). A high diffusion coefficient for coenzyme Q_{10} might be related to a folded structure. FEBS Lett. 426, 77-80.

Dodd, C. E., Johnson, B. R. G., Jeuken, L. J. C., Bugg, T. D. H., Bushby, R. J., and Evans, S. D. (2008). Native *E. coli* inner membrane incorporation in solid-supported lipid bilayer membranes. Biointerphases 3, 59-67.

Elliott, S. J., Hoke, K. R., Heffron, K., Palak, M., Rothery, R. A., Weiner, J. H., and Armstrong, F. A. (2004). Voltammetric Studies of the Catalytic Mechanism of the Respiratory Nitrate Reductase from Escherichia coli: How Nitrate Reduction and Inhibition Depend on the Oxidation State of the Active Site. Biochemistry 43, 799–807.

Esselborn, J., Lambertz, C., Adamska-Venkatesh, A., Simmons, T., Berggren, G., Noth, J., Siebel, J. F., Hemschemeier, A., Artero, V., Reijerse, E. J., Fontecave, M., Lubitz, W., and Happe, T. (2013). Spontaneous activation of [FeFe]-hydrogenases by an inorganic [2Fe] active site mimic. Nat. Chem. Biol. 9, 607-609.

Evans, D. J., and Pickett, C. J. (2003). Chemistry and the hydrogenases. Chem. Soc. Rev. 32, 268–275.

Evans, R. M., Parkin, A., Roessler, M. M., Murphy, B. J., Adamson, H., Lukey, M. J., Sargent, F., Volbeda, A., Fontecilla-Camps, J. C., and Armstrong, F. A. (2013). Principles of Sustained Enzymatic Hydrogen Oxidation in the Presence of Oxygen−The Crucial Influence of High Potential Fe−S Clusters in the Electron Relay of [NiFe]-Hydrogenases. J. Am. Chem. Soc. 135, 2694−2707.

Evans, R. M., Brooke, E. J., Wehlin, S. A. M., Nomerotskaia, E., Sargent, F., Carr, S. B., Phillips, S. E. V., and Armstrong, F. A. (2016). Mechanism of hydrogen activation by [NiFe] hydrogenases. Nat. Chem. Biol. 12, 46-50.

Fato, R., Battino, M., Esposti, M. D., Parenti Castelli, G., and Lenaz, G. (1986). Determination of Partition and Lateral Diffusion Coefficients of Ubiquinones by Fluorescence Quenching of n-(9-Anthroyloxy)stearic Acids in Phospholipid Vesicles and Mitochondrial Membranes. Biochemistry 25, 3378-3390.

Fontecilla-Camps, J. C., Volbeda, A., Cavazza, C., and Nicolet, Y. (2007). Structure/Function Relationships of [NiFe]- and [FeFe]-Hydrogenases. Chem. Rev. 107, 4273−4303.

Fourmond, V., Infossi, P., Giudici-Orticoni, M.-T., Bertrand, P., and Leger, C. (2010). "Two-Step" Chronoamperometric Method for Studying the Anaerobic Inactivation of an Oxygen Tolerant NiFe Hydrogenase. J. Am. Chem. Soc. 132, 4848–4857.

Friedrich, M. G., Plum, M. A., Santonicola, M. G., Kirste, V. U., Knoll, W., Ludwig, B., and Naumann, R. L. C. (2008a) In Situ Monitoring of the Catalytic Activity of Cytochrome *c* Oxidase in a Biomimetic Architecture. Biophys. J. 95, 1500–1510.

Friedrich, M. G., Kirste, V. U., Zhu, J. P., Gennis, R. B., Knoll W., and Naumann, R. L. C. (2008b). Activity of Membrane Proteins Immobilized on Surfaces as a Function of Packing Density. J. Phys. Chem. B 112, 3193–3201.

Friedrich, M. G., Robertson, J. W. F., Walz, D., Knoll, W., and Naumann, R. L. C. (2008c). Electronic Wiring of a Multi-Redox Site Membrane Protein in a Biomimetic Surface Architecture. Biophys. J., 2008, 94, 3698–3705.

Friedrich, B., Fritsch, J., and Lenz, O. (2011). Oxygen-tolerant hydrogenases in hydrogen-based technologies. Curr. Opin. Biotechnol. 22, 358–364.

Frielingsdorf, S., Schubert, T., Pohlmann, A., Lenz, O., and Friedrich, B. (2011). A Trimeric Supercomplex of the Oxygen-Tolerant Membrane-Bound [NiFe] hydrogenase from Ralstonia eutropha H16. Biochemistry 50, 10836−10843.

Frielingsdorf, S., Fritsch, J., Schmidt, A., Hammer, M., Löwenstein, J., Siebert, E., Pelmenschikov, V., Jaenicke, T., Kalms, J., Rippers, Y., Lendzian, F., Zebger, I., Teutloff, C., Kaup, M., Bittl, R., Hildebrandt, P., Friedrich, B., Lenz, O., and Scheerer, P. (2014). Reversible [4Fe-3S] Cluster Morphing in an O_2-Tolerant Hydrogenase. Nat. Chem. Biol. 10, 378-385.

Fritsch, J., Scheerer, P., Frielingsdorf, S., Kroschinsky, S., Friedrich, B., Lenz, O. and Spahn, C. M. T. (2011a). The crystal structure of an oxygen-tolerant hydrogenase uncovers a novel iron-sulphur centre. Nature 479, 249-253.

Fritsch, J., Löscher, S., Sanganas, O., Siebert, E., Zebger, I., Stein, M., Ludwig, M., De Lacey, A. L., Dau, H., Friedrich, B., Lenz, O., and Haumann, M. (2011b). [NiFe] and [FeS] Cofactors in the Membrane-Bound Hydrogenase of Ralstonia eutropha Investigated by X-ray Absorption Spectroscopy: Insights into O_2-Tolerant H_2 Cleavage. Biochemistry 50, 5858–5869.

Fritsch, J., Lenz, O., and Friedrich, B. (2013). Structure, function and biosynthesis of O_2-tolerant hydrogenases. Nature 11, 106-114.

Garcin, E., Vernède, X., Hatchikian, E. C., Volbeda, A., Frey, M., Fontecilla-Camps, J. C. (1999). The crystal structure of a reduced [NiFeSe] hydrogenase provides an image of the activated catalytic center. Structure 7, 557-566.

George, S. J., Kurkin, S., Thorneley, R. N. F., and Albracht, S. P. J. (2004). Reactions of H_2, CO, and O_2 with Active [NiFe] hydrogenase from *Allochromatium vinosum*. A Stopped-Flow Infrared Study**.** Biochemistry 43, 6808-6819.

Goldet, G., Wait, A. F., Cracknell, J. A., Vincent, K. A., Ludwig, M., Lenz, O., Friedrich, B. and Armstrong, F. A. (2008). Hydrogen Production under Aerobic Conditions by Membrane-Bound Hydrogenases from Ralstonia Species. J. Am. Chem. Soc. 130, 11106–11113.

Goldet, G., Brandmayr, C., Stripp, S. T., Happe, T., Cavazza, C., Fontecilla-Camps, J. C., and Armstrong, F. A. (2009). Electrochemical Kinetic Investigations of the Reactions of [FeFe]-Hydrogenases with Carbon Monoxide and Oxygen: Comparing the Importance of Gas Tunnels and Active-Site Electronic/Redox Effects. J. Am. Chem. Soc. 131, 14979–14989.

Gordillo, G. J., and Schiffrin, D. J. (2000). The Electrochemistry of Ubiquinone-10 in a Phospholipid Model Membrane. Faraday Discuss. 116, 89.

Goris, T., Wait, A. F., Saggu, M., Fritsch, J., Heidary, N., Stein, M., Zebger, I., Lendzian, F., Armstrong, F. A., Friedrich, B., and Lenz, O. (2011). A Unique Iron-Sulfur Cluster is Crucial for Oxygen Tolerance of a [NiFe]-Hydrogenase. Nat. Chem. Biol. 7, 310-318. Correction published: Nat. Chem. Biol. 2011, 7, 648.

Gutierrez-Sanchez, C., Olea, D., Marques, M., Fernandez, V. M., Pereira, I. A. C., Velez, M., De Lacey, A. L. (2011). Oriented Immobilization of a Membrane-Bound Hydrogenase onto an Electrode for Direct Electron Transfer. Langmuir 27, 6449−6457.

Hackenbrock, C. R., Chazotte, B., and Gupte, S. S. (1986). The random collision model and a critical assessment of diffusion and collision in mitochondrial electron transport. J. Bioenerg. Biomembr. 18, 331-368.

Haji, V., Baffert, C., Sybirna, K., Meynial-Salles, I., Soucaille, P., Bottin, H., Fourmond, V., and Leger, C. (2014). FeFe hydrogenase reductive inactivation and implication for catalysis. Energy Environ. Sci. 7, 715-719.

Hallahan, D. L., Hernandez, V. M., and Hall, D. O. (1987). Reversible Activation of Hydrogenase from *Escherichia coli*. Eur. J. Biochem. 165, 621-625.

Heering, H. A., Hirst, J., and Armstrong, F. A. (1998). Interpreting the Catalytic Voltammetry of Electroactive Enzymes Adsorbed on Electrodes. J. Phys. Chem. B 102, 6889-6902.

Heinekey, D. M. (2009). Hydrogenase enzymes: Recent structural studies and active site models. J. Organomet. Chem. 694, 2671–2680.

Heinze, J. (1984). Cyclic Voltammetry - “Electrochemical Spectroscopy”. Angew. Chem. Int. Ed. Engl. 23, 831-847.

Hexter, S. V., Grey, F., Happe, T., Climent, V., and Armstrong, F. A. (2012). Electrocatalytic mechanism of reversible hydrogen cycling by enzymes and distinctions between the major classes of hydrogenases. Proc. Natl. Acad. Sci. U.S.A. 109, 11516-11521. Correction published: Proc. Natl. Acad. Sci. U.S.A. 2012, 109, 18232-18233.

Hexter, S. V., Chung, M.-W., Vincent K. A., and Armstrong, F. A. (2014). Unusual Reaction of [NiFe]-Hydrogenases with Cyanide. J. Am. Chem. Soc. 136, 10470−10477.

Hidalgo, R., Ash, P. A., Healy, A. J., and Vincent, K. A. (2015). Infrared Spectroscopy During Electrocatalytic Turnover Reveals the Ni-L Active Site State During H_2 Oxidation by a NiFe Hydrogenase. Angew. Chem. Int. Ed. 54, 7110 –7113.

Hirst, J., and Armstrong, F. A. (1998). Fast-Scan Cyclic Voltammetry of Protein Films on Pyrolytic Graphite Edge Electrodes: Characteristics of Electron Exchange. Anal. Chem. 70, 5062-5071.

Hitzbleck, M., Thang Vu, X., Ingebrandt, S., Offenhäusser, A., and Mayer, D. (2013). Functional peptides for capacitative detection of Ca^{2+} ions. Phys. Status Solidi A 5, 1030-1037.

Hoeben, F. J. M., Heller, I., Albracht, S. P. J., Dekker, C., Lemay, S. G., and Heering, H. A. (2008). Polymyxin-Coated Au and Carbon Nanotube Electrodes for Stable [NiFe]-Hydrogenase Film Voltammetry. Langmuir 24, 5925–5931.

Horch, M., Lauterbach, L., Lenz, O., Hildebrandt, P., and Zebger, I. (2012). NAD(H)-coupled hydrogen cycling – structure–function relationships of bidirectional [NiFe] hydrogenases. FEBS Lett. 586, 545-556.

Hrabakova, J., Ataka, K., Heberle, J., Hildebrandt, P., and Murgida, D. H. (2006). Long distance electron transfer in cytochrome c oxidase immobilised on electrodes. A surface enhanced resonance Raman spectroscopic study. Phys. Chem. Chem. Phys. 8, 759–766.

Infossi, P., Lojou, E., Chauvin, J.-P., Herbette, G., Brugna, M., Giudici-Orticoni, M.-T. (2010). Aquifex aeolicus membrane hydrogenase for hydrogen biooxidation: Role of lipids and physiological partners in enzyme stability and activity. Int. J. Hydrogen Energy 35, 10778-10789.

Jadhav, S. R., Sui, D., Garavito, R. M., and Worden, R. M. (2008). Fabrication of highly insulating tethered bilayer lipid membrane using yeast cell membrane fractions for measuring ion channel activity. J. Colloid Interface Sci. 322, 465–472.

Janshoff, A., and Steinem, C. (2006). Transport across artificial membranes–an analytical perspective. Anal. Bioanal. Chem. 385, 433–451.

Jeuken, L. J. C., Connell, S. D., Nurnabi, M., O'Reilly, J., Henderson, P. J. F., Evans, S. D., and Bushby, R. J. (2005) Direct Electrochemical Interaction between a Modified Gold Electrode and a Bacterial Membrane Extract. Langmuir 21, 1481-1488.

Jeuken, L. J. C., Connell, S. D., Henderson, P. J. F., Gennis, R. B., Evans, S. D., and Bushby, R. J. (2006). Redox Enzymes in Tethered Membranes. J. Am. Chem. Soc. 128, 1711-1716.

Jeuken, L. J. C., Daskalakis, N. N., Hana, X., Sheikh, K., Erbe, A., Bushby, R. J., and Evans, S. D. (2007a). Phase separation in mixed self-assembled monolayers and its effect on biomimetic membranes. Sens. Actuators, B 124, 501–509.

Jeuken, L. J. C., Bushby, R. J., and Evans, S. D. (2007b). Proton transport into a tethered bilayer lipid membrane. Electrochem. Commun. 9, 610–614.

Jeuken, L. J. C., Weiss, S. A., Henderson, P. J. F., Evans, S. D., and Bushby, R. J. (2008). Impedance Spectroscopy of Bacterial Membranes: Coenzyme-Q Diffusion in a Finite Diffusion Layer. Anal. Chem. 80, 9084–9090.

Jeuken, L. J. C. (2009). Electrodes for integral membrane enzymes. Nat. Prod. Rep. 26, 1234–1240.

Jones, A. K., Sillery, E., Albracht, S. P. J., and Armstrong, F. A. (2002). Direct comparison of the electrocatalytic oxidation of hydrogen by an enzyme and a platinum catalyst. Chem. Commun. 866–867.

Jones, A. K., Lamle, S. E., Pershad, H. R., Vincent, K. A., Albracht, S. P. J., and Armstrong, F. A. (2003). Enzyme Electrokinetics: Electrochemical Studies of the Anaerobic Interconversions between Active and Inactive States of Allochromatium vinosum [NiFe] hydrogenase. J. Am. Chem. Soc. 125, 8505-8514.

Jorcin, J.-B., Orazem, M. E., Pebere, N., and Tribollet, B. (2006). CPE analysis by local electrochemical impedance spectroscopy. Electrochim. Acta 51, 1473–1479.

Kalms, J., Schmidt, A., Frielingsdorf, S., van der Linden, P., von Stetten, D., Lenz, O., Carpentier, P., and Scheerer, P. (2016). Krypton Derivatization of an O2-Tolerant Membrane-Bound [NiFe] Hydrogenase Reveals a Hydrophobic Tunnel Network for Gas Transport. Angew. Chem. Int. Ed. 55, In Press.

Karyakin, A. A., Morozov, S. V., Karyakina, E. E., Zorin, N. A., Perelygin, V. V., and Cosnier, S. (2005). Hydrogenase electrodes for fuel cells. Biochem. Soc. Trans. 33, 73-75.

Kim, D.-H., and Kim, M.-S. (2012). Hydrogenases for biological hydrogen production. Bioresour. Technol. 102, 8423–8431.

Kissinger, P. T., and Heineman, W. R. (1983). Cyclic Voltammetry. J. Chem. Educ. 60, 702-706.

Krasna, A. I. (1979). Hydrogenase: Properties and applications. Enzyme Microb. Technol. 1, 165–172.

Krishnan, S., and Armstrong, F. A. (2012). Order-of-magnitude enhancement of an enzymatic hydrogen-air fuel cell based on pyrenyl carbon nanostructures. Chem. Sci. 3, 1015 −1023.

Kurkin, S., George, S. J., Thorneley, R. N. F., and Albracht, S. P. J. (2004). Hydrogen-Induced Activation of the [NiFe] hydrogenase from *Allochromatium vinosum* as Studied by Stopped-Flow Infrared Spectroscopy**.** Biochemistry 43, 6820-6831.

Lamle, S. E., Vincent, K. A., Halliwell, L. M., Albracht, S. P. J., and Armstrong, F. A. (2003). Hydrogenase on an electrode: a remarkable heterogeneous catalyst. Dalton Trans. 4152-4157.

Lamle, S. E., Albracht, S. P. J., and Armstrong, F. A. (2004). Electrochemical Potential-Step Investigations of the Aerobic Interconversions of [NiFe]-Hydrogenase from Allochromatium vinosum: Insights into the Puzzling Difference between Unready and Ready Oxidized Inactive States. J. Am. Chem. Soc. 126, 14899-14909.

Lamle, S. E., Albracht, S. P. J., and Armstrong, F. A. (2005). The Mechanism of Activation of a [NiFe]-Hydrogenase by Electrons, Hydrogen, and Carbon Monoxide. J. Am. Chem. Soc. 127, 6595-6604.

Lauterbach, L., and Lenz, O. (2013). Catalytic Production of Hydrogen Peroxide and Water by Oxygen-Tolerant [NiFe]-Hydrogenase during H_2 Cycling in the Presence of O_2. J. Am. Chem. Soc. 135, 17897-17905.

Le Goff, A., Artero, V., Jousselme, B., Tran, P. D., Guillet, N., Métayé, R., Fihri, A., Palacin, S., and Fontecave, M. (2009). From Hydrogenases to Noble Metal–Free Catalytic Nanomaterials for H_2 Production and Uptake. Science 326, 1384-1387.

Leger, C., Jones, A. K., Roseboom, W., Albracht, S. P. J., and Armstrong, F. A. (2002a). Enzyme Electrokinetics: Hydrogen Evolution and Oxidation by Allochromatium Vinosum [NiFe] hydrogenase. Biochemistry 41, 15736-15746.

Leger, C., Jones, A. C., Albracht, S. P. J., and Armstrong, F.A., (2002b). Effect of a Dispersion of Interfacial Electron Transfer Rates on Steady State Catalytic Electron Transport in [NiFe] hydrogenase and Other Enzymes. J. Phys. Chem. B 106, 13058-13063.

Leger, C., Elliott, S. J., Hoke, K. R., Jeuken, L. J. C., Jones, A. K., and Armstrong, F. A. (2003). Enzyme Electrokinetics: Using Protein Film Voltammetry to Investigate Redox Enzymes and their Mechanisms. Biochemistry 42, 8653-8662.

Leger, C., Dementin, S., Bertrand., P., Rousset, M., and Bertrand., P. (2004). Inhibition and Aerobic Inactivation Kinetics of Desulfovibrio fructosovorans NiFe Hydrogenase Studied by Protein Film Voltammetry. J. Am. Chem. Soc. 126, 12162-12172.

Leger, C., Lederer, C., Guigliarelli, B., and Bertrand., P. (2005). Electron Flow in Multicenter Enzymes: Theory, Applications, and Consequences on the Natural Design of Redox Chains. J. Am. Chem. Soc. 128, 180-187.

Lemon, B. J. and Peters, J. W. (1999). Binding of Exogenously Added Carbon Monoxide at the Active Site of the Iron-Only Hydrogenase (CpI) from *Clostridium pasteurianum*. Biochemistry 38**,** 12969-12973.

Lenaz, G., and Fato, R. (1986). Is Ubiquinone Diffusion Rate-Limiting for Electron Transfer? J. Bioenerg. Biomembr. 18, 369-401.

Lenz, O., Ludwig, M., Schubert, T., Bürstel, I., Ganskow, S., Goris, T., Schwarze, A., and Friedrich, B. (2010). H_2 Conversion in the Presence of O_2 as Performed by the Membrane-Bound [NiFe] hydrogenase of Ralstonia eutropha. ChemPhysChem 11, 1107 – 1119.

Liebgott, P.-P., De Lacey, A. L., Burlat, B., Cournac, L., Richaud, P., Brugna, M., Fernandez, V. M., Guigliarelli, B., Rousset, M., Leger, C., and Dementin, S. (2010a). Original Design of an Oxygen-Tolerant [NiFe] Hydrogenase: Major Effect of a Valine-to-Cysteine Mutation near the Active Site. J. Am. Chem. Soc. 133, 986-997.

Liebgott, P.-P., Leroux, F., Burlat, B., Dementin, S., Baffert, C., Lautier, T., Fourmond, V., Ceccaldi, P., Cavazza, C., Meynial-Salles, I., Soucaille, P., Fontecilla-Camps, J. C., Guigliarelli, B., Bertrand, P., Rousset, M., Léger, C. (2010b). Relating diffusion along the substrate tunnel and oxygen sensitivity in hydrogenase. Nat. Chem. Biol. 2010, 6, 63-70.

Lin, C.-Y., Lay, C.-H., Sen, B., Chu, C.-Y., Kumar, G., Chen, C.-C., and Chang, J.-S. (2012). Fermentative hydrogen production from wastewaters: A review and prognosis. Int. J. Hydrogen Energy 37, 15632–15642.

Ludwig, M., Cracknell, J. A., Vincent, K. A., Armstrong, F. A., and Lenz, O. (2009). Oxygen-tolerant H_2 Oxidation by Membrane-bound [NiFe] Hydrogenases of Ralstonia Species. J. Biol. Chem. 284, 465–477.

Lukey, M. J., Parkin, A., Roessler, M. M., Murphy, B., Harmer, J., Palmer, T., Sargent, F., and Armstrong, F. A. (2010). How Escherichia Coli is Equipped to Oxidize Hydrogen under Different Redox Conditions. J. Biol. Chem. 285, 3928-3938.

Lukey, M. J., Roessler, M. M., Parkin, A., Evans, R. M., Davies, R. A., Lenz, O., Friedrich, B., Sargent, F., and Armstrong, F. A. (2011). Oxygen-Tolerant [NiFe] hydrogenases: The Individual and Collective Importance of Supernumerary Cysteines at the Proximal Fe-S Cluster. J. Am. Chem. Soc. 133, 16881–16892.

Luo, X., Brugna, M., Tron-Infossi, P., Giudici-Orticoni, M.-T., and Lojou, E. J. (2009). Immobilization of the hyperthermophilic hydrogenase from *Aquifex aeolicus* bacterium onto gold and carbon nanotube electrodes for efficient H_2 oxidation. Biol. Inorg. Chem. 14, 1275–1288.

Mabbott, G. A. (1983). An Introduction to Cyclic Voltammetry. J. Chem. Educ. 60, 697-702.

Macdonald, J. R. (1984). Note on the Parametrization of the Constant-Phase Admittance Element. Solid State Ionics 13, 147-149.

Macdonald, J. R. (1992). Impedance Spectroscopy. Ann. Biomed. Eng. 20, 289-305.

Madden, C., Vaughn, M. D., Díez-Pérez, I., Brown, K. A., King, P. W., Gust, D., Moore, A. L., and Moore, T. A. (2012). Catalytic Turnover of [FeFe]-Hydrogenase Based on Single-Molecule Imaging. J. Am. Chem. Soc. 134, 1577–1582.

Marchal, D., Pantigny, J., Laval, J. M., Moiroux, J., and Bourdillon, C. (2001). Rate Constants in Two Dimensions of Electron Transfer between Pyruvate Oxidase, a Membrane Enzyme, and Ubiquinone (Coenzyme Q_8), Its Water-Insoluble Electron Carrier. Biochemistry 40, 1248–1256.

Marques, M. C., Coelho, R., de Lacey, A. L., Pereira, I. A. C., Matias, P. M. (2010). The Three-Dimensional Structure of [NiFeSe] Hydrogenase from *Desulfovibrio vulgaris* Hildenborough: A Hydrogenase without a Bridging Ligand in the Active Site in Its Oxidized, “as-Isolated” State. J. Mol. Biol. 396, 893-907.

Matsumoto, T., Eguchi, S., Nakai, H., Hibino, T., Yoon, K.-S., and Ogo, S. (2014). [NiFe]Hydrogenase from Citrobacter sp. S-77 Surpasses Platinum as an Electrode for H_2 Oxidation Reaction. Angew. Chem. Int. Ed. 53, 8895 –8898.

McCafferty, E. (1997). On The Determination of Distributed Double-Layer Capacitances from Cole-Cole Plots. Corros. Sci. 39, 243-254.

Meyer, J. (2007). [FeFe] hydrogenases and their evolution: a genomic perspective. Cell.Mol.Life Sci. 64, 1063 – 1084.

Mulder, D. W., Shepard, E. M., Meuser, J. E., Joshi, N., King, P. W., Posewitz, M. C., Broderick, J. B., and Peters, J. W. (2011). Insights into [FeFe]-Hydrogenase Structure, Mechanism, and Maturation. Structure 19, 1038-1052.

Murphy, B., Sargent, F., and Armstrong, F. A. (2014). Transforming an oxygen-tolerant [NiFe] uptake hydrogenase into a proficient, reversible hydrogen producer. Energy Environ. Sci. 7, 1426-1433.

Murphy, B., Hidalgo, R., Roessler, M. M., Evans, R. M., Ash, P. A., Myers, W. K., Vincent, K. A., and Armstrong, F. A. (2015). Discovery of Dark pH-Dependent H^+ Migration in a [NiFe]-Hydrogenase and Its Mechanistic Relevance: Mobilizing the Hydrido Ligand of the Ni-C Intermediate. J. Am. Chem. Soc. 137, 8484−8489.

Naumann, R., Schmidt, E. K., Jonczyk, A., Fendler, K., Kadenbach, B., Liebermann, T., Offenhäusser, A., and Knoll, W. (1999). The peptide-tethered lipid membrane as a biomimetic system to incorporate cytochrome c oxidase in a functionally active form. Biosens. Bioelectron. 14, 651–662.

Ogata, H., Hirota, S., Nakahara, A., Komori, H., Shibata, N., Kato, T., Kano, K., and Higuchi, Y. (2005). Activation Process of [NiFe] Hydrogenase Elucidated by High-Resolution X-Ray Analyses: Conversion of the Ready to the Unready State. Structure 13, 1635–1642.

Ogata, H., Kellers, P., and Lubitz, W. (2010). The Crystal Structure of the [NiFe] Hydrogenase from the Photosynthetic Bacterium Allochromatium Vinosum: Characterization of the Oxidized Enzyme (Ni-A State). J. Mol. Biol. 402(2), 428-444.

Ogata, H., Nishikawa, and K., Lubitz, W. (2015). Hydrogens detected by subatomic resolution protein crystallography in a [NiFe] hydrogenase. Nature 250, 571-574.

Olson, J. W., and Maier, R. J. (2002). Molecular hydrogen as an energy source for Helicobacter pylori. Science 298, 1788-1790.

Orain, C., Saujet, L., Gauquelin, C., Soucaille, P., Meynial-Salles, I., Baffert, C., Fourmond, V., Bottin, H., and Léger, C. (2015). Electrochemical measurements of the kinetics of inhibition of two FeFe hydrogenases by O_2 demonstrate that the reaction is partly reversible. J. Am. Chem. Soc. 137, 12580–12587.

Oughli, A.A., Conzuelo, F., Winkler, M., Happe, T., Lubitz, W., Schuhmann, W., Rüdiger, O., and Plumeré, N. A (2015). Redox Hydrogel Protects the O_2-Sensitive [FeFe]-Hydrogenase from Chlamydomonas reinhardtii from Oxidative Damage. Angew. Chem. Int. Ed. 54, 12329-12333.

Page, C.C., Moser, C.C., Chen, X., and Dutton, P.L. (1999). Natural engineering principles of electron tunnelling in biological oxidation-reduction**.** Nature 402, 47-52.

Pandelia, M.-E., Fourmond, V., Tron-Infossi, P., Lojou, E., Bertrand, P., Leger, C., Giudici-Orticoni, M.-T., and Lubitz, W. (2010). Membrane-Bound Hydrogenase I from the Hyperthermophilic Bacterium *Aquifex aeolicus*: Enzyme Activation, Redox Intermediates and Oxygen Tolerance. J. Am. Chem. Soc. 132, 6991–7004.

Parkin, A., Cavazza, C., Fontecilla-Camps, J. C., and Armstrong, F. A. (2006). Electrochemical Investigations of the Interconversions between Catalytic and Inhibited States of the [FeFe]-Hydrogenase from Desulfovibrio desulfuricans. J. Am. Chem. Soc. 128, 16808-16815.

Parkin, A.; Goldet, G.; Cavazza, C.; Fontecilla-Camps, J. C.; Armstrong, F. A. (2008). The Difference a Se Makes? Oxygen-Tolerant Hydrogen Production by the [NiFeSe]-Hydrogenase from *Desulfomicrobium baculatum*. J. Am. Chem. Soc. 130, 13410–13416.

Parkin, A., Bowman, L., Roessler, M. M., Davies, R. A., Palmer, T., Armstrong, F. A., and Sargent, F. (2012). How Salmonella oxidises H_2 under aerobic conditions. FEBS Lett. 586, 536–544.

Parkin, A., and Sargent, F. (2012). The hows and whys of aerobic H_2 metabolism. Curr. Opin. Chem. Biol. 16, 26–34.

Pershad, H. R., Duff, J. L. C., Heering, H. A., Duin, E. C., Albracht, S. P. J., and Armstrong, F. A. (1999). Catalytic Electron Transport in *Chromatium vinosum* [NiFe]-Hydrogenase: Application of Voltammetry in Detecting Redox-Active Centers and Establishing That Hydrogen Oxidation Is Very Fast Even at Potentials Close to the Reversible H^+/H_2 Value. Biochemistry 38, 8992-8999.

Plumeré, N., Rüdiger, O., Oughli, A.A., Williams, R., Vivekananthan, J., Pöller, S., Schuhmann, W., and Lubitz, W. (2014). A redox hydrogel protects hydrogenase from high-potential deactivation and oxygen damage. Nat. Chem. 6, 822-827.

Reeve, H. A., Lauterbach, L., Ash, P. A., Lenz, O., and Vincent, K. A. (2012). A modular system for regeneration of NAD cofactors using graphite particles modified with hydrogenase and diaphorase moieties. Chem. Commun. 48, 1589–1591.

Reeve, H. A., Lauterbach, L., Lenz, O., and Vincent, K. A. (2015). Enzyme-Modified Particles for Selective Bio-Catalytic Hydrogenation via H_2-driven NADH Recycling. ChemCatChem 7, 3480-3487.

Reisner, E. (2011). Solar Hydrogen Evolution with Hydrogenases: From Natural to Hybrid Systems. Eur. J. Inorg. Chem. 7, 1005–1016.

Richter, R. P., Berat, R., and Brisson, A. R. (2006). Formation of Solid-Supported Bilayers: An Integrated View. Langmuir 22, 3497-3505.

Roessler, M. M., Evans, R. M., Davies, R. A., Harmer, J., and Armstrong, F. A. (2012). EPR Spectroscopic Studies of the Fe–S Clusters in the O_2-Tolerant [NiFe]-Hydrogenase Hyd-1 from *Escherichia coli* and Characterization of the Unique [4Fe–3S] Cluster by HYSCORE. J. Am. Chem. Soc. 134, 15581–15594.

Rüdiger, O., Abad, J. M., Hatchikian, E. C., Fernandez, V. M., and De Lacey, A. L. Oriented Immobilization of *Desulfovibrio gigas* Hydrogenase onto Carbon Electrodes by Covalent Bonds for Nonmediated Oxidation of H_2 (2005). J. Am. Chem. Soc. 127, 16008–16009.

Saggu, M., Zebger, I., Ludwig, M., Lenz, O., Friedrich, B., Hildebrandt, P., and Lendzian, F. (2009). Spectroscopic Insights into the Oxygen-tolerant Membrane-associated [NiFe] Hydrogenase of Ralstonia eutropha H16. J. Biol. Chem. 284(24), 16264-16276.

Sahaym, U., and Norton, G. (2008). Advances in the application of nanotechnology in enabling a 'hydrogen economy'. J. Mater Sci. 43, 5395–5429.

Schäfer, C., Friedrich, B., and Lenz, O. (2013). Novel, Oxygen-Insensitive Group 5 [NiFe] hydrogenase in *Ralstonia eutropha*. Appl. Environ. Microbiol. 79, 5137–5145.

Schäfer, C., Bommer, M., Hennig, S. E., Jeoung, J. H., Dobbek, H., and Lenz, O. (2016). Structure of an actinobacterial-type [NiFe]-hydrogenase reveals insight into O_2-tolerant H_2 oxidation. Structure 24, 285–292.

Schiller, S. M., Naumann, R., Lovejoy, L., Kunz, H., and Knoll, W. (2003). Archaea Analogue Thiolipids for Tethered Bilayer Lipid Membranes on Ultrasmooth Gold Surfaces. Angew. Chem. Int. Ed. 42, 208-211.

Schink, B. and Probst, I. (1980). Competitive Inhibition of the Membrane-Bound Hydrogenase of Alcaligenes Eutrophus by Molacular Oxygen. Biochem. Biophys. Res. Comm. 95,1563-1569.

Schink, B. and Schlegel, H. G. (1979). The Membrane-Bound Hydrogenase of *Alcaligenes Eutrophus* I. Solubilization, Purification, and Biochemical Properties. Biochim. Biophys. Acta 567, 315-324.

Sezer, M., Frielingsdorf, S., Millo, D., Heidary, N., Utesch, T., Mroginski, M.-A., Friedrich, B., Hildebrandt, P., Zebger, I., Weidinger, I. M. (2011). Role of the HoxZ Subunit in the Electron Transfer Pathway of the Membrane-Bound [NiFe]-Hydrogenase from *Ralstonia eutropha* Immobilized on Electrodes. J. Phys. Chem. B 115, 10368-10374.

Shomura, Y., Yoon, K.-S., Nishihara, H., and Higuchi, Y. (2011). Structural basis for a [4Fe-3S] cluster in the oxygen-tolerant membrane-bound [NiFe] hydrogenase. Nature 479, 253-257.

Silakov, A., Kamp, C., Reijerse, E., Happe, T., and Lubitz, W. (2009). Spectroelectrochemical Characterization of the Active Site of the [FeFe] Hydrogenase HydA1 from Chlamydomonas reinhardtii. Biochemistry 48, 7780–7786.

Stephenson, M., and Stickland, L. H. (1931). Hydrogenase: a bacterial enzyme activating molecular hydrogen. I. The properties of the enzyme. Biochem. J. 25, 205-214.

Stripp, S. T., Goldet, G., Brandmayr, C., Sanganas, O., Vincent, K. A., Haumann, M., Armstrong, F. A., and Happe, T. (2009) How oxygen attacks [FeFe] hydrogenases from photosynthetic organisms. Proc. Natl. Acad. Sci. USA 106, 17331-17336.

Su, L. Y., Hawkridge, F. M., and Rhoten, M. C. (2004). Electroreduction of Oxygen by Cytochrome c Oxidase Immobilized in Electrode-Supported Lipid Bilayer Membranes. Chem. Biodiversity 1, 1281–1288.

Swanson, K.D., Ratzloff, M.W., Mulder, D.W., Artz, J.H., Ghose, S., Hoffman, A., White, S., Zadvornyy, O.A., Broderick, J.B., Bothner, B., King, P.W., and Peters, J.W. (2015). [FeFe]-hydrogenase oxygen inactivation is initiated at the H cluster 2Fe subcluster. J. Am. Chem. Soc. 137, 1809-1816.

Thauer, R.K., Kaster, A.-K., Goenrich, M., Schick, M., Hiromoto, T., and Shima, S. (2010). Hydrogenases from Methanogenic Archaea, Nickel, a Novel Cofactor, and H_2 Storage. Annu. Rev. Biochem. 79, 507–36.

Thauer, R.K. (2011). Hydrogenases and the Global H_2 Cycle. Eur. J. Inorg. Chem. 7, 919–921.

Vignais, P. M., and Billoud, B. (2007). Occurrence, Classification, and Biological Function of Hydrogenases: An Overview. Chem. Rev. 107, 4206−4272.

Vincent, K. A., Parkin, A., Lenz, O., Albracht, S. P. J., Fontecilla-Camps, J. C., Cammack, R., Friedrich, B. and Armstrong, F. A. (2005a). Electrochemical Definitions of O_2 Sensitivity and Oxidative Inactivation in Hydrogenases. J. Am. Chem. Soc. 127, 18179-18189.

Vincent, K. A., Cracknell, J. A., Lenz, O., Zebger, I., Friedrich, B., and Armstrong, F. A. (2005b). Electrocatalytic hydrogen oxidation by an enzyme at high carbon monoxide or oxygen levels. Proc. Natl. Acad. Sci. USA 102, 16951–16954.

Vincent, K. A., Cracknell, J. A., Clark, J. R., Ludwig, M., Lenz, O., Friedrich, B., and Armstrong, F. A. (2006). Electricity from low-level H_2 in still air – an ultimate test for an oxygen tolerant hydrogenase. Chem. Commun. 5033-5035.

Vincent, K. A., Parkin, A., and Armstrong, F. A. (2007). Investigating and Exploiting the Electrocatalytic Properties of Hydrogenases. Chem. Rev. 107, 4366-4413.

Volbeda, A., Charon, M. H., Piras, C., Hatchikian, E. C., Frey, M., and Fontecilla-Camps, J. C. (1995). Crystal structure of the nickel-iron hydrogenase from *Desulfovibrio gigas*. Nature 373, 580-587.

Volbeda, A., Martin, L., Cavazza, C., Matho, M., Faber, B. W., Roseboom, W., Albracht, S. P. J., Garcin, E., Rousset, M., and Fontecilla-Camps, J. C. J. (2005). Structural differences between the ready and unready oxidized states of [NiFe] hydrogenases Biol. Inorg. Chem. 10, 239-249.

Volbeda, A., Amara, P., Darnault, C., Mouesca, J.-M., Parkin, A., Roessler, M. M., Armstrong, F. A., and Fontecilla-Camps, J. C. (2012). X-Ray Crystallographic and Computational Studies of the O_2-Tolerant [NiFe] hydrogenase 1 from *Escherichia Coli*. Proc. Natl. Acad. Sci. USA 109, 5305-5310.

Volbeda, A., Darnault, C., Parkin, A., Sargent, F., Armstrong, F. A., and Fontecilla-Camps, J. C. (2013**)** Crystal Structure of the O_2-Tolerant Membrane-Bound Hydrogenase 1 from Escherichia Coli in Complex with its Cognate Cytochrome *b*. Structure 21, 184-190.

Wait, A. F., Parkin, A., Morley, G. M., dos Santos, L., and Armstrong, F. A. (2010). Characteristics of Enzyme-Based Hydrogen Fuel Cells Using an Oxygen-Tolerant Hydrogenase as the Anodic Catalyst. J. Phys. Chem. C 114, 12003–12009.

Wakerley, D. W., and Reisner, E. (2015). Oxygen-tolerant proton reduction catalysis: much O_2 about nothing? Energy Environ. Sci. 8, 2283-2295.

Wallace, B. J., and Young, I. G. (1977). Role of quinones in electron transport to oxygen and nitrate in *Escherichia coli*. Studies with a *ubiA*$^-$ *menA*$^-$ double quinone mutant. Biochim. Biophys. Acta 461, 84-100.

Wang, J. (2000). Analytical Electrochemistry, 2nd Ed., Wiley-VCH, New York.

Weiss, R. F. (1970). The solubility of nitrogen, oxygen and argon in water and seawater. Deep-Sea Res. Oceanogr. Abstr. 17, 721-735.

Weiss, S. A., Bushby, R. J., Evans, S. D., Henderson, P. J. F., and Jeuken, L. J. C. (2009). Characterisation of cytochrome *bo3* activity in a native-like surface-tethered membrane. Biochem. J. 417, 555-560.

Weiss, S. A., Bushby, R. J., Evans, S. D., and Jeuken, L. J. C. (2010). A study of cytochrome bo_3 in a tethered bilayer lipid membrane. Biochim. Biophys. Acta 1797, 1917–1923.

Whipple, G. C., Whipple, M. C. (1911). Solubility of Oxygen in Sea Water. J. Am. Chem. Soc. 33(3), 362-365.

Woolerton, T. W., and Vincent, K. A. (2009). Oxidation of dilute H_2 and H_2/O_2 mixtures by hydrogenases and Pt. Electrochim. Acta 54, 5011–5017.

Wulff, P., Day, C. C., Sargent, F., and Armstrong, F. A. (2014). How oxygen reacts with oxygen-tolerant respiratory [NiFe]-hydrogenases. Proc. Natl. Acad. Sci. USA 111, 6606–6611.

Wulff, P., Thomas, C., Sargent, F., and Armstrong, F. A. (2016). How the oxygen tolerance of a [NiFe]‑hydrogenase depends on quaternary structure. J. Biol. Inorg. Chem. 21, 121-134.

Xu, L., and Armstrong, F. A. (2013). Optimizing the power of enzyme-based membrane-less hydrogen fuel cells for hydrogen-rich H_2–air mixtures. Energy Environ. Sci. 6, 2166-2171.

Zirngibl, C., van Dongen, W., Schwoerer, B., von Buenau, R., Richter, M., Klein, A., and Thauer, R. K. (1992). H_2-forming methylenetetrahydromethanopterin dehydrogenase, a novel type of hydrogenase without iron-sulfur clusters in methanogenic archaea. Eur. J. Biochem. 208, 511–520.

Zoski, C. G. (2001). Handbook of Electrochemistry, 1st Ed., Elsevier, Amsterdam.